Nº D'ORDRE: 41095

THÈSE EN CO-TUTELLE PRESENTÉE DEVANT L'UNIVERSITÉ DE FLORIDE

POUR OBTENIR LE GRADE DE

PH.D. CHEMICAL ENGINEERING DE

L'UNIVERSITÉ DE FLORIDE ET DE

DOCTORAT EN MÉCANIQUE POUR L'INGENIEUR DE

L'UNIVERSITÉ DE LILLE 1 SCIENCES ET TECHNOLOGIES

SOUTENUE PUBLIQUEMENT LE 25 MARS 2013 PAR

WILLIAM R. BATSON III

FARADAY WAVES IN SMALL CYLINDERS AND THE SIDEWALL NON-IDEALITY

(INSTABILITÉ DE FARADAY CONFINÉE DANS UNE CELLULE CYLINDRIQUE ET LA PROBLÉMATIQUE DE CONDITIONS LIMITES)

MEMBRES DU JURY:

JASON WEAVER	UNIVERSITÉ DE FLORIDE	**PRÉSIDENTE DU JURY**
MAURICE ROSSI	UNIVERSITÉ PIERRE ET MARIE CURIE	**RAPPORTEUR**
DMITRY KOPELEVICH	UNIVERSITÉ DE FLORIDE	**RAPPORTEUR**
RANGA NARAYANAN	UNIVERSITÉ DE FLORIDE	**CO-DIRECTEUR DE THÉSE**
FARZAM ZOUESHTIAGH	UNIVERSITÉ LILLE 1	**CO-DIRECTEUR DE THÉSE**
SERGEI PILYUGIN	UNIVERSITÉ DE FLORIDE	**INVITE**
UWE EHRENSTEIN	AIX-MARSEILLE UNIVERSITÉ	**INVITE**
PIERRE COLINET	UNIVERSITÉ LIBRE DE BRUXELLES	**INVITE**

To my family and friends

ACKNOWLEDGMENTS

This manifestation marks an accomplishment for which I am most proud of, as I believe I have given as much of myself to it as I possibly could, justified by the immense amount of satisfaction it has given me.

I would like to thank my parents Billy and Susan for giving me their unconditional love and support through all these years. They have set the example which I will forever try to follow. I am equally grateful to be able to share so much with my brother Thomas and sister Grayce.

Beyond family, I first and foremost would like to thank all who teach. I am here because of an outstanding line of teachers, and the opportunities they have provided me. Learning is my most prized hobby and these are the facilitators.

Ranga Narayanan, after my family, will stand as one of the most influential people in my life. The pursuit of science is my dream, and regardless of what happens in the future, I can already say that I have done that, because of him. He is a dear friend who I have an utmost respect for, given his true love for what he does, which I hope he continues to do for a long time.

A warm reflection of Ranga's personality, my French advisor, Farzam Zoueshtiagh, is devoted to his work and his family, and stands as role model for a person I strive to become. Alongside him in Lille I was able to work with an incredible level of focus and accomplish nearly every goal I set, because he repeatedly extended himself to ensure my comfort and unlock resources.

I am also very appreciative of the staffpersons of both IEMN in Lille and the University of Florida Department of Chemical Engineering. Hélène Delsarte, the busiest person at IEMN, was especially helpful in my dealings with administration (and tolerable of my French!). Carolyn Miller, who navigated my travel paperwork at UF, was always concerned for my best interest.

The satisfaction I derive from work is intimately connected with my friendships, and oftentimes it seems like one would not exist without the other. Therefore I must say the spreading of myself through Gainesville was a special path laden with great memories. Joseph C. Revelli III and Christopher P. Muzzillo are two caring guys whose opinions and thoughts I will forever value.

I thank the Partner University Fund and the Embassy of France for a Chateaubriand Fellowship during Spring 2011 and the University of Florida for the part-alumni fellowship for a major part of my Doctoral work. The National Science Foundation provided funding via grant NSF OISE 0968313. I am grateful to all of them in no small measure.

TABLE OF CONTENTS

LIST OF TABLES

LIST OF FIGURES

Abstract of Dissertation Presented to the Graduate School
of the University of Florida in Partial Fulfillment of the
Requirements for the Degree of Doctor of Philosophy

FARADAY WAVES IN SMALL CYLINDERS AND THE SIDEWALL NON-IDEALITY

By

William R. Batson III

May 2013

Chair: Ranganathan Narayanan
Major: Chemical Engineering

This work is the result of a scientific inquiry into the current understanding of experimental single-mode Faraday waves, from the perspective of the linear stability theory. Given an electromechanical shaker capable of imposing vibrations of several centimeters at frequencies of up to 15 Hz, experiments were directed toward laterally “small” systems in which the cell modes are discretized and the excited wavelength was of the order of the lateral dimension. In this regime, the theoretically tractable boundary condition for the sidewalls is a stress free condition, which is a challenge to produce experimentally. In reality, the no-slip behavior of the fluid along the sidewalls and interfacial contact line effects such as capillary hysteresis introduce sidewall stresses. In the interest of comparing an experiment to the theory, it was therefore necessary to develop an experiment which respected this assumption. This marks the first attempt to match the single mode Faraday experiment to a linear theory that rigorously treats viscosity. Past experiments comparing the observed threshold to a theory have found agreement by phenomenologically accounting for the overall system damping. While remarkable that such a match can be made, the observed thresholds of past experiments in general do not agree with the predictions of the viscous linear stability theory, thereby motivating this work.

Instrumental to the production of a system that respects the stress-free condition is the choice of system liquids. In these experiments it was found that the liquids FC70

and silicone oil, which, other than a slight meniscus, produced a flat interface that moved with little effort once the container was tilted. This behavior stands in contrast to that of a water-air or an immiscible silicone oil-water interface in a glass beaker, which suffer from pinning to the sidewall. Closer inspection of the FC70-oil interface at the sidewalls shows formation of a tiny oil film in a tilted cell where bulk FC70 had displaced bulk silicone oil. It is believed this film is instrumental in reducing the stresses associated with the sidewall, and its dynamics alone are a remarkable result worthy of continued study. Wave decay experiments confirm the dominance of the bulk viscous contribution to the sidewall damping effects when measuring the overall system damping, supporting the case that the stress-free condition has been approximated.

In proceeding to interpret the experiments, first the viscous linear stability theory of Kumar & Tuckerman[52] is presented, and modified with the stress free boundary condition to account for mode discretization. The linear theory is capable of predicting the threshold amplitude, above which the flat interface is unstable and deflection occurs. In horizontally infinite systems the well-known result is that the instability is subharmonically excited–with a frequency half that of the forcing frequency. The main implication of mode discretization is the system no longer necessarily has access to a mode whose frequency is half the imposed frequency. Instead the continuum of available modes is discretized, and each available mode can be excited inside of its own frequency band. The corresponding threshold amplitudes for each band descend to a minimum amplitude near the natural frequency of the mode, and the points at which the thresholds of neighboring modes intersect are co-dimension 2 points, conditions where two modes are neutrally stable. Another important implication of a finite system is the ability to access instability tongues with harmonic and superharmonic responses.

The theoretical concepts of the critical threshold and frequency bands at which modes appear are studied extensively with the FC70 and silicone oil system. In a system oscillating below the instability threshold, tiny flow perturbations are seen due

to the emission of waves from the oscillating meniscus, an unavoidable non-ideality. Imposing vibrations above the threshold amplitude results in the gradual (or sudden) deflection and growth of the interface to some new state. Experimental thresholds are therefore marked by performing a series of trials at different amplitudes, and the lowest amplitude at which the instability is observed is marked as the threshold. Data sets are built by measuring the threshold for the experimental frequency band, and bounded with the co-dimension 2 points. Agreement between these data sets is seen to improve when lower viscosity silicone oils are used, presumably due to the decrease in the sidewall film thickness and shearing stresses.

Two complete data sets of several subharmonic, harmonic, and superharmonic modes are presented for FC70 and 1.5 cSt silicone oil systems of different layer heights, and are compared to the predictions of the linear theory. While slightly higher than predicted thresholds are observed near the mode natural frequencies, the agreement is quite good as one moves toward the co-dimension 2 points. The deviation near the natural frequencies appears to be greater for modes with greater number of azimuthal nodes, suggesting an associated increase in wall damping. Considerable deviation is seen in the lower-than-predicted thresholds for the harmonic modes, most noticeably for the mode showing the same azimuthal uniformity as the sidewall meniscus, suggesting an interaction between the harmonic modes with the meniscus waves, which are also harmonic with the cell motion. Similar deviation is seen for the other harmonic modes, albeit less due to the spatial mismatch of the instability with the meniscus wave. This is another key finding of this work, as it could potentially be modeled as an inhomogeneous interaction with the instability.

The power of the linear theory comes in being able to predict the mode of instability and the critical threshold at which it appears, whereas growth beyond the infinitesimal state a nonlinear theory is required. A nonlinear theory was not completed in this work and therefore the experiment was used primarily for comparison to the linear theory.

Qualitative nonlinear observations, however, were numerous, and many are presented in the interest of both giving a broader sense of the experiment and insight into the parameter spaces a weakly nonlinear theory might show agreement. In general it is observed that excitation of the instability at an amplitude close to the threshold often results in a mode that grows and saturates to a finite amplitude that closely resembles the linear spatial form of the mode. Continued increase of the imposed amplitude eventually results in the appearance of secondary instabilities which can either be a source of nonlinear damping or a pathway to mode breakup. Additionally, behavior suggests a subcritical bifurcation for frequencies below the natural frequency and supercritical above, consistent with past experiments.

The final result presented is for when the instability is excited with two frequencies, a novelty for single mode experiments. The theory can be written and predictions made for the case when these two frequencies are integer multiples of a basic frequency and a basic amplitude, and the results of this method are presented and discussed. An important implication of the addition of a second frequency component is the addition of three degrees of freedom: the amplitude, frequency, and phase shift of the second component. A larger parameter space is therefore necessary to conduct a thorough investigation. While initial experiments on double frequency excitation of single modes is shown to agree with the theory for a few selected modes, the threshold behavior of the harmonic mode that was observed to interact with the meniscus waves in the single frequency case is seen to produce even more irregular behavior when the second frequency component is added.

CHAPTER 1
INTRODUCTION

This work concerns an investigation into the wave phenomenon originally reported by Faraday [30] in 1831, appearing at the surface of a liquid layer that was made to vibrate up and down in an oscillatory fashion. Henceforth bearing his name, Faraday waves are most simply characterized by the deflection, growth and saturation of the normally flat fluid interface to a standing wave when the amplitude of vibration surpasses a critical threshold. Faraday also observed the wave frequency to be one half that of the imposed vibrations, i.e. subharmonic resonance, which is now understood to be characteristic of parametric excitation. Subharmonic resonance was also observed in the experiment of Melde [57], who induced such behavior in a string by periodically adjusting its tension at a frequency equal to twice the frequency of the string's dominant mode. Motivated by the experiments of Melde and Faraday, and following analysis of the lunar perigee by Hill [39], Rayleigh [68] put forth a mathematical argument for the existence of subharmonic solutions appearing above a critical parametric threshold in single degree of freedom mechanical systems.

Classical examples of such systems, including simple pendulums or a mass attached to a spring, exhibit nonlinearities due to the dependence of the system force on the state of the system. In the investigation of his own experiments like that of Melde, Raman [67] extended Rayleigh's analysis by inclusion of cubic nonlinearity in the spring tension with respect to its displacement. Nonlinear behavior in Faraday's waves is also present, as wave restorative forces such as buoyancy and surface tension and dissipative forces such as viscosity depend upon the amplification of the wave and the fluid velocities. Therefore common analyses of such systems tend to first focus on the linearized behavior of the system, in the case of Rayleigh's analysis the parametric threshold represents the departure of the system from a quiescent state. In the case of Faraday's waves, Benjamin & Ursell [11] in 1954 successfully described the departure

from the flat state by reducing the inviscid fluid equations of motion to the Mathieu equation, viz.,

$$\partial_{tt}\zeta_m + [p_m + 2q_m \cos T]\,\zeta_m = 0$$

The classical form of the Mathieu equation, shown above, depicts the parametric excitation of a linear harmonic oscillator. The scaling uncovered by Benjamin & Ursell shows that the square of the natural wave frequency of a Faraday system, determined by the fluid density, surface tension, and wavelength, to be represented by the parameter p_m, the parametric amplitude by q_m and the wave response amplitude by the dependent variable ζ_m. What can be shown either by numerical integration or advanced analysis, in accordance with observations of Faraday and Rayleigh, is that for certain values of p_m and q_m the response ζ_m grows without bound with half-integer ($\frac{\omega}{2}$, ω and $\frac{3\omega}{2}$) frequencies with respect to the parametric frequency. Sufficient reduction of the amplitude q_m results in a bounded solution for long time indicating system stability, and the existence of a neutrally stable q_m. Fundamental physics of the Faraday phenomenon are gleaned from this model as the definitions of p_m and q_m provide excellent approximation for the excited wavenumber.

However, the Mathieu equation is insufficient for predicting the threshold amplitudes in an experiment such as that of Faraday. The reason is two-fold, and highlights the fundamental differences between high-frequency experiments, and low-frequency experiments such as those Benjamin & Ursell performed and compared their model to. First, dissipation, an effect present in all real systems, is absent in this model, and it will be shown that the effect of fluid viscosity can not simply be incorporated by insertion of linear damping into the Mathieu equation. The second reason is analogous to the quantum mechanical particle in a box, and the boundary conditions it must satisfy, which places restrictions on the allowed wavefunctions and energies. At low energy levels the spacing between allowed wavefunction energies is finite, forming a discrete set,

while at sufficiently high energy these levels form a continuous set. The same is true of the Faraday wave system, where there exists a regime, accessed by sufficiently high parametric frequencies, where the spacing between the allowed wavenumbers is very small and the set forms a continuum. The regime of interest to this dissertation, is low frequency excitation, where the wavenumbers allowed by the system form a discretized set, and are strongly dependent upon the boundary conditions and the lateral geometry of the container.

Due to the absence of dissipation in the Mathieu equation, perfect resonance is attained for infinitesimal forcing amplitudes whenever the imposed frequency is a half-integer multiple of a wave's natural frequency. Therefore a high-frequency system having access to a continuum of modes would invariably be unstable because one of these modes is bound to be in perfect resonance with the parametric frequency. Development of the viscous linear stability model by Kumar & Tuckerman [52] has allowed for the prediction of the experimental threshold in a high-frequency system. On the other hand, the Mathieu equation has been shown to be sufficient in the low-frequency discretized system, as experiments with low-viscosity fluids can relegate the sources of dissipation to the sidewalls, which experimentally have been shown to be linear. Discretized experiments therefore have neglected analysis from the perspective of a fluid mechanical system, but rather as a parametrically excited single degree of freedom system with linear damping. While a valid approach, what will be discussed is that the prediction of this dissipation is extremely difficult, requiring its measurement directly from the experiment. In some ways this phenomenological nature is unsatisfying, and what will be shown in this work is that an experimental effort can be made to approximate the appropriate boundary conditions, allowing closer connection to the Kumar & Tuckerman model. In doing so not only has it become possible to accurately predict selected modes and threshold amplitudes, but also to pinpoint the causes for difference which lend themselves to a myriad of rich phenomena.

It was investigation of the pattern forming behavior, originally observed by the high-frequency experiments of Faraday, that was seen as a pathway to disorder and chaos and led to the development of the viscous linear stability analysis of Kumar & Tuckerman. Other hydrodynamic instabilities such as Rayleigh-Bènard convection and Taylor-Couette flow had exhibited transitions from regular patterns to chaos and turbulence, and such transitions were similarly displayed in the Faraday wave experiments of Keolian *et al.* [47], Gollub & Meyer [33] and Ezerskii *et al.* [29] as the parametric amplitude was increased well past the critical point. Faraday wave patterns symmetric and asymmetric with the container geometry were studied for the instability nearer the threshold by Douady & Fauve [26]. Of note is that they filled their square container to the brim, thereby pinning the interface with a 90° contact angle and eliminating the parasitic waves emitted by a meniscus subjected to vibrations. Douady [25] studied the effect of the meniscus on mode discretization at moderate frequencies by measuring the linear threshold for several modes in a brimful system and one with a prominent meniscus. However, these thresholds were not compared to a theory, and Douady acknowledged that the cell modes in a brimful system do not respect the proper boundary conditions and that a model did not exist that correctly treated viscosity. The importance of viscosity to the linear threshold in a high-frequency system was further highlighted by the high-frequency experiments of Fauve *et al.* [31], who observed systematically higher thresholds than those predicted by a model including linear viscous dissipation.

Following classical hydrodynamic stability analysis like that of Chandrasekhar [16], Kumar & Tuckerman [52] studied the stability of a horizontally infinite bilayer subjected to parametric forcing, while respecting the role of viscosity present in the Navier-Stokes equations. They did this by means of a Fourier-Floquet analysis which cast the linear stability of a spatial wavenumber k into an infinite set equations for the perturbed interfacial deflection, coupled by virtue of the parametric forcing term cos ωt. Setting

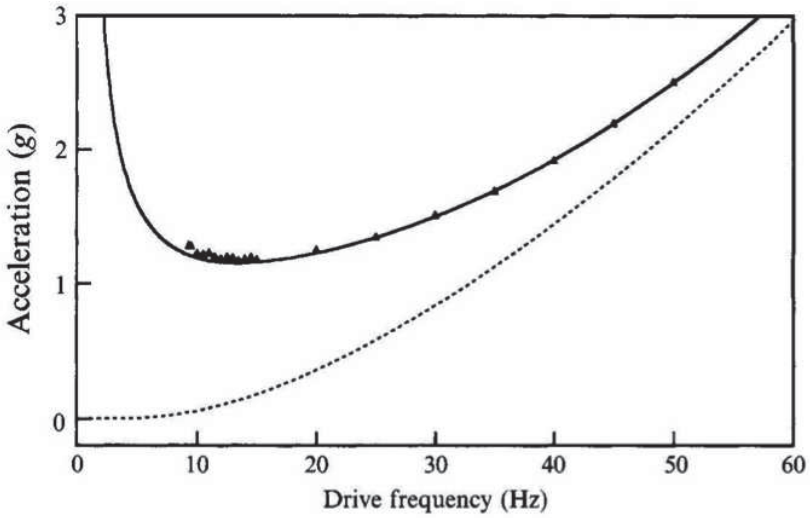

FIGURE 7. Threshold measurements for oil at 55 °C in a square container of width 11.4 cm and depth 0.24 cm. The solid line is the finite-depth numerical calculation; the dashed line is the infinite-depth one.

Figure 1-1. Measurement of the instability threshold by Bechhoefer *et al.* [8].

the growth rate of the Floquet exponent to zero, the neutrally-stable amplitudes A were numerically calculated as the eigenvalues of the truncated system. Repeated solution of this problem for all values of *k* produced a diagram of the neutral amplitudes A outlining several regions for which a solution would grow in time, similar to the diagram depicting the stability of solutions to the Mathieu equation. Different, however was the damping of the threshold tongues to a finite amplitude, indicating the presence of viscous effects. The global minimum of this diagram thereby established the threshold amplitude at which the interface belonging to a horizontally infinite system would destabilize.

This calculation represents the main theoretical tool used in this work and will be presented in detail in Chapter 2. The predicted amplitudes and wavenumbers were successfully reproduced in an experiment by Bechhoefer *et al.* [8], whose results are presented in Figure 1-1. The focused regime of this dissertation are the oscillations in the thresholds occurring at low frequencies, which they acknowledge is due to the discretization of cell modes. Data points corresponding to these thresholds were characterized by distinct patterns, whereas at higher frequencies they observed well

ordered squares. These distinct patterns, or cell modes as they will be referred to throughout this work, are dependent not only upon the container geometry but also upon the sidewall contact behavior of the fluid interface. Mathematically, the tractable condition which allows the separation of the horizontal spatial dependence of each cell mode is the so-called stress-free condition, and was used by Benjamin & Ursell to adapt the Mathieu equation predictions to their single-mode experiment.

This history and discussion forms the motivation for this work, because, to date, adaptation of the Kumar & Tuckerman model with the stress-free condition has not been made, nor has a discretized Faraday wave system been designed which replicates this condition, allowing for the a priori prediction of the instability threshold. The work that will be presented represents the course of study taken to put forth such an effort, and is not only composed of the design and results of the experiment, but also an amount of theoretical detail sufficient to reproduce the linear stability predictions to which the experiment was compared. An additional experimental case considered was that where the parametric forcing was composed of two frequencies, a theoretical extension treated by Besson *et al.* [12], which is also presented along with adaptation of the stress-free condition in Chapter 2. An especially insightful part of this work, providing further historical context, is the retrospective comparison in Chapter 3 of the viscous linear theory to the previous experiments that measured single mode thresholds, highlighting that previous experiments have been controlled by sidewall or interfacial effects. Experimental design, repeatability, and measurement analysis are detailed in Chapter 4 and highlights the considerations taken towards producing an ideal system. Chapter 5 presents the general experimental behavior, the agreement and disparities with the theory, and the investigation into higher order nonlinear phenomena. The influence of the double-frequency parametric forcing on the experimental agreement with the theory is investigated in Chapter 6. Here, quantitative nonlinear data is also presented which represents the furthest extent of the experimental investigation. Finally,

discussion, conclusions, and avenues for future study are presented in Chapter 7. Before proceeding, however, a more detailed look at the previous work on parametric resonance and Faraday waves will be given.

Literature Review

In the following literature review the experimental and theoretical advancement of Faraday waves will be presented, along with a nuanced scientific application and a technological application. First, the resurgence of the phenomenon in the 1980s will be discussed in the context of experiments which probed the different transitions made from regular waves to disordered behavior and chaos. Following are the experiments which moved closer to the instability threshold, which promoted the phenomenon to the status of being the premier testbed for nonlinear pattern formation. The discovery of this rich behavior begged stronger theoretical explanation, which was made by development of linear and weakly nonlinear stability analyses, which will also be discussed at length.

Spatiotemporal Chaos

Interest in the Faraday problem began to build in the early 1980s with the experiments of Keolian *et al.* [47] who followed a pursuit for chaos and turbulence arising from hydrodynamic instabilities. They parametrically excited a water layer in a thin cylindrical annulus, therefore with limited spatial behavior, and observed that an increased parametric amplitude resulted in sequenced increases in the response frequency from the initial subharmonic response. Gollub & Meyer [33] introduced a spatial variation into this nonlinear behavior by studying the transitions made in a large cylindrical layer of water. Relative to the current work, they noted and measured a threshold which did not monotonically decrease with frequency, undoubtedly due to mode discretization. Their interest however was spatiotemporal variation, and they observed such transitions from subharmonic modes with spatial axisymmetry, followed by modes with periodic modulations to the axisymmetry, then quasiperiodic modulations with azimuthal spatial modulations, and finally to complete spatiotemporal disorder. At lower frequencies

Ciliberto & Gollub [20] reported such transitions in the interaction between two cell modes near the co-dimension 2 point, and at large frequencies, Ezerskii *et al.* [29] reported these transitions for the disordering of regular square patterns. The effects of the loss of mode degeneracy in slightly rectangular cells on the interaction between discretized modes was studied by Simonelli & Gollub [71] and even qualitatively reproduced the phase space predicted by the weakly nonlinear theory of Gu *et al.* [34]. By careful adjustment of the layer height, Henderson & Miles [37] brought subharmonic modes into internal resonance both with their subharmonic and superharmonic modes, and comprehensively mapped a phase space for the different resulting spatiotemporal behaviors, in addition to attempting theoretical comparison with that of Becker & Miles [9]. A unique method was that of Ciliberto *et al.* [19], who detect chaotic transitions in a high-frequency system by the adjustment in the required drive acceleration resulting from the changing mode dissipation.

Experimental Faraday Wave Pattern Formation

Another aspect of Faraday's waves which drew the attention of everyone in the 1990s were the patterns Faraday deemed so beautiful himself in his original experiments. Comprehensively reviewed for numerous physical systems by Cross & Hohenberg [22], including hydrodynamic systems, the pattern forming nature of the Faraday system is an attractive pattern forming system due to the short time scales and the ease of production of large aspect ratio systems. The regime in which this behavior is observed is therefore opposite of that for this dissertation: high frequencies where mode discretization is preferably absent. However, it was learned that the fluid mechanical treatment of viscosity was necessary to predict these patterns and therefore the Kumar & Tuckerman linear analysis, which is also used in this work, forms the basis for the current most complete pattern theory. Additionally, the pattern work on parametric excitation with double frequencies serves as the only work to which the

discretized results of this work can be compared to, as such experiments have not been performed in the discretized regime.

Higher-order transitions from regular patterns to more disordered states have been observed. Early experiments studying the pattern formation near the threshold excited by single parametric frequencies were conducted by Douady & Fauve [26], however these experiments were performed at moderate frequencies where effects of discretization persisted, and they interpreted their patterns in the context of individual superpositions of discrete waves, one of which was hexagonal. Tufillaro *et al.* [78] followed the experiments of Ezerskii *et al.* [29], by conducting experiments at high-frequency such that the excited wavelength was sufficiently smaller than the container size, and both observed square patterns just above the instability threshold. Christiansen *et al.* [18] further increased the system aspect ratio and generated a phase diagram of regions in which patterns formed by 3, 4 (quasicrystalline), 6 and 8 plane waves appeared. Fauve *et al.* [31] studied the instability near the liquid-vapor critical point of carbon dioxide, and observed a transition from the normal square patterns to a striped pattern as the difference in temperature from the thermodynamic critical point was decreased. Notably they also observed systematically higher thresholds for their large aspect ratio system when compared to predictions assuming linear damping. Kudrolli & Gollub [49] extensively studied the patterns formed by single-frequency forcing and established the dependence of a transition from squares to stripes on the fluid viscosity, and further report the higher order transitions from hexagons and stripes to spatiotemporal chaos.

Müller [61] was the first to report an equilateral triangular pattern, accessed by excitation with two frequencies of ratio 1:2 and explained qualitatively by amplitude equations describing the interaction of three modes. Edwards & Fauve [28] extended the two frequency work of Müller to that of an even-odd case of ratio 4:5, thereby breaking the subharmonic-harmonic time symmetry of the instability. In doing so they established dependence of the patterns on the mixing ratio and phase angle between

the two frequencies χ and ϕ. Squares, stripes, and hexagons were observed, as well as novel quasi-patterns near values of χ producing bicriticality with respect to both frequencies, and resulting from the interaction of 12 separate modes. Near the bicritical point in 4:5 and 6:7 parametric forcing and obtained by varying the phase angle ϕ, Kudrolli *et al.* [50] observed the appearance of so-called superlattice-I and superlattice-II patterns, and was explained by them as being the interaction of two separate hexagonal lattices. Such superlattices were generalized by Arbell & Fineberg [2] to that of 2-mode superlattices resulting from triad wave interactions, and additionally observed the appearance of new so-called subharmonic super lattice states away from the bicritical point. These aspects of two-frequency pattern formation in the Faraday experiment were extensively studied for 18 different frequency ratios by Arbell & Fineberg [3]. This myriad of pattern formation behavior provides insight into phenomena and interactions that could potentially be observed in future experiments double-frequency excitation in discretized experiments.

Linear Theory and Comparison to Experiments

Given the nonlinear nature of the fluid equations of motion, the theoretical study of the Faraday instability is typically approached perturbatively where analytical solutions can be derived given various assumptions. Assuming the parameter about which the equations are perturbed is very small, the basic state of the system can be described as a quiescent layered system of zero fluid velocities, a flat interface, and an oscillating vertical pressure gradient. Translation of this solution to the equation defined by the terms which are of first order in the perturbation produces a problem whose analysis constitutes linear stability theory, because the growth or decay of the solution in long time in general determines the stability of the basic state. A necessary assumption that has to be made in this analysis is the spatial extent of the system, for which a horizontally infinite system is the most simple because this allows the first order solutions to be written as being spatially periodic of wavenumber k. Theoretically the

horizontally infinite system has access to an infinite continuum of these wavenumbers, and for the conditions of instability to be determined the neutral conditions at which these wavenumbers neither decay nor grow are determined. In the case of the Faraday instability where it is observed there exists a critical threshold amplitude for any given frequency at which the interface destabilizes, the wavenumber with the lowest associated threshold would represent the first unstable mode in an experiment that was conducted at successively higher amplitudes.

This analysis was first performed by Benjamin & Ursell [11] for a horizontally infinite inviscid fluid with a passive upper layer. In doing so they highlighted that every wavenumber k possessed an unforced, natural frequency, and that the instability resulted from a resonance that occurs between this and the parametric frequency. The absence of dissipation in their model, however, meant that perfect resonance could occur for a wavenumber when excited with a frequency equal to a half-integer multiple of its own, and thus, in a horizontally infinite system which has access to an infinite number of modes, the free surface is unstable to all parametric excitations. Benjamin & Ursell themselves compared their theory to a discretized experiment which did not have access to an infinite number of modes, and this will be discussed further on as it is the regime of focus for this dissertation.

The model used in this dissertation was developed by Kumar & Tuckerman [52], as they performed the linear stability of the analysis of the nonlinear system without making the inviscid assumption. Inclusion of viscosity prevents the reduction of the linear problem to a Mathieu equation describing each wavenumber, but rather the instability of each wavenumber is defined by an infinite set of coupled equations by Fourier-Floquet analysis which must be solved numerically for the thresholds. In doing so the wavenumber corresponding to the minimum threshold is the first excited in an experiment, which was confirmed by Bechhoefer *et al.* [8] for a wide range of

frequencies (see Figure 1-1). The threshold for systems excited by two frequencies was theoretically presented and experimentally confirmed by Besson *et al.* [12].

An idea which is repeated several times throughout this work is the inherent differences between Faraday excitation at high and low frequencies. The main assumptions of the theories of Kumar & Tuckerman and Besson *et al*. which require care in experiment are that the system must produce a base state of a flat interface and no flow, and must have access to the wavenumber corresponding to the minimum predicted threshold. The normal cause for violation of the first condition is the production of a meniscus by the interface at the container sidewalls. Modulation of gravity by cell vibration causes the alteration of the desired profile meniscus, which inevitably emits a traveling wave to the interior of the interface. Continued cell vibration results in a ripple pattern on the interface which takes the geometry of the cell. This non-ideality has adverse effects both on the experimental threshold and on the nonlinear pattern formation, and therefore high-frequency experiments employ different sidewall techniques which eliminate the effect. The brimful technique of Douady & Fauve [26] is one such example which pins the interface at a 90° angle at the sidewall, thereby minimizing the parasitic waves. This was one of the methods used by Bechhoefer *et al*. and many of other experiments studying pattern formation.

Equally important to the meniscus which must be considered in experiments is that the system must have access to the wavenumber of the predicted minimum threshold. At sufficiently low frequency this however is not guaranteed, because in this regime a boundary condition must be applied to specify the discretization of the modes. Two mathematically attractive boundary conditions are that either the interface contact position remains fixed, or that the slope of the interface normal to the wall remains 90° while moving freely in the vertical. While the former pinned condition is realized by the brimful condition of Douady & Fauve, the resulting eigenfunctions for the interface are generally not compatible with the linear stability analyses of Benjamin & Ursell or

Kumar & Tuckerman. Theory for such waves, including approximation of their natural frequencies has been put forth by Benjamin & Scott [10], but its incorporation into Faraday wave theory is fleeting. The latter stress-free condition is compatible with the linear stability theories, allowing decoupling of the systems wavenumbers, and is the condition Benjamin & Ursell to adapt their theory to their discretized experiments. It should be noted however, that in finite containers such as that of Benjamin & Ursell, stresses from the sidewalls inevitably appear due to viscous Stokes boundary layers, capillary hysteresis and interfacial dissipative effects. Their system used water, a sufficiently low viscosity fluid, such that the system dissipation was in fact solely defined by these stresses, as will be shown in Chapter 3.

Knowledge of the overall system dissipation is crucial in being able to predict the threshold amplitude at which the instability appears in any regime of the instability. While careful experimental design and large aspect ratios at high frequencies has constrained these effects to the bulk fluids, enabling connection to the Kumar & Tuckerman theory, what will be shown is that for all previous experiments in the discretized regime is that the dissipative effects have been constrained to these sidewall effects. Prediction of this behavior is enormously complex, and exhibits a remarkable connection between the molecular, boundary layer and container length scales. The damping of long wavelength water waves in rectangular basins was studied by Keulegan [48], who also established that sidewall surface wetting was a key factor as identical experiments on wave decay produced far greater damping rates of the water waves in lucite containers than in glass containers. Lowering of surface tension by the addition of aerosol brought the damping rates in the two containers into agreement. Miles [58] developed a model for the damping of waves for slightly viscous fluids that separately treated the contributions due to wall boundary layers, surface films produced by contamination, and capillary hysteresis. Application of the model to the wave damping results of Keulegan and Case & Parkinson [15] yielded qualitative explanations for their observed damping rates

but not quantitative. Hocking presents a model which includes the effect of contact hysteresis by means of “wetting” boundary condition which describes a linear relation between the interface contact angle and velocity, and he uses this model to analyze the relative importance of capillary to viscous effects in the damping rates observed by Benjamin & Ursell, Case & Parkinson and Keulegan.

In applying the model of Miles [59] to the single-mode Faraday experiments of Henderson & Miles [36], it was seen that the rates were correctly predicted provided that the water viscosity was taken to be 3 cSt. Upon using this damping rate the stability model used by Henderson & Miles was able to accurately predict the Faraday instability threshold for the fundamental axisymmetric mode in their cylindrical cell. Tipton & Mullin [77] and Das & Hopfinger [23] both were able to match their experimental thresholds with curves generated using damping rates measured from the experiment. While this approach is informative, it also motivates this work to develop an experiment whose thresholds can be predicted a priori.

Nevertheless these works also studied nonlinear phenomena. The discretized regime is inherently characterized by a series of “oscillations” in the instability threshold as frequency is increased, corresponding to each allowed cell mode. Each of these oscillations descends to a minimum threshold located near the natural frequency of the mode, and the modes excited at lower frequencies and higher thresholds are referred to as “detuned” modes while those at higher frequencies and thresholds are referred to as “tuned” modes. An observation made by previous single-mode experiments such as Henderson & Miles, Tipton & Mullin and Das & Hopfinger was that the bifurcation is subcritical for detuned modes and supercritical for tuned modes, consistent with parametrically excited single degree of freedom systems. Hysteresis was also reported where the threshold at which an excited detuned mode decayed was less than the onset threshold. Mullin & Tipton probed the bifurcation structure of the fundamental axisymmetric mode and its dependence upon the liquid layer heights. Das & Hopfinger

observed regimes in which period doubling and period tripling to the main subharmonic response occurred.

Nonlinear Theoretical Advancement

In the linear stability analysis, one is able to determine the conditions at which a tiny periodic perturbation is neutrally stable, that is, it neither grows nor decays in time. Experimental precision restricts one from being able to find this point directly, instead, it is necessary to interpolate the neutral threshold lies between the conditions of one stable and another unstable state. The unstable state naturally departs from the basic state, as tiny perturbations present in the experiment grow in time. While the linear stability analysis predicts the growth constants for the departure from the basic state, the assumptions made are only valid a small distance from the critical point and the associated long time growth is exponential. Visualization of a flow or interfacial deflection in the experiment often implies that nonlinear effects have already become important. However, in regions sufficiently close to the onset of instability, it is often seen that the linear form of the perturbation has manifested itself in the nonlinear experiment, and it saturates to a finite amplitude. Such behavior is a potential candidate for a weakly nonlinear analysis in which the terms of higher order in the perturbation expansion may be considered. Upon using a correctly scaled perturbation parameter of finite amplitude, what is seen is that solvability conditions arise in the higher order problems for the solutions growing out of the first order problem. The condition manifests itself as a differential equation determining the temporal growth of the amplitude of the first order solutions, in which the time derivative of the amplitude is balanced by a linear term whose coefficient corresponds to the growth rate of linear stability. The nonlinearity then appears as terms either quadratic or cubic in the amplitude, whose coefficients govern the departure from linear growth. This equation is commonly referred to the Ginzburg-Landau equation, after those who first investigated it. Its appearance in

hydrodynamic instabilities is covered by Drazin & Reid [27], who note its resemblance to the equation for logistical population growth.

The importance of such theory to Faraday waves is based on the observation that an unstable system does not grow infinitely, and that nonlinear damping results in saturation to a finite amplitude standing wave. In the case of single-mode excitation, weakly nonlinear analysis has not been extended from the viscous Kumar & Tuckerman linear theory, and viscosity has been incorporated either by linear damping or viscous boundary layers. Such analysis resembles that of nonlinear single degree of freedom systems, covered by Nayfeh & Mook [63]. Miles [59] developed the amplitude evolution equations by a Lagrangian formulation for inviscid Faraday waves in small cylinders subject to linear damping, and is the theory to which Henderson & Miles [36] compared their amplitude responses, seeing reasonable agreement. Gu *et al.* [34] derive the amplitude equation from the interface condition for a Cartesian geometry, again including dissipation via linear damping, and the results of Virnig *et al.* [79] are compared to this theory. Hill [38] presents a unique theory for linearly damped Faraday resonance in a cartesian geometry where corrections due to sidewall and interfacial boundary layers are incorporated into the solvability conditions.

The variety of patterns observed in the regime of high single and double-frequency excitation has been a primary interest of weakly nonlinear analysis. In general these patterns are the result of excitation of the instability at a finite distance above the threshold such that a band of wavenumbers is excited simultaneously, and the nonlinear interaction of these modes gives rise to the observed pattern. Milner [60] made the first attempt to describe this behavior, and by minimization of a Lyupanov functional written for the weakly nonlinear growth of arbitrary sets of wavenumbers they find that squares were a stable pattern, in accordance with the observation of Tufillaro *et al.* [78]. This was done for the inviscid equations, and a key step was that damping was included by substitution of the expanded velocity potential into the expression for viscous dissipation.

An observation whose importance was overlooked by Milner was the divergence of the nonlinear damping coefficients when two excited wavenumbers separated by the right angle summed to a third wave with which they resonated with at second order. Termed triad resonances, their importance to pattern formation was noted by Zhang & Viñals [82] and included in their weakly nonlinear theory. They assumed viscous effects were constrained to a small layer near the interface and potential flow in the bulk, a so-called quasipotential approximation. In making this assumption and accounting for the triad interactions they predict the square pattern in the purely capillary wave regime, with the possibility of hexagonal and quasipatterns near the low limit of triad interaction in the mixed gravity-capillary regime. Chen & Viñals [17] write the weakly nonlinear theory from the fully viscous Navier-Stokes equations and produce quantitative agreement between their predictions and the pattern transitions observed in the phase space of Kudrolli & Gollub [49]. Finally Skeldon & Guidoboni [72] offer rigorous treatment of the fully viscous problem subject to double-frequency forcing and find good matching with the “regular” patterns of Kudrolli *et al.* [50] and qualitative explanation of their superlattice-I and II patterns.

Faraday Waves in Ferrofluids

Ferrofluids, invented in the 1960s, are colloidal suspensions of magnetic particles whose Brownian motion prevents settling under gravity and surfactant coating prevents agglomeration, see Rosensweig [70]. Resulting is a magnetizable fluid which has seen many commercial applications such as liquid o-rings in seals or bearing lubricants, and current interest lies in application to micro- and nano-scale devices or biological applications such as drug delivery. The subharmonic Faraday instability on a ferrofluid interface resulting from an oscillating magnetic field was observed by Perry & Jones [64] in a thin channel and the behavior was connected to that of the Hill equation. Bashtovoi & Rosensweig [7] observed the instability in a small cylindrical container and reported effects of mode discretization, in addition to a theoretical connection to the Mathieu

equation. The Rosensweig instability of a ferrofluid interface is observed when a system is subjected to a normal magnetic field of critical magnitude, as reported by Cowley & Rosensweig [21], and experiments by Pétrélis *et al.* [65] showed this instability could be stabilized by parametric oscillation of the magnetic field. An especially peculiar behavior of ferrofluids is the “negative viscosity” effect, first shown by Bacri *et al.* [4], which results from a resonance of the magnetic particle dipole with an oscillating magnetic field, thereby translating particle angular momentum to the surrounding colloidal fluid. Linear stability theories for the Faraday instability in magnetic fluids employing methods analogous to that of Kumar & Tuckerman have been presented by Bajaj & Malik [6] for single-frequency and Bajaj [5] for double-frequency excitation. A review of ferrofluids is given by Rinaldi *et al.* [69].

Faraday Waves in Microfluidics

While the pattern-forming nature of the Faraday system may be the most scientifically attractive aspect of the phenomena, there currently exists interest in Faraday waves in microfluidic design. Due to the large wave response observed in single-mode excitation, the discretized regime serves well as a means to achieve bulk fluid mixing. Excitation of the instability well above the threshold inevitably results in highly nonlinear sloshing, a field comprehensively reviewed by Ibrahim [42] with consideration of Faraday waves. Such mixing would be enhanced for immiscible systems with density stratification, as studied by Zoueshtiagh *et al.* [83]. In the interest of designing smaller and smaller systems, the instability was excited by ultrasound in geometries with width as small as 100 microns by Xu & Attinger [81]. Atomization of droplets subjected to parametric vibration was studied by James *et al.* [45], and this mechanism has been posed by Qi *et al.* [66] as a means to design portable ultrasonic nebulizers, in replacement of typical aerosol designs. Ultrahigh-frequency actuation of the instability at frequencies over 100 kHz and theoretical deviation due to microscale turbulence has recently been reported

by Blamey *et al.* [13]. The application of the Faraday instability to microfluidic systems has been reviewed by Friend & Yeo [32].

CHAPTER 2
MODEL AND LINEAR STABILITY ANALYSIS

In this chapter a linear stability model will be developed to which the experiments can be compared. Previous experiments on single-mode Faraday excitation have focused using systems with very low viscosity fluids, and have measured the system dissipation directly from the experiments. In doing so the linear and nonlinear behavior can be adequately described as a single degree of freedom system with linear damping, another example being a simple pendulum. Unique to this work is that the linear stability model for single-mode excitation in a cylindrical system will be derived directly from the Navier-Stokes equations, respecting the fluid mechanical nature of the instability and allowing an analytical description of the bulk viscous effects.

The nonlinear equations are given first, and in the interest of analyzing the departure of the system from a basic linear state, the system is then linearized. The stability of the basic state is then determined, where the conditions of neutral stability of wavenumbers k are solved for. This is done by a Fourier-Floquet method resulting in an eigenvalue problem and is solved by a cheap numerical calculation like that performed by Kumar & Tuckerman [52]. These results describe the stability of horizontally flat interface separating two immiscible fluid, and the dependence of these results on the model parameters are discussed. Next the stress-free boundary condition required by horizontally finite systems is applied to these results, which places constraints on the wavenumbers allowed by the system. Then all of these results are applied to a case study of the effect of gravity. Finally, the linear analysis is extended to systems subjected two double-frequency excitation, following that of Besson *et al.* [12], in addition to the adaptation of their model to the case of a finite cell.

Governing Equations

To analyze the stability of a flat immiscible interface subjected to an oscillatory vertical displacement with stress-free sidewalls we first take a horizontally infinite fluid

bilayer of depths h_1 and h_2 with the interface located at z = 0. We then observe that the case of stress-free sidewalls can be adapted from the horizontally infinite fluid analysis. The equations of motion governing flow of Newtonian, incompressible fluids in the bulk domains are written as,

$$\rho_j \left(\partial_t \mathbf{V}_j + \mathbf{V}_j \cdot \nabla \mathbf{V}_j\right) = -\nabla P_j + \mu_j \nabla^2 \mathbf{V}_j + \rho_j g \mathbf{k}$$

$$\text{and } \nabla \cdot \mathbf{V}_j = 0$$

where $j = 1$ indicates the lower layer and $j = 2$ the upper one. The vector $\mathbf{V}$ is the velocity field of the fluids with pressure field P, of density ρ and of viscosity μ. The vertical displacement and imposed acceleration

$$\begin{aligned} d(\tau) &= A\cos\omega\tau \\ a(\tau) &= A\omega^2\cos\omega\tau \end{aligned} \tag{2–1}$$

are accounted for in the equations of motion by adoption of a moving reference frame via the velocity transformation

$$\mathbf{V}' = \mathbf{V} + \partial_t d\,(t)\mathbf{k}$$

where the prime indicates the moving frame. Substitution into the equations of motion, and denoting the convective derivative, ∂'_t, by

$$\partial'_t = \partial_t + \partial_t d(t)\partial_z$$

the result is the grouping of the forcing acceleration $a(t)$ with the gravitational acceleration, g. Removing primes, we have,

$$\rho_j \left(\partial_t \mathbf{V}_j + \mathbf{V}_j \cdot \nabla \mathbf{V}_j\right) = -\nabla P_j + \mu_j \nabla^2 \mathbf{V}_j + \rho_j \left(g + A\omega^2\cos\omega t\right)\mathbf{k}$$

$$\text{and } \nabla \cdot \mathbf{V}_j = 0$$

No-slip conditions apply at the top and bottom walls and continuity of velocity is applied at the interface. The kinematic condition results from the jump mass balance (see Slattery [74]), i.e.,

$$[\![\rho\left(\mathbf{V}-\mathbf{U}\right)\cdot\mathbf{n}]\!] = 0 \text{ at } z = Z\left(x,y,t\right) \tag{2–2}$$

where $\mathbf{U}\cdot\mathbf{n}$ is the speed of the interface, $\mathbf{n}$ is the unit surface normal pointing into the light fluid, and $Z = Z(x,y,t)$ is the position of the interface. The surface normal $\mathbf{n} = \nabla f|\nabla f|^{-1}$, where $f = 0 = z - Z\left(x,y,t\right)$, is

$$\mathbf{n} = \frac{\mathbf{k} - Z_x\mathbf{i} - Z_y\mathbf{j}}{\left(1+Z_x^2+Z_y^2\right)^{1/2}} = \frac{\mathbf{k} - Z_x\mathbf{i} - Z_y\mathbf{j}}{|\nabla Z|} \tag{2–3}$$

In 2–2 the braces represent a jump quantity, evaluated as $[\![Q]\!] = Q_2 - Q_1$. Expanding the jump in 2–2 we have

$$\begin{aligned}
\left(\rho_2-\rho_1\right)\left(\mathbf{V}-\mathbf{U}\right)\cdot\mathbf{n} &= 0\\
\mathbf{V}\cdot\mathbf{n} &= \mathbf{U}\cdot\mathbf{n}\\
\mathbf{V}\cdot\mathbf{n} &= U\mathbf{n}\cdot\mathbf{n}\\
\mathbf{V}\cdot\mathbf{n} &= U.
\end{aligned} \tag{2–4}$$

Writing the total differential for the motion of the interface in an infinitesimal time δt we write

$$\begin{aligned}
Z\left(x,y,t+\delta t\right) - Z\left(x,y,t\right) &= \frac{\partial Z}{\partial t} + \frac{\partial Z}{\partial x}\frac{\partial x}{\partial t} + \frac{\partial Z}{\partial y}\frac{\partial y}{\partial t} + \frac{\partial Z}{\partial z}\frac{\partial z}{\partial t}\\
0 &= \frac{\partial Z}{\partial t} + \mathbf{U}\cdot\nabla Z\\
0 &= \frac{\partial Z}{\partial t} + U\mathbf{n}\cdot\mathbf{n}|\nabla Z|\\
0 &= \frac{\partial Z}{\partial t} + U|\nabla Z|
\end{aligned}$$

and making use of 2–4 followed by 2–3 we arrive at

$$\begin{aligned} \frac{\partial Z}{\partial t} &= \mathbf{V}\cdot\mathbf{n}|\nabla Z| \\ \partial_t Z &= V_z - V_x\partial_x Z - V_y\partial_y Z \text{ at } z = Z(x,y,t) \end{aligned} \tag{2–5}$$

noting that the subscripts on the velocity indicate the cartesian component while those on the surface elevation indicate partial derivatives. The stress balance at the interface,

$$[\![-P\mathbf{I} + \mu\left(\nabla\mathbf{V} + (\nabla\mathbf{V})^{\mathsf{T}}\right)]\!]\cdot\mathbf{n} = \gamma 2H\mathbf{n} \text{ at } z = Z(x,y,t)$$

states the pressure and viscous tangential stress differences between the two phases are balanced by the forces arising from surface curvature, where γ is the interfacial tension and $2H$ is twice the mean surface curvature. The mean curvature, is defined as

$$\begin{aligned} 2H &= \nabla\cdot\frac{\nabla Z}{\left[1+|\nabla Z|^2\right]^{1/2}} \\ &= \frac{\nabla^2 Z}{\left[1+|\nabla Z|^2\right]^{1/2}} + \frac{\nabla Z\cdot\left(-\frac{1}{2}\right)\nabla|\nabla Z|^2}{\left[1+|\nabla Z|^2\right]^{3/2}} \\ &= \frac{\nabla^2 Z\left(1+|\nabla Z|^2\right) - \frac{1}{2}\nabla Z\cdot\nabla|\nabla Z|^2}{\left[1+|\nabla Z|^2\right]^{3/2}} \end{aligned} \tag{2–6}$$

Perturbed Equations

Observing the instability to occur as a transition from a quiescent state of no flow or no interfacial deflection to a state of flow, and taking this transition to be an infinitesimal perturbation of order ϵ of this quiescent state, thus

$$\begin{aligned} \mathbf{V} &= \epsilon\mathbf{v} \\ P &= p_0 + \epsilon p \\ \text{and } Z &= \epsilon\zeta \end{aligned} \tag{2–7}$$

where the $\mathcal{O}(0)$ velocity and interfacial deflection are zero. Substitution of 2–7 into the governing Equations 2–2, 2–5 and 2–16, and collecting the terms of common powers in

ϵ, reveals the no-flow base state to be simply

$$\partial_z p_{0j} = \rho_j \left(g + A\omega^2 \cos\omega t\right) \tag{2–8}$$

which states that the gravitational modulation is balanced by a vertical pressure gradient. The stress balance gives a condition of pressure continuity at the interface where $p_{01} = p_{02}$. The expansion of dependent variables located at $z = Z(x, y, t)$ is attained with

$$u = u_0 + \epsilon \left(u_1 + \zeta \partial_z u_0\right) + \frac{1}{2}\mathcal{O}\left(\epsilon^2\right)$$

in order to map the variables from the unknown interface position to $z = 0$ (see Johns & Narayanan [46]). Collection of the $\mathcal{O}(\epsilon)$ terms generates the linearized domain problem

$$\rho_j \partial_t \mathbf{v}_j = -\nabla p_j + \mu_j \nabla^2 \mathbf{v}_j \tag{2–9}$$

and the kinematic condition and stress balance at z=0, i.e.,

$$\partial_t \zeta = w \tag{2–10}$$

and

$$[\![-\left(p_j + \zeta \partial_z p_0\right)\mathbf{I} + \mu_j \left(\nabla \mathbf{v_j} + (\nabla \mathbf{v_j})^{\mathsf{T}}\right)]\!] \cdot \mathbf{n} = \gamma \nabla^2 \zeta \mathbf{n}. \tag{2–11}$$

The two tangential components of the stress balance can be combined with continuity to obtain the condition

$$\mu_1 \left(\partial_{zz} - \nabla_H^2\right) w_1 = \mu_2 \left(\partial_{zz} - \nabla_H^2\right) w_2. \text{ at } z = 0 \tag{2–12}$$

where $\nabla_H = \mathbf{i}\partial_x + \mathbf{j}\partial_y$ is the horizontal divergence. The normal component of the stress balance becomes

$$[\![-p_j + \zeta \partial_z p_0 + 2\mu_j \partial_z w_j]\!] = \gamma \nabla_H^2 \zeta \text{ at } z = 0 \tag{2–13}$$

and applying ∇_H^2 to this results in

$$[\![-\nabla_H^2 p_j + \nabla_H^2 \zeta \partial_z p_0 + 2\mu_j \nabla_H^2 \partial_z w_j]\!] = \gamma \nabla_H^4 \zeta \text{ at } z = 0. \tag{2–14}$$

An expression for $\nabla_H^2 p_j$ can be evaluated by applying $\nabla_H \cdot$ to the perturbed domain Equations 2–9

$$\nabla_H^2 p_j = \left(\rho_j \partial_t - \nabla^2\right) \partial_z w_j \tag{2–15}$$

noting that via continuity we have $\nabla_H \cdot \mathbf{v_j} = -\partial_z w_j$. Substitution of 2–15 and the base pressure gradient 2–8 into 2–14 yields

$$[\![\left(-\rho_j \partial_t + \mu_j \nabla^2 + 2\mu_j \nabla_H^2\right) \partial_z w_j + \rho_j \left(g + A\omega^2 \cos \omega t\right) \nabla_H^2 \zeta]\!] = \gamma \nabla_H^4 \zeta \text{ at } z = 0. \tag{2–16}$$

The temporal evolution of this equation for a given imposed amplitude A and frequency ω ultimately determines the stability of the linear system. It may be noted that the kinematic condition 2–10 relates w in terms of ζ thereby yielding a homogeneous problem in ζ.

Linear Stability Analysis

The perturbed system is analyzed by considering horizontally spatial modes with wavenumber k. A term with two derivatives in time arises from the perturbed pressure field, but the appearance of $\cos \omega t$ via the base pressure gradient prevents us from expressing the state variables in pure exponential time modes with growth rates, σ. Instead the periodicity of the system must be accounted for by including a Floquet exponent σ, possibly complex, in the infinite Fourier series. The Fourier series is written in modes of the basic frequency, ω, for convenience. Accounting for both the horizontal spatial and temporal dependence of the system, for every dependent variable, ψ, we write

$$\psi = e^{i\mathbf{k}\cdot\mathbf{r}} \sum_{n=-\infty}^{\infty} e^{[\sigma + i(\alpha + n\omega)]\tau} \hat{\psi}_n(z) \tag{2–17}$$

To evaluate the z-derivatives of w in 2–16, the domain perturbed velocity profile must be calculated. Applying $\nabla \times \nabla \times$ to the domain Equation 2–9, the pressure field is eliminated, yielding

$$\left(\rho_j \partial_t - \mu_j \nabla^2\right) \nabla^2 \mathbf{v}_j = 0. \tag{2–18}$$

Substitution of the expansion 2–17 into the z-component, the fourth-order ordinary differential equation governing each Fourier mode, n, for w is

$$\left[\sigma + i\left(\alpha + n\omega\right) - \nu_j\left(\partial_{zz} - k^2\right)\right] w_{jn} = 0, \tag{2–19}$$

to which the solutions are

$$w_{jn} = a_{jn}\mathrm{e}^{kz} + b_{jn}\mathrm{e}^{-kz} + c_{jn}\mathrm{e}^{q_{jn}z} + d_{jn}\mathrm{e}^{-q_{jn}z} \tag{2–20}$$

with

$$q_{jn}^2 = k^2 + \frac{\sigma + i\left(\alpha + n\omega\right)}{\nu_j}$$

where $\nu = \frac{\mu}{\rho}$ is the kinematic viscosity. In the case of $\sigma + i\left(\alpha + n\omega\right) = 0$ the functions containing q_{jn} are replaced with $z\mathrm{e}^{kz}$. The boundary conditions determine the coefficients in 2–20. The no-flow and no-slip boundary conditions on the bottom and top surfaces are,

$$w_{1n} = \partial_z w_{1n} = 0 \quad \text{at} \quad z = -h_1$$
$$\text{and } w_{2n} = \partial_z w_{2n} = 0 \quad \text{at} \quad z = h_2$$

and at the interface z=0,

$$\begin{aligned} w_{1n} &= w_{2n} \\ \partial_z w_{1n} &= \partial_z w_{2n} \\ \mu_1\left(\partial_{zz} w_{1n} + k^2\right) &= \mu_2\left(\partial_{zz} w_{2n} + k^2\right) \\ \text{and } w_{1n} = w_{2n} &= \left(\sigma + i\left(\alpha + n\omega\right)\right)\zeta_n \end{aligned}$$

hold. The pressure p in 2–16 can be replaced with an expression including the vertical velocity component w using the x and y components of the perturbed equations of motion along with continuity, and the final form of the normal component of the stress balance for each Fourier mode n is then

$$\begin{aligned} \left[\!\left[\left(\rho_j\left(\mu + i\left(\alpha + n\omega\right)\right) + 3\mu_j k^2\right)\partial_z w_n - \mu_j \partial_{zzz} w_n\right]\!\right] + \left(\Delta\rho g - \gamma k^2\right) k^2 \zeta_n \\ = A\omega^2 \frac{\Delta\rho k^2}{2}\left(\zeta_{n+1} + \zeta_{n-1}\right). \end{aligned} \tag{2–21}$$

The identity $\cos\omega t = \frac{1}{2}\left(e^{i\omega t} + e^{-i\omega t}\right)$ has been used, resulting in the coupling of the n^{th} Fourier mode ζ_n to the $n+1$ and $n-1$ modes. The linear stability of the system is solely governed by the infinite series of equations given by 2–21, and substitution of the derivatives calculated from 2–20 gives a series of coupled linear equations homogeneous in ζ_n. Truncated to a finite number of modes N, with the growth constant σ set to zero, the stability of the linearized problem can be cast as an eigenvalue problem for solutions of neutral stability and their corresponding eigenvalues being the amplitudes A at which they occur, expressed as

$$\mathcal{D}\boldsymbol{\zeta} = A\mathcal{B}\boldsymbol{\zeta}. \tag{2–22}$$

Here the matrix $\mathcal{D}$ is generated by the l.h.s. of 2–21 and operates on the eigenvector $\boldsymbol{\zeta}$. The response frequency α is set to zero in 2–21 for harmonic solutions and to $\frac{1}{2}\omega$ for subharmonic solutions. The matrix $\mathcal{B}$ is a double banded matrix of largely 1's and 0's used to select the coupled modes $\boldsymbol{\zeta}$, but differs slightly for the $n = 0$ mode. Truncation

from n=0 to N results in the inclusion of the ζ_{-1} coefficient in the matrix $\mathcal{B}$ for the $n = 0$ mode and is replaced with the conjugate $\overline{\zeta_1}$ for $\alpha = 0$ and $\overline{\zeta_0}$ for $\alpha = \frac{\omega}{2}$, by virtue of the time symmetry of the expansion 2–17. For $\alpha = 0$, 2–22 becomes

$$\begin{bmatrix} D_0^r & -D_0^i & 0 & 0 & 0 & 0 & \\ D_0^i & D_0^r & 0 & 0 & 0 & 0 & \\ 0 & 0 & D_1^r & -D_1^i & 0 & 0 & \\ 0 & 0 & D_1^i & D_1^r & 0 & 0 & \\ 0 & 0 & 0 & 0 & D_2^r & -D_2^i & \\ 0 & 0 & 0 & 0 & D_2^i & D_2^r & \\ & & & & & & \ddots \end{bmatrix} \begin{bmatrix} \zeta_0^r \\ \zeta_0^i \\ \zeta_1^r \\ \zeta_1^i \\ \zeta_2^r \\ \zeta_2^i \\ \vdots \end{bmatrix} = A \begin{bmatrix} 0 & 0 & 2 & 0 & 0 & 0 & \\ 0 & 0 & 0 & 0 & 0 & 0 & \\ 1 & 0 & 0 & 0 & 1 & 0 & \\ 0 & 1 & 0 & 0 & 0 & 1 & \\ 0 & 0 & 1 & 0 & 0 & 0 & \\ 0 & 0 & 0 & 1 & 0 & 0 & \\ & & & & & & \ddots \end{bmatrix} \begin{bmatrix} \zeta_0^r \\ \zeta_0^i \\ \zeta_1^r \\ \zeta_1^i \\ \zeta_2^r \\ \zeta_2^i \\ \vdots \end{bmatrix}$$

and for $\alpha = \omega/2$

$$\begin{bmatrix} D_0^r & -D_0^i & 0 & 0 & 0 & 0 & \\ D_0^i & D_0^r & 0 & 0 & 0 & 0 & \\ 0 & 0 & D_1^r & -D_1^i & 0 & 0 & \\ 0 & 0 & D_1^i & D_1^r & 0 & 0 & \\ 0 & 0 & 0 & 0 & D_2^r & -D_2^i & \\ 0 & 0 & 0 & 0 & D_2^i & D_2^r & \\ & & & & & & \ddots \end{bmatrix} \begin{bmatrix} \zeta_0^r \\ \zeta_0^i \\ \zeta_1^r \\ \zeta_1^i \\ \zeta_2^r \\ \zeta_2^i \\ \vdots \end{bmatrix} = A \begin{bmatrix} 1 & 0 & 1 & 0 & 0 & 0 & \\ 0 & -1 & 0 & 1 & 0 & 0 & \\ 1 & 0 & 0 & 0 & 1 & 0 & \\ 0 & 1 & 0 & 0 & 0 & 1 & \\ 0 & 0 & 1 & 0 & 0 & 0 & \\ 0 & 0 & 0 & 1 & 0 & 0 & \\ & & & & & & \ddots \end{bmatrix} \begin{bmatrix} \zeta_0^r \\ \zeta_0^i \\ \zeta_1^r \\ \zeta_1^i \\ \zeta_2^r \\ \zeta_2^i \\ \vdots \end{bmatrix}$$

The solution of Equation 2–22 yields a set of amplitude eigenvalues A, for which the lowest real eigenvalue corresponds to the first excited mode in a physical system when the forcing amplitude is gradually increased from zero upward (cf. Kumar & Tuckerman [52]).

Spatially Infinite System Results and Discussion

Solving the linearized problem for all wavenumbers k is a set of tongues of instability similar to the fins produced by the Mathieu equation[11][63] (see A, but with the tips smoothed by viscosity and not descending to zero amplitude, cf. Figure

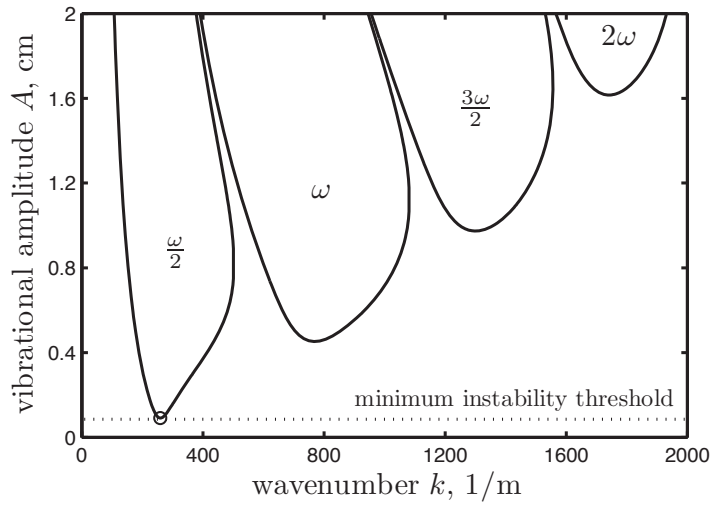

Figure 2-1. Fixed-frequency linear stability threshold for a horizontally infinite bilayer. System fluids are FC70 (1880 kg m^{-3}, 12 cSt) and silicone oil (846 kg m^{-3}, 1.5 cSt) with h_1=h_2=0.5 cm, and frequency f=$\omega/2\pi$=9 Hz. Interfacial tension estimated to be 7 dyn cm^{-1} [75].

2-1. For these calculations N was taken to be 12. The linear system response arising from these tongues alternates between subharmonic (α=$\frac{\omega}{2}$) and harmonic (α=0), where the first tongue is subharmonic. To make a clarification that is important to an experiment, we refer to the first tongue as subharmonic, the second as harmonic, and the third as superharmonic, as the waves excited in these regions execute one-half, one, and one-and-a-half periods per cell period, respectively. In an experimental system that approaches the laterally infinite limit like that of Bechhoefer *et al*.[8], the wavenumber with the lowest threshold amplitude would be excited first in a series of trials of increasing vibrational amplitudes. In Figure 2-1 the minimum threshold occurs at A=0.091 cm with a wavenumber k of 259.5 m^{-1}. A sample MATLAB® code generating this threshold is presented in Appendix B.

Figures 2-2 presents several examples of how tongue behavior is altered by common system parameters. Pictured in Figure 2-2 (a) is the effect of increasing the parametric frequency. It is clear that increasing frequency causes a shift of all tongues towards high wavenumbers, which is a result of the system requiring a wavenumber with

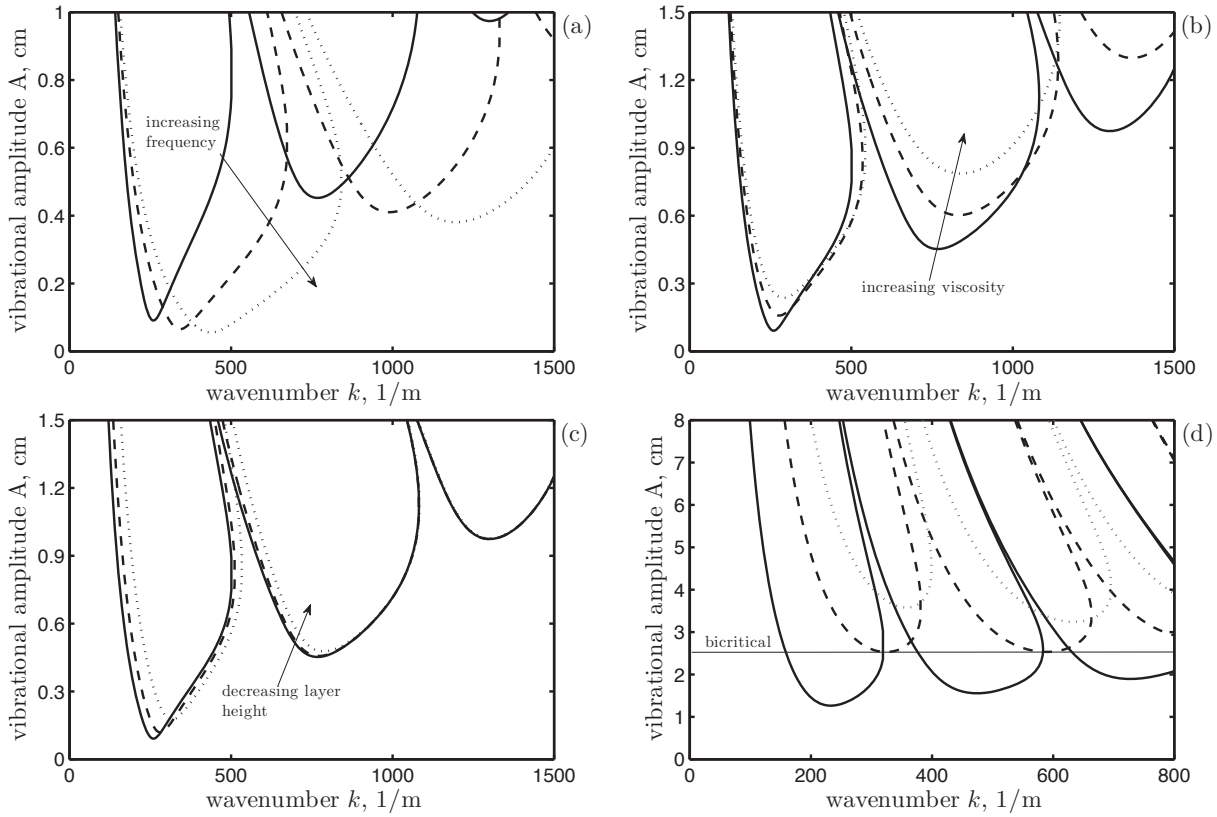

Figure 2-2. Fixed-frequency stability dependence upon various system parameters. Predictions are for FC70 and 1.5 cSt silicone oil bilayers for (a) h_1=h_2=5 mm at f=9, 11, 13 Hz; (b) h_1=h_2=5 mm and f=9 Hz with ν_2=1.5, 20, 50 cSt; (c) h_1=h_2=5, 3, 1 mm at f=9 Hz and (d) h_1=h_2= 1.5, 1.3, 1.1 mm at f=5 Hz. Physical parameters are the same as in Figure 2-1.

a higher natural frequency to meet the resonant condition. This occurs by selection of higher wavenumbers with greater capillary contribution. This selection can be predicted in general using the inviscid dispersion relation for single [11] and double layer [52] systems. While here the minimum threshold decreases, it will be shown later and explained that increases with respect to increasing frequency are possible as well.

The effect of increasing fluid viscosity is shown in Figure 2-2 (b), where the upper layer silicone oil viscosity is increased from 1.5 to 20 to 50 centiStokes. It is seen that the increase in viscosity causes a damping of the tongues, raising the minimum thresholds. Tongue damping is greater for the higher harmonic tongues, due to the

increased viscous effect of higher wavenumber, choppier waves. Additionally, slight shifts toward higher wavenumbers are observed.

Figures 2-2 (c) and (d) present the complex effect of layer height. There exists a deep layer limit beyond which larger heights do not show any effect on the onset threshold. It is well explained mathematically by the $\tanh kH$ term in the single fluid inviscid theory (see Appendix A). Figure 2-2 (c) shows that lowering the layer heights h_1=h_2= 5 to 4 and to 3 mm causes shift of the first subharmonic tongue toward higher wavenumbers, and threshold amplitudes. Observing that resonance is obtained on account of a gravitational as well as capillary contribution, it is therefore apparent that a reduced gravitational effect leads to a greater capillary contribution. The effect of height saturates as wavenumber is increased and the stability diagrams coincide with each other at sufficiently high wavenumbers.

Lowering the layer heights to extreme values especially causes interesting behavior, where the harmonic tongue can become more unstable than the first subharmonic tongue. This is seen in Figure 2-2 where the layer heights h_1=h_2 are decreased from 1.5 to 1.3 to 1.1 mm. Upon performing a calculation for a lower frequency of 5 Hz where inertial effects should be controlling, it is seen, for the 1.1 mm case, that the harmonic tongue is the least stable. In the 1.3 mm case the subharmonic and harmonic minima are positioned at nearly identical amplitudes, giving rise to a co-dimension 2 point. This behavior, due to diminished inertial effects and increased viscous film effects, was first predicted by Kumar [51]. The harmonic response with a thin layer was confirmed experimentally by Müller *et al.* [62], and a nonlinear pattern forming study of the co-dimension 2 point was done by Wagner *et al.* [80].

The theoretical curve matched by Bechhoefer *et al.*[8] can be generated by calculating the minimum point in Figure 2-1 for a range of frequencies, noting that their curves depict forcing acceleration, $A\omega^2$, instead of forcing amplitude, A. An example of this calculation is given in Figure 2-3 (a) for several different layer heights, while the

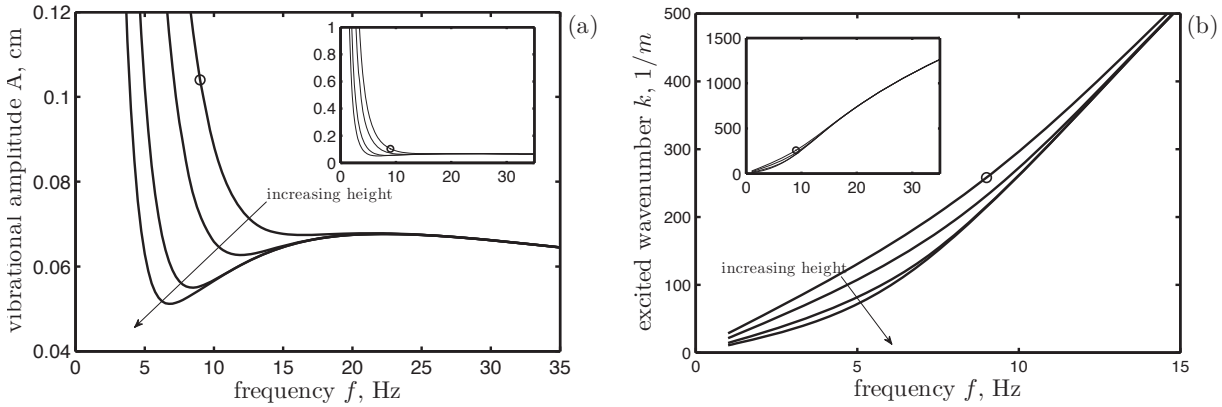

Figure 2-3. Minimum threshold dependence upon frequency for horizontally infinite bilayers. Shown is the dependence of the (a) threshold amplitude and (b) wavenumber selection for FC70 and silicone oil bilayers of h_1=h_2=0.75, 1, 1.5 and 2.5 cm. Physical parameters are the same as in Figure 2-1. Circled point denotes the first excited mode from Figure 2-1.

corresponding wavenumber selection is shown in 2-3 (b). It can be seen that the general behavior of these curves depends upon the layer height. At low forcing frequency the minimum threshold increases without bound as frequency is decreased, agreeing with intuition that a light over heavy system is stable. Increasing the forcing frequency causes a sharp drop in the minimum threshold amplitude. For systems of large layer height the threshold can drop to a minimum value before rising and then dropping again. The wavenumber selection in Figure 2-3 (b) shows that for lower layer heights wavenumber selection is higher. The shift toward higher wavenumbers arises from the diminished inertial effect due to the density jump across the interface from which resonance is achieved resulting in a greater capillary contribution. Higher wavenumbers feel greater viscous effects and this is seen in the rises in the threshold present in the systems of h_1=h_2=1, 1.5, and 2.5 cm in Figure 2-3 (a). For the h_1=h_2=0.75 cm case, the height is sufficiently low such that the viscous effects are important at much lower frequencies than in the other cases, and a local minimum in the threshold curve is therefore barely seen.

Spatially Finite Systems

Extension of this model to the case of a cell with finite lateral dimension permitting separation of horizontal spatial dimension was outlined by Benjamin & Ursell [11] for both rectangular and cylindrical cross-sections. They applied these conditions to their stability results generated by the Mathieu equation, and the application to the viscous model is much the same. For a system with a rectangular cross-section of width W and breadth L, the surface waves must satisfy the boundary conditions

$$\frac{\partial \zeta}{\partial x} = 0 \text{ and } \frac{\partial \zeta}{\partial y} = 0$$

at the $x = 0$ and W and $y = 0$ and L sidewalls, respectively. These constraints discretize the wavenumber selection to those which form 90° angles at the sidewalls. Functions that follow this constraint take the form of trigonometric functions of the horizontal directions, viz.,

$$\begin{aligned} \zeta(x, y) &= \hat{\zeta} \cos k_x x \cos k_y y \\ \text{with } k_x &= \frac{\pi n}{W} \text{ and } k_y = \frac{\pi m}{L} \end{aligned} \tag{2–23}$$

where n and m increase from zero to infinity. Defining $k^2 = k_x^2 + k_y^2$, and specifying a square cross-section i.e., $W = L$, a series of dimensionless wavenumbers can be written for increasing n and m, viz. $k_{nm}W = \pi\left(n^2 + m^2\right)^{\frac{1}{2}}$, producing $k_{0,1}W$=3.14, $k_{1,1}W$=4.443, $k_{0,2}W$=6.283, $k_{1,2}W$=7.025, $k_{2,2}W$=8.886, and $k_{0,3}R$=9.425 and so on. This series specifies the wavenumbers allowed in Figure 2-1 for a finite cell of square cross-section.

For the cylindrical case, the allowed eigenfunctions $\zeta_m = \zeta(r, \theta)$ are given by the functions satisfying

$$\left(\frac{\partial^2}{\partial r^2} + \frac{1}{r}\frac{\partial}{\partial r} + \frac{1}{r^2}\frac{\partial}{\partial \theta} + k_m^2\right)\zeta_m = 0$$

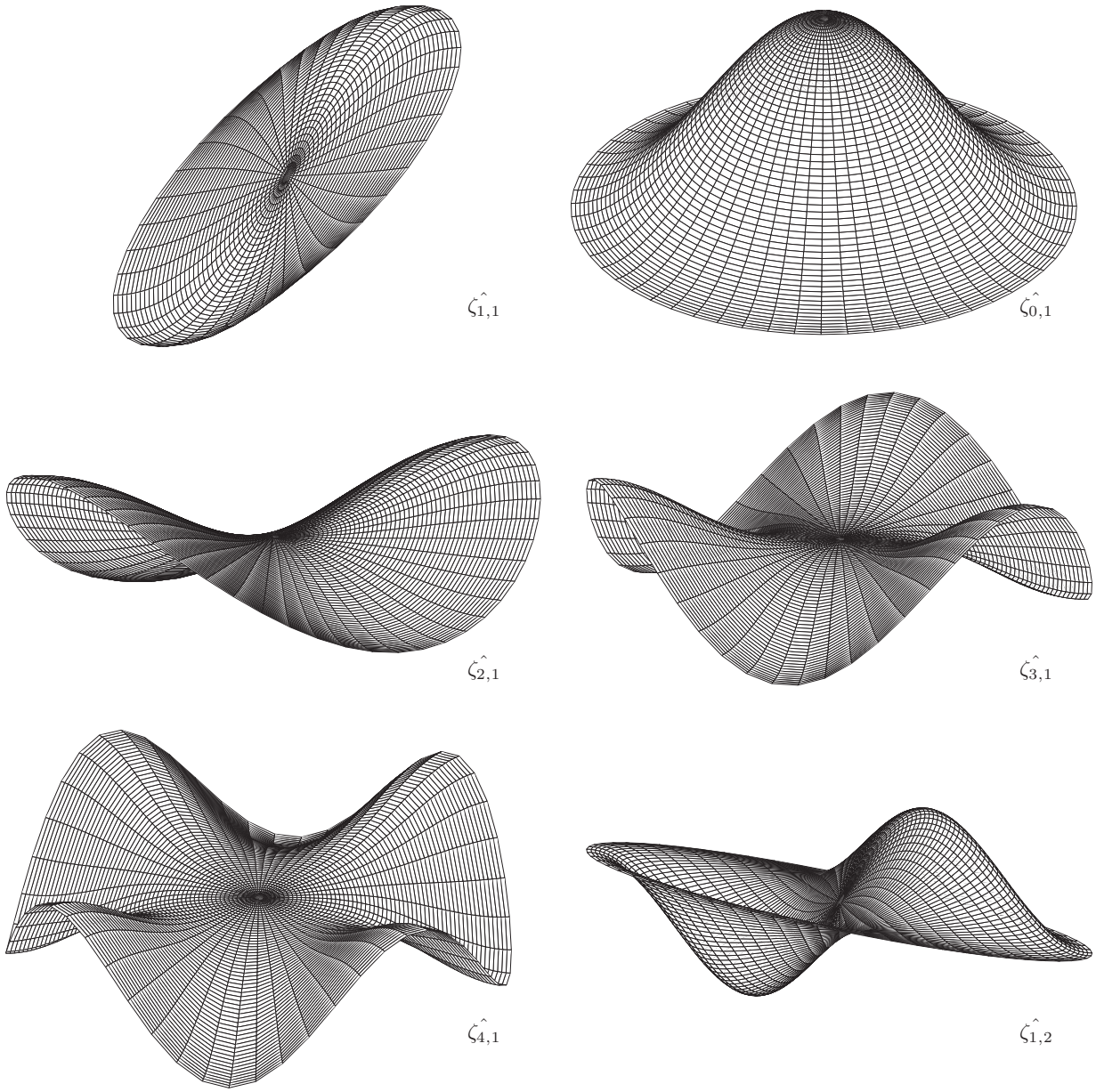

Figure 2-4. Cylindrical cell modes and wavenumbers satisfying the stress-free condition.

which can be decomposed as

$$\hat{\zeta_{l,m}} = J_l\left(k_{l,m}r\right)\sin l\theta \tag{2–24}$$

where $k_{l,m}$ is the mth zero of $J_l'\left(k_{l,m}R\right)$, R being the container radius. The indices l and m, indicate the number of azimuthal and radial nodes, respectively. The spatial

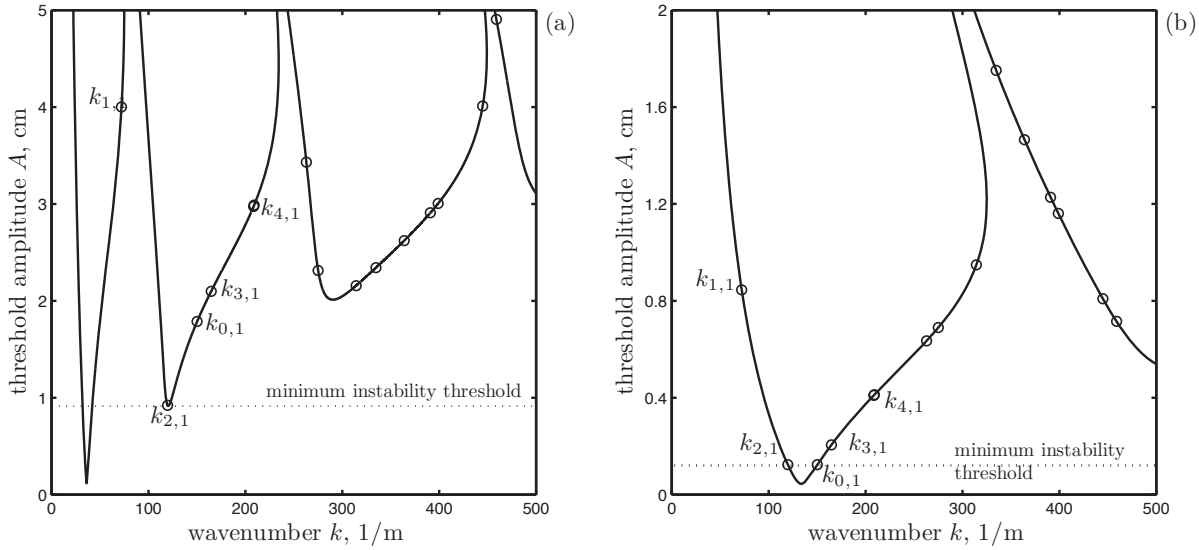

Figure 2-5. Fixed-frequency linear stability of systems with cylindrical mode discretization. Predictions are for a FC70 and silicone oil bilayer of h_1=3.1 cm and h_2=3.3 cm oscillated at frequencies of (a) 3.3 Hz and (b) 7.045 Hz. Circled thresholds correspond to the allowed set of discrete wavenumbers for a cylindrical container of R=2.55 cm. Physical parameters are the same as in Figure 2-1.

form of the various cylindrical linear modes $\zeta_{l,m}$ are presented in Figure 2-4, and the non-dimensionalized values of $k_{l,m}R$ for these modes are $k_{1,1}R$=1.841, $k_{2,1}R$=3.054, $k_{0,1}R$=3.832, $k_{3,1}R$=4.201, $k_{4,1}R$=5.318, and $k_{1,2}R$=5.331 [1].

The critical thresholds corresponding to these allowed modes (in addition to higher index modes) have been labelled on stability diagrams of two different frequencies in Figures 2-5 (a) and (b). Here it is apparent that the wavenumber corresponding to the subharmonic minimum threshold is excited only in the case where it coincides with one of the allowed modes. Harmonic, and ever more, superharmonic excitation is uncommon at high frequencies, but at low frequencies in a discretized system one can potentially skip the first subharmonic tongue and excite harmonic and superharmonic modes, as in Figure 2-5 (a), where the $(2,1)_h$ mode would be excited first at an amplitude of 0.92 cm. The stability diagram of Figure 2-5 (b) was calculated for a carefully chosen frequency to highlight the appearance of a co-dimension 2 point, a set of conditions where two modes

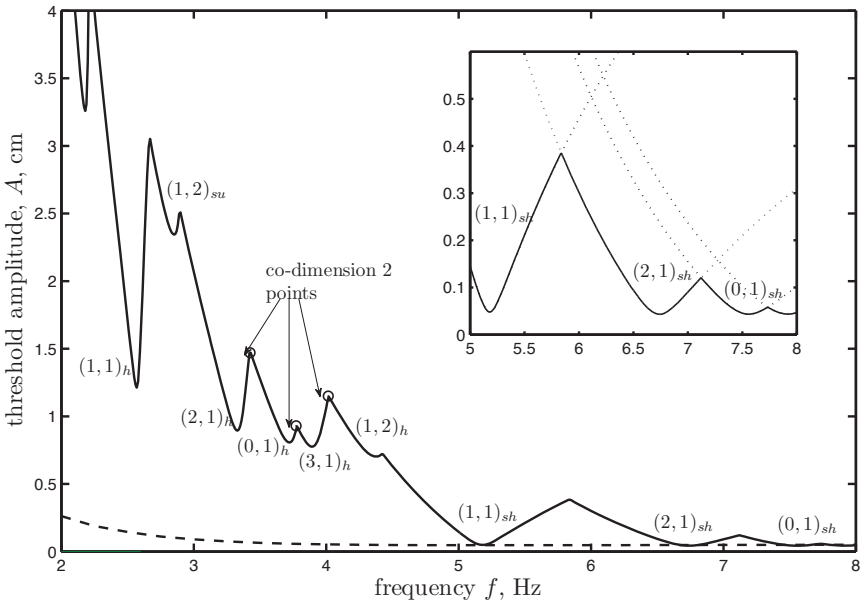

Figure 2-6. Minimum threshold dependence upon frequency for a cylindrical system. Predictions are for a bilayer of FC70 (1916 kg m^{-3}, 12 cSt, h_1=3.1 cm) and silicone oil (846 kg m^{-3}, 1.5 cSt, h_2=3.3 cm) in both an infinite system (dashed line) and cylindrical R=2.55 cm system. Subscripts *sh*, *h* and *su* represent subharmonic, harmonic, and superharmonic modes.

are both neutrally stable for the same amplitude and frequency. Here, both $(2,1)_{sh}$ and $(0,1)_{sh}$ modes are simultaneously excited at an amplitude of 0.123 cm.

Combined in Figure 2-6 are all of the discussed aspects of discretization, where the minimum amplitudes of instability from calculations such as Figure 2-5 are plotted versus a multitude of frequencies for a cylindrical system. Present are the overlapping dips of instability for each mode, descending to minimum thresholds. Each dip corresponds to a single mode $\zeta_{l,m}$ specified by Equation 2–24. When positioned at one of the local minima, slight adjustment to a lower or higher frequency causes the threshold to rise as the resonant transfer of energy to the wave becomes less efficient. The modes excited at frequencies higher than the minima are termed tuned modes, and those at lower frequencies as detuned modes. This distinction is important because many including Benjamin & Ursell have noted different nonlinear behavior near the threshold for tuned and detuned modes, which will be discussed later in the context

of determining the experimental threshold. Further departure from a local minimum results in the intersection with an adjacent mode. These intersections, or cusps, are the co-dimension 2 points highlighted by Figure 2-5 (b). The general ordering of the modes is dictated by the wavenumber, where at low frequencies harmonic and superharmonic modes are prevalent, followed by subharmonic modes at the higher range. The physical parameters used to calculate Figure 2-6 are the same as in one of the experiments of this study, and one result of this is the viscous damping of sharp resonances at low frequencies entering from the higher harmonic tongues. One of the benefits of using a viscous system is a series of well-spaced modes, resulting from the damping of resonances of higher harmonic tongues. It will be shown in the next section that the use of less viscous systems, typical of previous work, makes individual modes more difficult to discern due to the inclusion of these higher harmonics. Included for comparison in Figure 2-6 is the infinite system threshold, much like Figure 2-3 (a). At large frequencies the finite system threshold is very nearly identical to the infinite threshold and continued increase in frequency causes the merging of the two.

A Case Study: the Effect of Gravity

An example demonstrating the predictive capabilities of the model is comparison of its application to identical systems based on earth and microgravity environments, highlighting the role of gravity on the instability threshold. A relevant application is the propellant in a rocket fuel tank, whereupon vibrations during take-off are known to induce Faraday initialized sloshing Ibrahim [42].

In the context of the Rayleigh-Taylor instability, also driven by a density contrast across two phases, one intuitively knows that gravity has a destabilizing effect on the system's stability. This stands in contrast with the Faraday system, where it is found that gravity not only possesses a destabilizing effect akin to its role in the Rayleigh-Taylor instability, but its contribution to the natural frequency of a mode results in a shift toward higher wavenumbers when it is removed, as seen in Figure 2-7 (a). Here, the system is

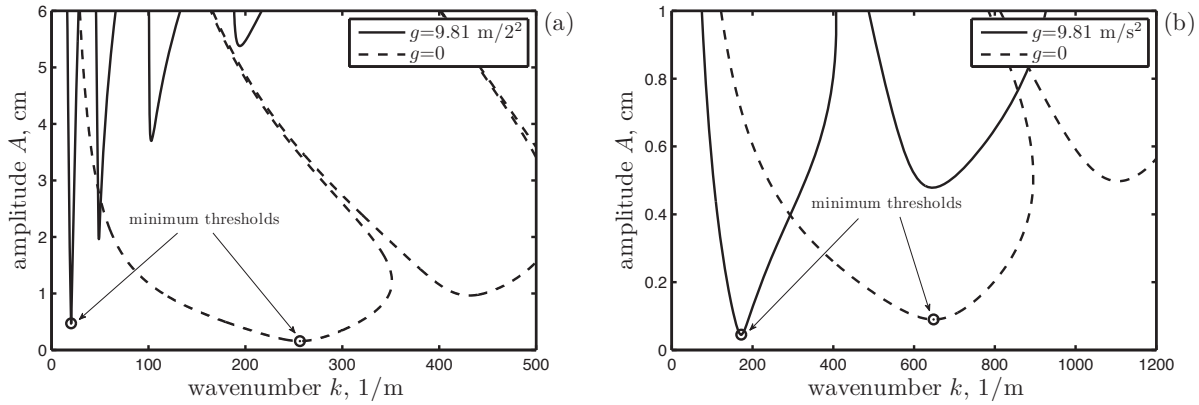

Figure 2-7. Fixed-frequency linear stability in earth-based and zero-gravity environments. Systems are infinite bilayers of FC70 and 1.5 cSt silicone oil with h_1=h_2=3 cm oscillating at f=(a) 2 Hz and (b) 8 Hz.

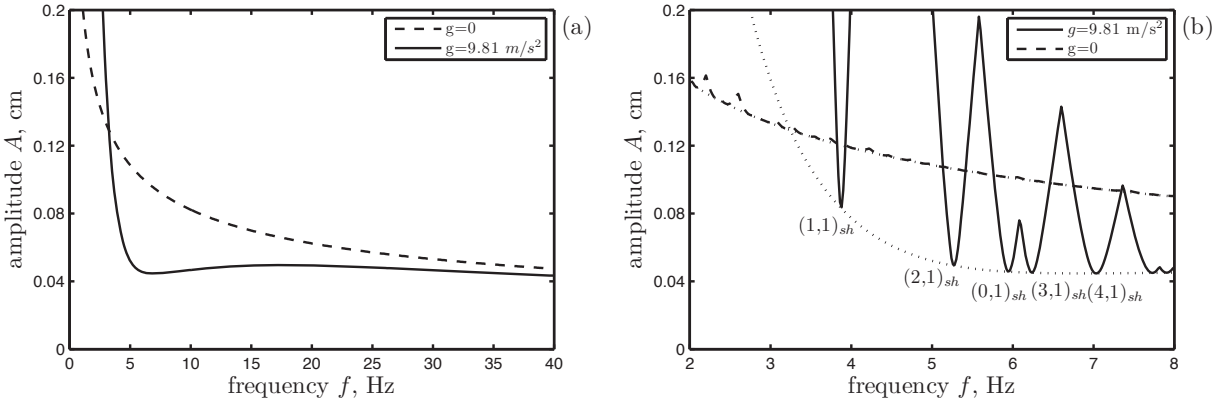

Figure 2-8. Minimum threshold in earth-based and zero-gravity environments. Predictions are for FC70 and 1.5 cSt silicone oil bilayers as (a) infinite systems and (b) a R=4 cm cylindrical cell. System parameters are identical to those of Figure 2-7.

oscillated at a frequency where zero-g minimum threshold is lower than its earth-based value, following the Rayleigh-Taylor justification. However the opposite is seen in Figure 2-7 (b), where the same system is oscillated at a higher frequency, and the shift towards a higher wavenumbers is accompanied by an increase in the minimum threshold. It is therefore apparent there exists a frequency where the zero gravity system transitions from being less to more stable than the earth-based system.

This crossover in the minimum threshold is depicted in Figure 2-8 (b) and results from increased viscous effects due to higher wavenumber selection in zero-g systems.

At large frequencies the zero-g system will continue to select higher wavelengths, at therefore greater thresholds as well. Given that the crossover typically occurs at low frequencies where discretization are significant, the thresholds for a small cylindrical cell are depicted in Figure 2-8. In the discretized system the notion of the crossover frequency becomes more ambiguous as multiple cell modes in the earth-based system become less and then more stable than the zero-g system before the zero-g system becomes consistently more stable. It is also worth noting that in the zero-g cell the effects of discretization are minimized, as the wavenumber selection has been shifted into a region of the spectrum with smaller spacing.

The Case of Double-Frequency Parametric Forcing

The instability may also be excited with parametric forcing composed of two separate frequencies. Following the single-frequency analysis, predictions can be made for both horizontally infinite systems and also those in small containers when subjected to a motion with two frequency components. The addition of a second frequency component naturally adds three degrees of freedom to the problem: an amplitude, frequency, and phase lag of the second component. First presented theoretically by Besson *et al.* [12], these degrees of freedom were accounted for by writing the forcing function as

$$\begin{aligned} d(t) &= A\left[\cos\chi\cos\left(M_1\omega\tau\right)+\sin\chi\cos\left(M_2\omega\tau+\phi\right)\right] \\ a(t) &= A\omega^2\left[M_1^2\cos\chi\cos\left(M_1\omega\tau\right)+M_2^2\sin\chi\cos\left(M_2\omega\tau+\phi\right)\right] \end{aligned} \tag{2–25}$$

in their theory, which replaces 2–2 in the single-frequency analysis. The two components are written in terms of a basic frequency ω and are denoted by the integers M_1 and M_2, and the angle ϕ specifies the phase lag. The frequency ratio χ divides the overall forcing amplitude A between the two components, and increasing from χ=0° to 90° represents a sweep from pure $M_1\omega$ to pure $M_2\omega$ excitation. Different comparative studies could be conducted by adjustment of the way the forcing function is written, for example,

replacement of the mixing angle χ and overall amplitude A with two independent amplitudes A_1 and A_2. However, when the two frequencies are written as integer multiples of a basic frequency ω, Floquet analysis identical to the single frequency case is possible. Thereby instead of each Fourier mode ζ_n coupling to the modes ζ_{n-1} and ζ_{n+1}, the double-frequency case sees each mode ζ_n being coupled to four modes, ζ_{n-M_1}, ζ_{n+M_1}, ζ_{n-M_2} and ζ_{n+M_2}. Inclusion of the new function into the analysis leading to 2–21, gives the new form of each Fourier component of the normal component of the stress balance to be

$$\begin{aligned}&[\![\left(\rho_j\left(\mu+i\left(\alpha+n\omega\right)\right)+3\mu_j k^2\right)\partial_z w_n-\mu_j\partial_{zzz}w_n]\!]+\left(\Delta\rho g-\gamma k^2\right)k^2\zeta_n\\&=A\omega^2\frac{\Delta\rho k^2}{2}\left(\sin\left(\chi\right)\left(\zeta_{n+M_1}+\zeta_{n-M_1}\right)+\cos\left(\chi\right)\left(e^{i\phi}\zeta_{n+M_2}+e^{-i\phi}\zeta_{n-M_2}\right)\right).\end{aligned}\tag{2–26}$$

The reality conditions on ζ_n remain unchanged from the single frequency analysis. The $\mathcal{B}$ matrix of 2–22 now takes a form $\mathcal{B}=\sin\left(\chi\right)\mathcal{B}_{M_1}+\cos\left(\chi\right)\mathcal{B}_{M_2}$, with the integers M_1 and M_2 specifying the band spacing. The matrices $\mathcal{B}_{M_1}$ and $\mathcal{B}_{M_2}$ are given in Appendix C for both the harmonic and subharmonic cases. Again, the thresholds of neutral stability are determined from the set of eigenvalues obtained from 2–22, with the new form of the $\mathcal{B}$ matrix. Repeated solution for harmonic and subharmonic response for a range of wavenumbers k provides the familiar stability diagrams similar to 2-1.

Double-Frequency Predictions for Horizontally Infinite Systems

With a total of five degrees of freedom, a large number of comparative studies must be made to uncover the effect of addition of a second frequency component. The general effects of density, viscosity, and layer height remain unchanged from the single frequency case, however the addition of the the second component's degrees of freedom present many new phenomena. Figures 2-9 (a)-(f) depict the appearance and growth of new tongues of instability due to the addition of the second component. When χ=0°, the system is forced with a single frequency $M_1\omega$ and the stability is identical to the single frequency result of Figure 2-1. Increasing χ to 10° in Figure 2-9 (b), an island

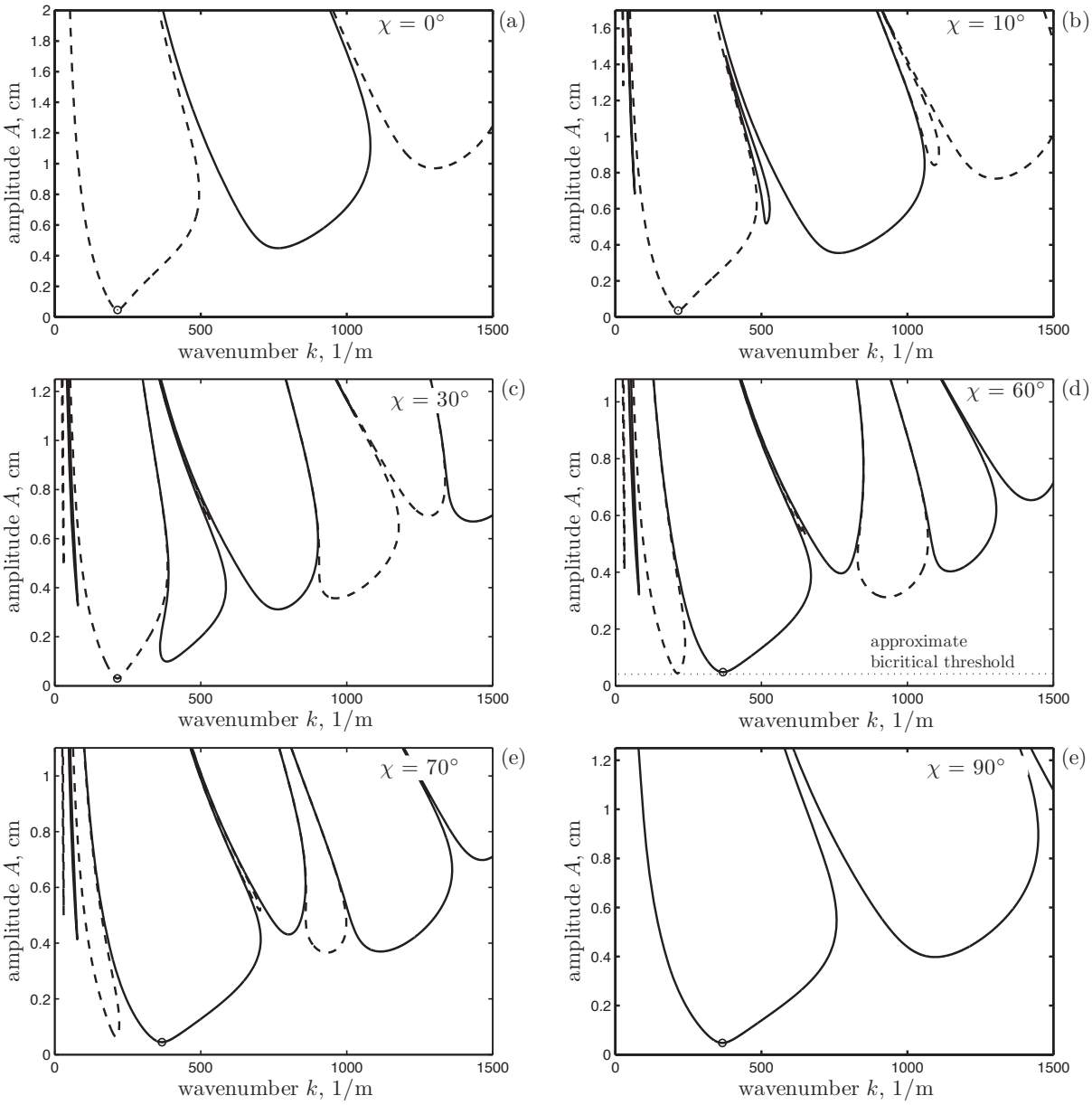

Figure 2-9. Fixed-frequency stability of infinite systems with double-frequency excitation. System at various angles χ (a)-(f) is a a h_1=h_2=3 cm bilayer of FC70 (ρ_1=1888 kg m^{-3}, 12 cSt) and 1.5 cSt silicone oil (ρ_2=846 kg m^{-3}). Basic frequency f=$\omega/2\pi$= is 3 Hz with (M_1, M_2)=(3,4).

region of instability appears between the first two original tongues, and another tongue has appeared between the original second and third tongues. Sharp resonant tongues also appear at low wavenumbers. At χ=30° the new tongues continue to appear and grow, and some of the original tongues from the single frequency result have noticeably shrunk. At χ=60° the primary harmonic tongue appearing due to the second forcing component has grown such that its minimum threshold is equally unstable with the original primary subharmonic tongue. This type of co-dimension 2 point manifests itself at a certain frequency ratio χ in any double frequency system, and the approximate angle at which is appears can be determined by setting the two accelerations of different frequency equal, that is,

$$\begin{aligned} A_1 \left(M_1\omega\right)^2 &= A_2 \left(M_2\omega^2\right)^2 \\ A\cos\chi M_1^2 &= A\sin\chi M_2^2 \\ \tan\chi &= \left(\frac{M_2}{M_1}\right)^2. \end{aligned}$$

For (M_1, M_2)=$(3, 4)$ forcing, bicriticality should appear at χ=60°, but due to higher damping of the main M_2 tongue, the viscous contribution gives a slightly higher angle.

Continued increase of χ past the the co-dimension 2 point in the further lessening and final disappearance of the tongues owing to the M_1 forcing. All tongues with χ=90 excitation are obtained with α=0, implying a harmonic response, and this is a result of the second frequency being an even-integer multiple of the basic frequency. The response in the first tongue is harmonic with respect to the frequency ω, but remains subharmonic with respect to $M_2\omega$.

Following the analysis for horizontally infinite systems in the single frequency case, the movement of the minimal threshold and wavenumber selection in double frequency systems is displayed in Figure 2-10 for various values of χ, and resembles the behavior of single frequency systems. The curves for χ=0 and 90° collapse onto each other when the frequencies are rescaled taking into account the values of (M_1, M_2). Figure 2-10 can

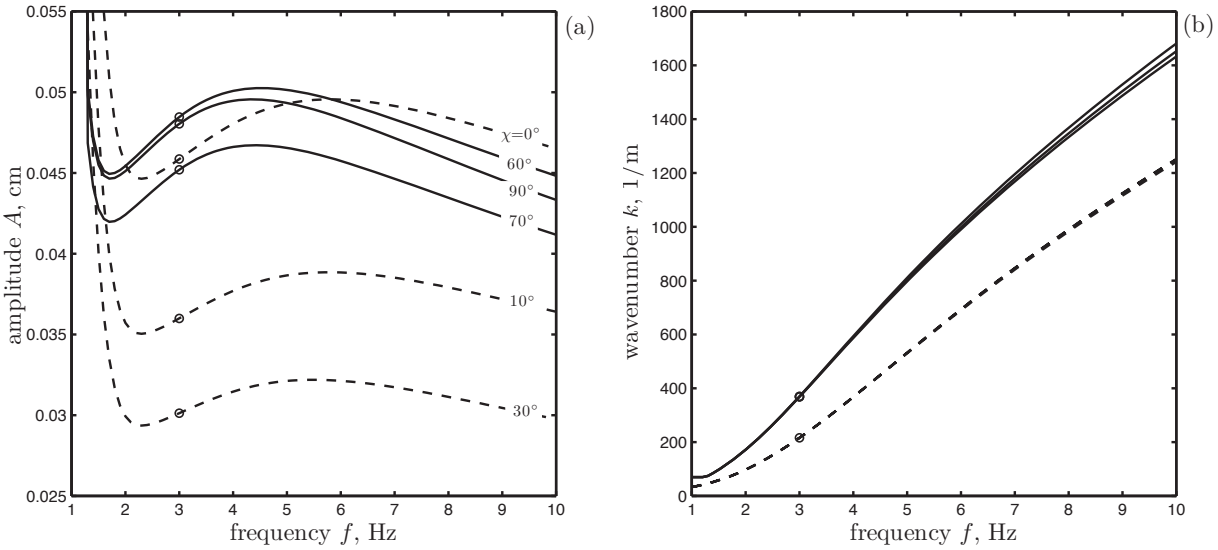

Figure 2-10. Minimum threshold dependence upon basic frequency for an infinite system. Shown is the (a) minimum threshold and (b) wavenumber selection for various forcing ratios χ with (M_1, M_2)=(3,4) for the system of Figure 2-9. Dashed lines represent subharmonic and solid lines represent harmonic thresholds. Circled points represent the tongue minima from Figure 2-9.

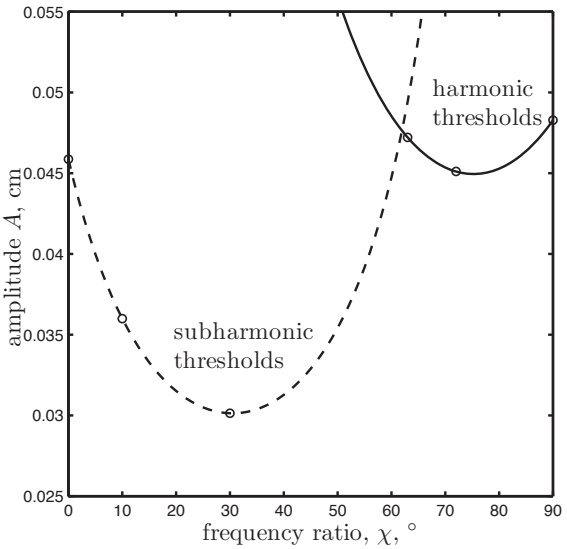

Figure 2-11. Minimum threshold dependence upon the frequency ratio χ for an infinite system. Predictions are for the system of Figure 2-9 oscillated at fixed frequency $f=\omega/2\pi$=3 Hz. Dashed lines represent subharmonic thresholds and solid lines represent harmonic thresholds. Circled points in Figure 2-10 (b) represent the wavenumber selection of the system.

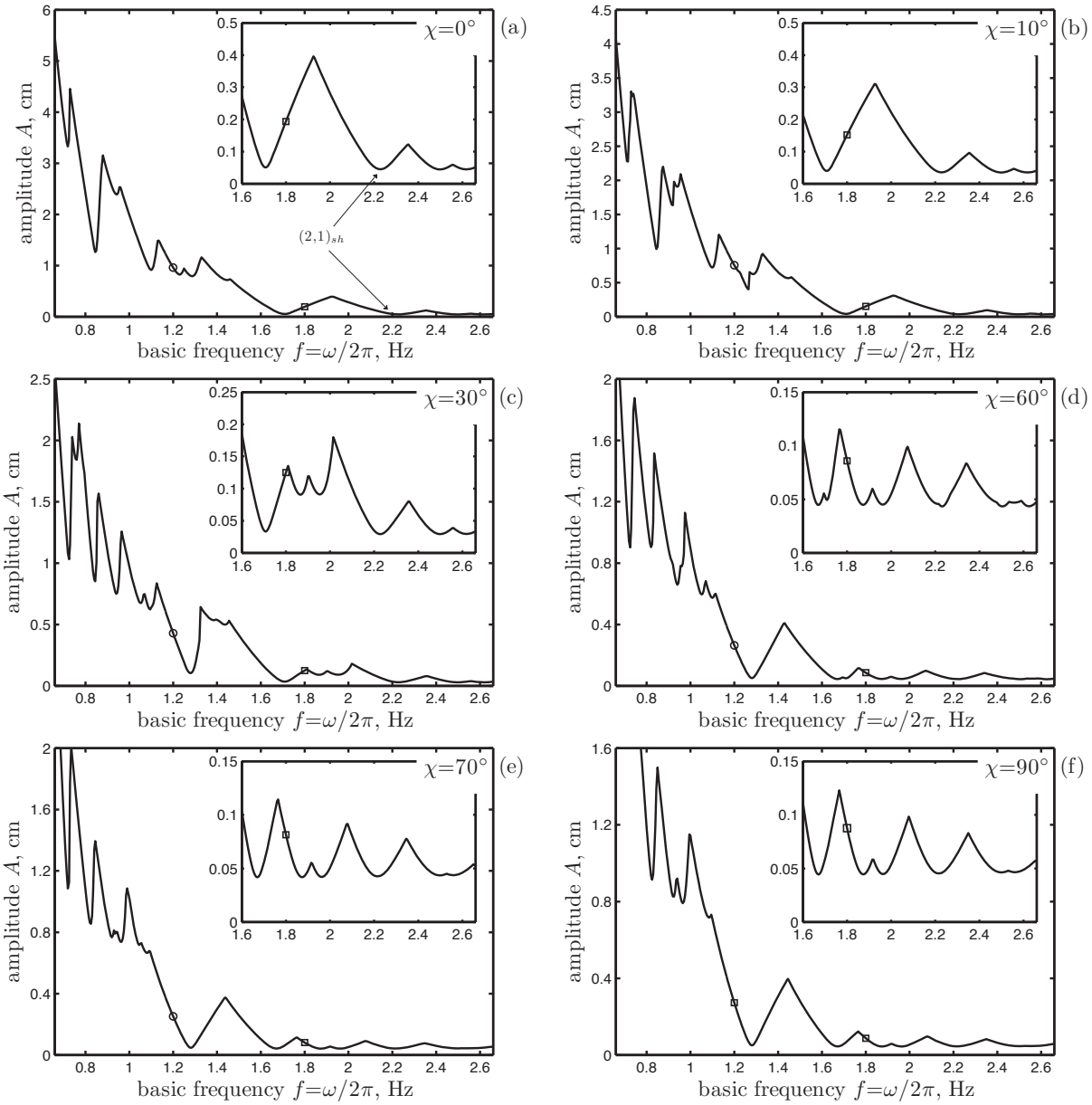

Figure 2-12. Minimum threshold dependence upon basic frequency for a cylinder. Predictions are made with various ratios χ (a)-(f) for the system of Figure 2-9 in a R=2.55 cm cylinder. The mode selection of Figures (a) and (f) follows that of Figure 2-6.

be used to deduce that an adjustment of χ can either increase or decrease the overall threshold A, and this is clearly presented in Figure 2-11 where the minimum threshold is plotted as a function of χ for a fixed frequency.

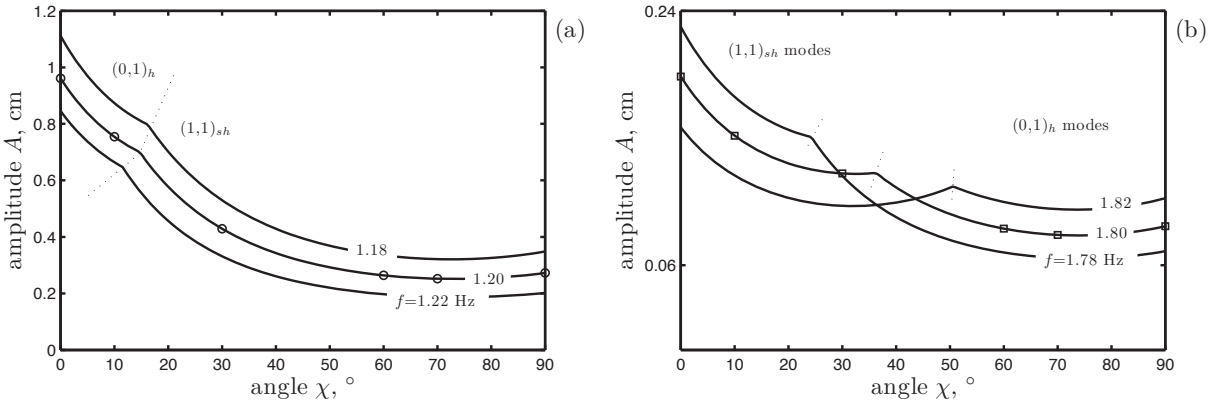

Figure 2-13. Minimum threshold dependence upon the ratio χ for a cylinder. Predictions are for basic frequencies ω of (a) 1.2 Hz and (b) 1.8 Hz in the system of 2-12. Mode selection to the left and right of the co-dimension 2 points in (a) are $(0,1)_h$ and $(1,1)_{sh}$, then $(1,1)_{sh}$ and $(0,1)_h$ in (b). Circled and squared points correspond to the thresholds from Figures 2-12 (a)-(f).

Double-Frequency Predictions for Cylindrical Containers

The adjustments made to the predictions once the modes are discretized by application of the stress-free boundary condition, as done for the single-frequency case, are presented in Figures 2-12 and 2-13. The predictions of Figures 2-12 (a) and (f) for χ=0 and 90° forcing represent single frequency forcing and can be compared directly with the single frequency predictions 2-6 to determine mode selection. Starting with χ=0°, addition of the second forcing component effectively superimposes the same set of resonant tongues, located at the M_1 component frequencies multiplied by the factor M_2/M_1. Slight interaction is seen, but the threshold amplitudes of the growing M_2 or diminishing M_1 tongues are proportional to χ. Co-dimension 2 points are therefore created for the value of χ where an M_2 threshold surpasses the M_1 tongue threshold for a given frequency. Such co-dimension 2 points are visualized in Figure 2-13 (a) and (b), which also help further to visualize the three-dimensional A=$A(f, \chi)$ stability space.

It should be noted that the purpose of this analysis has been to make predictions which pertain to the available experiment. In the experiment, the amplitude and frequency are adjusted independently, and due to this the predictions have been

reported as threshold amplitudes in contrast to threshold accelerations, which is often done in Faraday literature. For this reason it is difficult to make statements regarding whether addition of a second frequency component “stabilizes” or “destabilizes” a system, because one statement could be true for the amplitude but not the acceleration. Intuition suggests there would be cooperative and destructive effects of the two components. Another avenue that was not pursed was the effect of different integer sets (M_1, M_2). The integers (3,4) represent a close set of frequencies when compared to other possibilities with a greater difference $M_2 - M_1$. Of great experimental potential is that by tailoring the integer set (M_1, M_2), one could position any two desired modes next to each other, allowing study of their co-dimension 2 point. Lastly, the role of the phase angle was not studied. While the phase angle has been determined important to pattern formation [28], it has been reported to have very little influence on the linear stability threshold [12]. However, potential influence of the phase lag on the interaction between the experimental non-ideality and the instability will be discussed.

CHAPTER 3
PREVIOUS EXPERIMENTS ON SINGLE-MODE EXCITATION

One of the central purposes of this work is to reproduce the thresholds predicted in Figure 2-6. Several Faraday experiments were performed in small cylinders with the aim of measuring the onset of instability, in the regime where mode discretization is important. Most often the experiments investigated the stability boundary for only one or two modes in a system with limited viscous effects and the large dissipation by contrast arising from the sidewalls results in systems exhibiting non-ideal behavior. Comparison of the data from these experiments to the predictions of the model of Chapter 2 highlights many of the discrepancies in the previous experiments and raises many questions regarding the mechanisms at play causing this, to which the current study will provide new insight. In Figures 3-1 (a) through (f) the results of these works have been compared to the viscous model and will be discussed.

The early experiments of Benjamin & Ursell (Figure 3-1 (a)) utilized a deep layer of water as the operating fluid in a test cylinder of diameter 5.4 cm. Using the nodal indexing of this work, they investigated the $(1,2)_{sh}$ mode, appearing with a natural frequency at 15.82 Hz, in contrast to the inviscid natural frequency of 15.87 Hz. Respectable agreement with their inviscid model was found after shifting the natural frequency to the observed frequency, but the amplitudes are noticeably higher at the tongue minimum, a result of system dissipation. Upon fitting the data with the viscous model, it is seen that the stability tongue is modified only slightly, indicating that the viscous contribution of the interior is negligible. One therefore can only conclude that the hidden dissipation comes from either sidewall or from interfacial dissipative effects. A finding of the experiments of Chapter 4 was that theoretical agreement of the observed thresholds improved with the increase of the Bond number,

$$Bo = \frac{\Delta\rho g}{\gamma k^2}$$

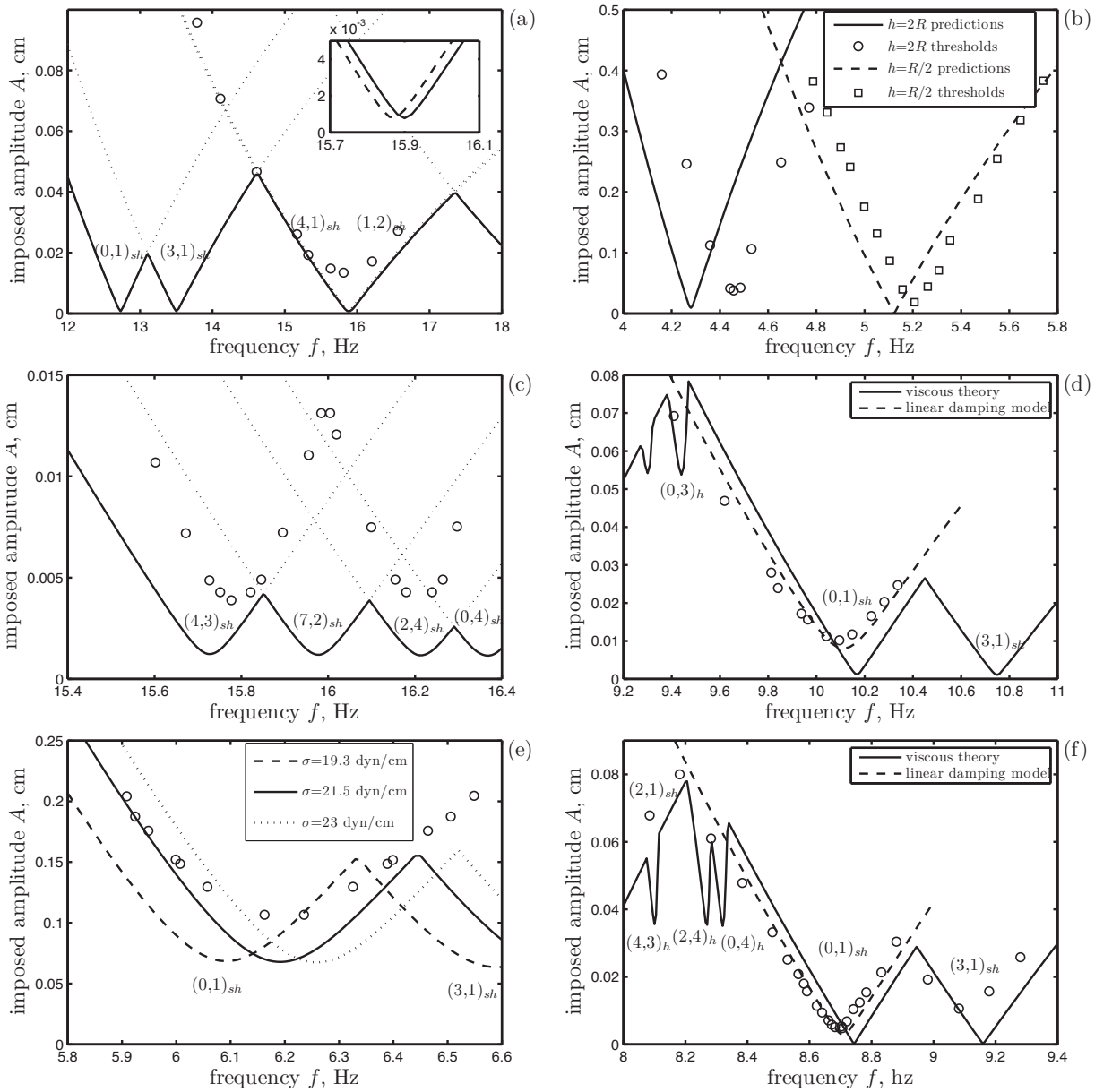

Figure 3-1. Past experimental thresholds in cylinders. System data are from (a) Benjamin & Ursell [11]: water and air, ρ=1000 kg m^{-3}, ν=1 cSt, γ=72.5 dyn cm^{-1}, R=2.70 cm, h=25.4 cm; (b) Dodge *et al.* [24]: water and air, R=14.5, h=29 and 7.25; (c) Ciliberto & Gollub [20]: water and air, R=6.35, h=1; (d) Henderson & Miles [36]: water/surfactant and air, γ=42.3, R=3.725, h=2.04; (e) Tipton & Mullin [77]: water and silicone oil, ρ_1=997.5 and ρ_2=766, ν_1=1.033 and ν_2=0.670, γ unreported and set to 23, R=1.76 cm, h_1=5.31 and h_2=0.739; (e) Das & Hopfinger [23]: FC72 and air, ρ=1690, ν=0.406, γ=11, R=5, h=6. All theoretical comparisons are made to the model of [52], assuming stress-free sidewalls and no interfacial dissipative effects. The dashed lines in Figures (d) and (f), however, are the linear damping predictions of the original works and are reproduced here for comparison to the case of stress-free sidewalls. All units are the same as listed for (a).

a measure of the relative importance of the sidewall capillary effects. For the experiments of Benjamin & Ursell, Bo=3.47. Careful inspection of all the predictions shows the $(4,1)_{sh}$ mode occupies nearly the same stability space as that of the $(1,2)_{sh}$, which is quickly understood by noting that the dimensionless wavenumbers $k_{41}R$ and $k_{12}R$ are identical to each other within 1% (see Figure 2-4). Therefore the selection of the $(1,2)_{sh}$ mode in the experiment is an important observation to make and we will present arguments later this is a result of sidewall effects. Also, the first two data points fall well inside the region of instability for the $(3,1)_{sh}$ and $(0,1)_{sh}$ modes, but these modes have apparently been damped entirely and instead the $(1,2)_{sh}$ mode remains.

Dodge *et al.* [24] ran experiments, also using water, in a cylinder with a rather large diameter of 14.5 centimeters, measuring critical thresholds and wave amplitudes. Figure 3-1 (b) shows their onset measurements for the $(1,1)_{sh}$ mode for two different layer heights, along with the predicted viscous thresholds. Their thresholds observed better agreement at the tongue minima than that of Benjamin & Ursell, likely due to the large tank dimensions and the relatively smaller sidewall contribution to the overall dissipation. A quantitative indicator is the Bond number of 839, which is the largest of all the previous experiments. However, acknowledged by Dodge *et al.*, of greatest surprise is the shifting of the experimental natural frequencies to higher frequencies, in contrast to the shift toward lower frequencies observed by Benjamin & Ursell. Notably the frequency bandwidths of 0.5 and 0.9 Hz were rather small, in part due to the large tank dimensions. A shift toward higher frequencies (and amplitudes) than predicted is also encountered with the thresholds of Ciliberto & Gollub [20] (Figure 3-1 (c), Bo=3.39), who explored chaos appearing near the co-dimension 2 point of a $(4,3)_{sh}$ and a $(7,2)_{sh}$ mode. Their frequency bandwidths of 0.4 Hz and 0.3 Hz were also notably small. Comparison of the predictions for the systems of Dodge *et al.* and Ciliberto & Gollub also illustrates how the viscous damping of the thresholds can differ for systems of the same working fluid when the heights and mode are different.

Of great significance are the experiments of Henderson & Miles [36], who made the first attempt of matching single-mode experiments to a theory incorporating viscous effects. Henderson & Miles performed experiments in a R=3.725 cm cylindrical cell with water as the operating fluid, using a surfactant to minimize the pinning of the interface to the sidewalls. Viscous damping was modeled using the theory of Miles [58], assuming that the effects were constrained to laminar boundary layers along the interface and the sidewalls. However, in the damping model, the water viscosity had to be taken to be 3 cSt to produce the experimentally observed damping rates in the cylinder. Nonetheless, incorporation of this damping rate into the model for the thresholds produced respectable agreement with the experiment for the $(0,1)_{sh}$ mode in the cylinder. The negative shift in the observed natural frequency was accounted for, as was the damping of the thresholds. The predictions of this linear damping model and their data are reproduced alongside the predictions of the viscous model in Figure 3-1 (d). In comparison, it is seen that the region of instability is only slightly damped for the viscous theory, much like the systems of Benjamin & Ursell and Dodge *et al.*, implying that again bulk viscous effects were not the primary source of damping in these experiments. The linear damping coefficient accounting for viscous effects in the bulk phases, given by Kumar & Tuckerman [52] and derived by Landau [54] upon ignoring interfacial effects is

$$\gamma_{visc} = 2k^2 \frac{\mu_1 \coth kh_1 + \mu_2 \coth kh_2}{\rho_1 \coth kh_1 + \rho_2 \coth kh_2}. \tag{3–1}$$

It follows that the linear contribution to the bulk viscous effect in these experiments was γ_{visc}=0.0216 s^{-1}, only about 5% of the measured damping rate of 0.44 s^{-1}, implying that the system's dissipation was dominated by the wall and interfacial dissipative effects. The frequency shift and slight deviation of the $(0,1)_{sh}$ thresholds in the work of Henderson & Miles (Bo=21.9) is also seen in the experiments of Das & Hopfinger [23], who also measured the threshold of the $(0,1)_{sh}$ mode, but in a large R=5 cm cell

(Bo=257). Figure 3-1 (f) reveals the deviation of the data from the viscous model to be qualitatively the same although arguably less than that of Henderson & Miles for both the $(0,1)_{sh}$ mode and its neighboring (3,1)h mode. Negative frequency shifts were observed along with threshold damping. The damping of the tuned $(3,1)_{sh}$ thresholds appears to be greater than the tuned thresholds of the $(0,1)_{sh}$ mode, a result consistent with the findings of our experiments.

Other experiments of note are those of Ito *et al.* [44] and Tipton & Mullin [77], because, like the experiments in this work, both were experiments run for liquid bilayers as opposed to a liquid with a passive air layer. The experiments of Ito *et al*. are qualitatively different from traditional single-mode experiments, as they were interested in modeling the effect of sidewall flow perturbations on the instability. In their experiment a column of water with kerosene lying on top of it was sinusoidally pumped using a piston, producing a moving interface like the Faraday problem, but base flow perturbations arose from shear flows at the sidewalls. They observed the growing cell modes at different frequencies much like the Faraday experiment, but in general the data does not agree with the viscous Faraday model and is not shown here. Of note, however, are the observations by Ito *et al*. of the development of a film produced by kerosene on the sidewalls. Qualitatively, this film was the same as observed in this work, and Ito *et al*. provide excellent discussion of its dynamics. Additionally, Ito & Kukita [43] further study the effect of the film on the nonlinear dynamics of the instability.

Tipton & Mullin probed the bifurcation structure of the $(0,1)_{sh}$ mode in a closed stainless steel cylinder containing water and silicone oil for a variety of interfacial heights, and observed a non-dimensionalized collapse to the predictions of a linearly damped Mathieu equation. They noted that their damping parameter was 8 times the value predicted by Equation 3–1, suggesting wall effects were important in their cell. The interfacial tension between their oil and water was also not measured, requiring guesses to be made to fit the viscous model to their data. Due to the small density

difference between water and oil, this system stands out for being the only set of previous experiments where the surface tension made a significant contribution to the mode dispersion. Taking the interfacial tension to be 21.5 dyn cm^{-1}, a match can be made between the observed and predicted natural frequencies, but is quickly lost when the value is adjusted slightly. At an interfacial tension of around 19 dyn cm^{-1} (a value suggested in private communication with Tipton & Mullin), the discrepancy is significant, cf. Figure 3-1. It appears the thresholds lay above the viscous prediction regardless of the exact value chosen, and the cell diameter of 35.22 mm, the smallest of the reviewed experiments, suggests that the dissipation due to wall effects was controlling. Additionally, the Bond number here of 2.4 was the lowest of all reviewed experiments.

Application of the viscous model to the past results clearly shows that there have been many experimental unknowns which are not accounted for in the linear stability model. Therefore results different forms of experimental mismatch, including mode shifts toward both higher and lower frequencies, increases in the threshold amplitudes and the complete absence of predicted modes. Broader interpretation of these systems cannot be given due to the limited scope of these studies, often times limited only to one or two modes. Thus in addition to a better replication of the assumptions of the linear theory, another important goal of this work is to study an entire range of modes, as presented in Figure 2-6, where the interaction between the sidewall and the instability can be more deeply understood.

CHAPTER 4
EXPERIMENTAL METHOD

While understanding the theoretical predictions is crucial to building an understanding of the instability, the main findings of this dissertation are, in fact, experimental. In this chapter, the different aspects of the experimental design of a system that attempts to replicate the model assumptions and produce repeatable and measurable phenomena will be discussed. The effect of temperature fluctuations, important to the replication of the main assumptions of incompressible Newtonian fluids with constant density and viscosity were considered throughout design of the cell and the experimental method. The most difficult assumption to replicate was the that of stress-free sidewalls, and the behavior of the interface near the sidewalls that it implies. The three-phase problem of the two liquids contacting a solid sidewall inevitably produces a static meniscus, which emits waves during vibration, and violates the assumptions of a no-flow base state and a flat interface. Fluid shearing at the sidewalls and capillary hysteresis are other examples of complex stresses which arise in real systems and must be considered. All of these phenomena hinder connection with the equations of motion and the experimental method must respect them. In addition to the choices made regarding the system fluids, dimensions, and cell design, the methods of measurement and analysis of the imposed vibrational waveform will be presented.

Choice of Liquids

One method to mitigate the non-ideality and approach ideal behavior is to select liquids forming an interface that “effortlessly” glides across the container wall when tilted, representing a minimization of the associated sidewall stresses. Quick and simple experiments with different single liquid layers and immiscible liquid bilayers revealed a wide variety of interfacial contact line behavior, strongly dependent upon the container material. It was beneficial to move away from single layers of water as a working system, considering it was shown that the sidewall stresses can control the overall system

dissipation (see Chapter 3), even when the capillary effects were lessened by addition of surfactant, as in the experiments of Henderson & Miles [36]. This work, although somewhat naively, shifted towards immiscible liquid bilayer systems, as the meniscus wave amplitudes appeared to decrease when compared to those observed with silicone oils in plexiglas containers, resulting from a large concave meniscus.

Early experiments were conducted using different sets of immiscible liquids in rectangular plexiglas cells. While immiscible silicone oil and water systems were natural candidates based on availability and the ability to tune the oil viscosity, water did not wet plexiglas and formed a gigantic bubble surrounded by wall-wetting silicone oil. Application of ScotchGuard^{TM} dirt repellant to the cell sidewalls attracted the water and created a horizontal interface, but the interface still suffered from a large, pinned meniscus which was resistant to motion. Notably, Tipton & Mullin [77] used silicone oil and water in a stainless steel cell, but the behavior of the contact line is unknown and non-ideal behavior is suggested by their damping rates and observed linear thresholds.

Octanol and water was an interesting and complex system considered, due to its ability to absorb isopropanol in both phases and thereby reduce its interfacial tension. By doing so, it was possible to virtually eliminate the sidewall meniscus and also produce free motion of the interface at the sidewalls. However, the solubility of IPA in both phases was difficult to control, and production of a system with a constant concentration of IPA in both phases was very difficult if not impossible. Excitation of the instability in a water-octanol-IPA system typically showed visual “streaming” of material near the deflecting interface, presumably due to the diffusion of IPA across the interface. Halting of the instability and allowing the system to settle subsequently resulted in stratified layers of different refractive index, also likely due to the graduation of IPA concentration. While extensive linear threshold data was not taken for water-octanol-IPA systems, there exist many interesting phenomena which could be studied in a controlled experiment and ought to be a subject of future investigation.

FC70, a dense and inert fluorinated hydrocarbon, and 1.5 centiStoke silicone oil were found to produce an interface with only a slight (∼1 mm) meniscus. Tilting of the experimental cell resulted in a smooth and very quick return of the interface to a flat position, indicating low sidewall stresses. It was believed the low surface tension (reported less than 7 dyn cm^{-1}[75]) was instrumental in minimizing the sidewall stresses. Close observation of the sidewall in a tilted cell showed that a tiny film of the silicone oil had formed, over which the FC70 glided, meaning the interface remained pinned to the sidewall well below where the apparent contact line had risen to. Low interfacial tension clearly aids the process where, to form a film, the interface must bend abruptly from its contact position, and then be stretched along the length of the oil-coated glass. The film thickness was found to decrease with the oil viscosity, and was therefore minimized by using 1.5 cSt oil. Silicone oil with 0.65 cSt viscosity was not used since it showed slight miscibility with FC70.

Liquid densities were measured using a pycnometer with calibrated volume of 51.490 mL. The density of FC70, listed as 1940 kg m^{-3}, was found to vary from bottle to bottle and therefore the measured densities are noted with the figures. Silicone oils of 10 cSt (ρ=940 dyn cm^{-1}) and 1.5 cSt (ρ=846 dyn cm^{-1}) were used. The density difference between the two phases plays a great role in the positioning of the frequency bands and thresholds in the discretized regime, considering the excited modes are primarily gravity waves with little capillary contribution. A system with a large density difference results in a larger frequency range for which mode discretization is important due to the selection of lower wavenumbers. At low frequencies the instability threshold is also lowered for large density differences, meaning harmonic and superharmonic modes are more easily accessed. The density difference in these experiments of nearly 1000 kg m^{-3} is quite similar to a water and air system, but the threshold behavior changes due to the increased viscous damping of high wavenumber harmonic and superharmonic tongues.

It was found that the assumed values of the viscosity and the interfacial tension were satisfactory for making experimentally-verifiable predictions with the linear model, and therefore neither was measured. The FC70 viscosity controls the damping of the threshold tongues in these experiments, and reasonable adjustment of the value reported by the manufacturer has very little effect on the predicted threshold curves. Additionally, interfacial tension shows virtually no effect on the theoretical predictions, as the large density difference between FC70 and silicone oils dominates the capillary contribution for the modes excited by the considered frequencies. Future, predictions made models of greater complexity would likely benefit from more accurate knowledge of the physical properties.

Cell Design

Rectangular cells were used initially, but later were substituted for cylindrical cells, as it was suspected the corners produced an adverse effect on the sidewall stresses. This was essentially reported by Henderson & Miles [36], who also conducted experiments with a square cross-section and observed greater deviation from predicted thresholds for squares than cylinders.

While increase of the lateral dimensions is appealing due to the dwarfing of the sidewall contribution by the bulk damping effects, a detrimental effect is the narrowing of mode frequency bands, for which tighter experimental control of imposed frequency and amplitude would be required. Although not pursued in these experiments, testing of multiple cell radii would offer the opportunity to minimize the sidewall damping with respect to the experimental control. The cylindrical height of the cell was not deemed crucial to designing a linearly ideal system, but the saturation of the $\tanh kH$ expression from the inviscid theory (see Appendix A) was helpful to determine at which layer heights a wavenumber k does not “see” the top or bottom.

Schematic diagrams of both the final cell design and the electromechanical shaker are presented in Figure 4-1. A modular approach was taken towards the cell design

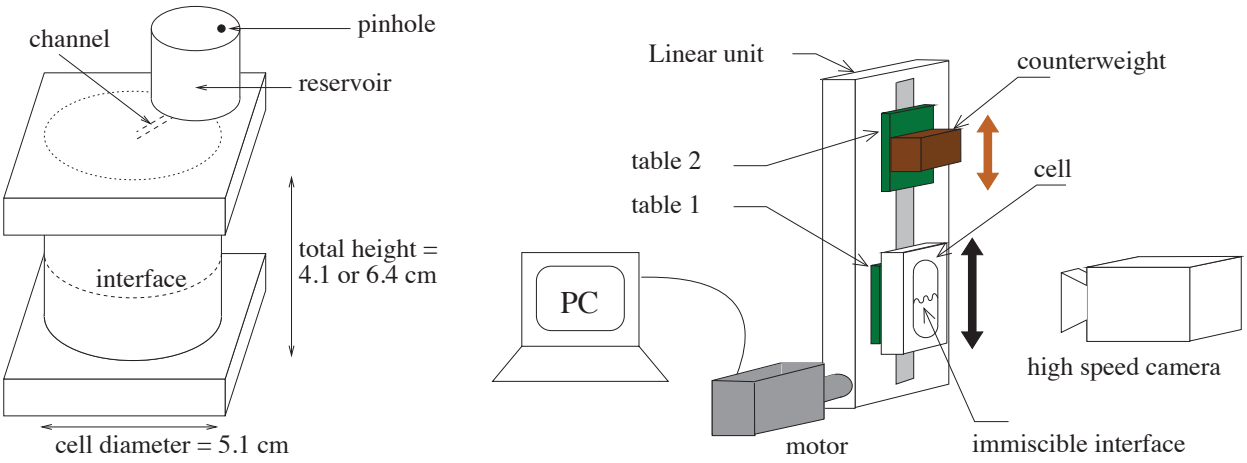

Figure 4-1. Schematic diagram of the cell and the electromechanical shaker. For further information see Zoueshtiagh *et al.* [83].

in order simplify cleaning and account for test cylinders of different height. With the availability of 5.1 cm ID glass tubes (of small wall thickness to reduce the optical effects due to glass curvature), two cylindrical test cells of approximately 6 cm and 4 cm total height were cut. The cells were built by closing the glass tube ends with square acrylic plates, into which circular trenches were cut and o-rings were placed. A compression seal was formed tightening of wing nuts on four bolts positioned near each plate corner. Finally, four thin acrylic plates and water resistant puddy were used to build a square cage around the cylinder. The cage was filled with water, which dramatically reduced the optical distortion that arises from curved geometries.

The influence of temperature fluctuations pervaded throughout all experiments, and is believed to have a significant impact on developing a repeatable non-linear experiment. An early problem encountered was being able to maintain a fully-filled, non-leaking cell due to the constant expansion and contraction of the working fluids in ambient conditions. This issue was exacerbated by the use of a halogen lamp which generated large amounts of heat. Use of the lamp was therefore limited, but it remained normal to perform experiments for an extended period of time, all during which the fluids were periodically heated and leaked due to the slight expansion of the liquids. During a

break, the liquids would again contract, typically introducing air bubbles to the cell. To manage these density fluctuations, the cell was designed with a small channel in the top plate connecting the main test cylinder to a smaller stainless steel reservoir. The reservoir was closed by a screw-cap with a tiny pinhole that allowed airflow. Filling of the entire system to a finite level in the reservoir allowed the main test cylinder to be completely filled indefinitely without need for refilling.

To minimize contamination during assembly of the cell, all pieces were rinsed with isopropanol, followed by water, and then dried with anti-static cloths and compressed air. Nevertheless small amounts of dust typically appeared in the test cylinder. Once the cell was completely assembled, test liquids were injected through the expansion reservoir into the main test cylinder using syringes and needles. To improve the contrast and visualization of the interfacial modes, a finely spaced grid was printed and affixed to the back pane of the water cage.

Electromechanical Shaker, Image Capture and Processing

Experiments were performed by mounting the cell to an electromechanical shaker (Figure 4-1) capable of moving the platform to programmed displacements at accelerations of up to $3g$. The cell was shaken using both single and double-frequency sinusoidal motions. All cell and interfacial motion were examined using time-space data of the images, obtained from high speed digital imaging with frame rates of up to 2000 fps. The shaker output frequency was taken as the actual experimental frequency, as the number of images in a cell period always corresponded to within one or two images based on a calculation using the programmed value, suggesting percent errors of less than 0.5%.

The imposed experimental amplitude, on the other hand, was quickly observed to deviate from the programmed amplitude, especially for amplitudes less than 3 mm. For this reason the real output amplitudes of the cell motion were determined by image analysis with ImageJ and MATLAB®. Nearly all of the rest of this chapter will be devoted

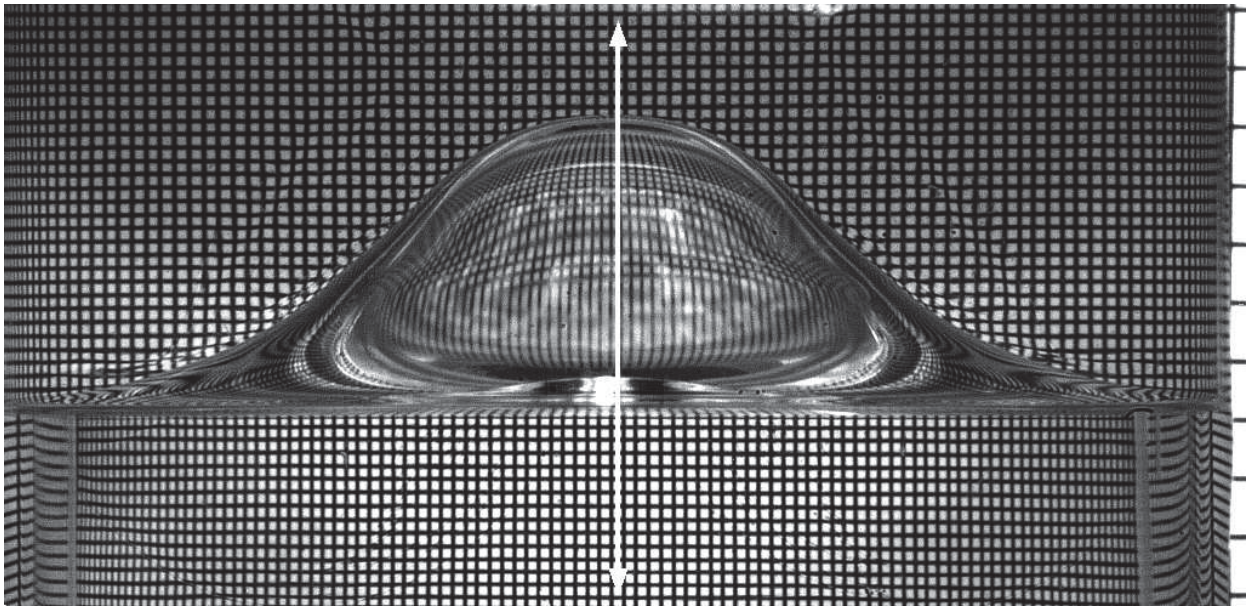

Figure 4-2. Sample camera image depicting excitation of a (0,1) mode. The white line depicts the single-pixel wide strip of data used in figure 4-3 and the graduations on the far right is a strip of paper on the front of the cell used to record cell motion. Cell radius is 2.55 cm.

to the determination of the output shaker single and double-frequency amplitudes, and analysis of the waveform quality. To begin to illustrate the means used to determine these amplitudes, pictured in Figure 4-2 is a sample cell image. The mode being excited is a $(0,1)_{sh}$ mode, behind which lies the backdrop grid. The disparity in the grid spacing between the upper and lower phase is due to different refractive indices, and careful observation shows distortion of the grid, owing to both residual curvature distortion and slight temperature and density gradients.

The actual cell amplitude of the experiment in Figure 4-2 was calculated by measurement of the displacement of the cell over the course of several oscillations. Taking a single-pixel wide slice of the image in Figure 4-2 (denoted by the white arrow), and stacking it next to the same set of data from each sequential image produces a set of time-space data, as in Figure 4-3. The white arrow in Figure 4-3 indicates the line of data taken from 4-2 where the wave deflection is at a maximum. The key information in the time space data is the sinusoidal motion of the backgrid, representing the output cell

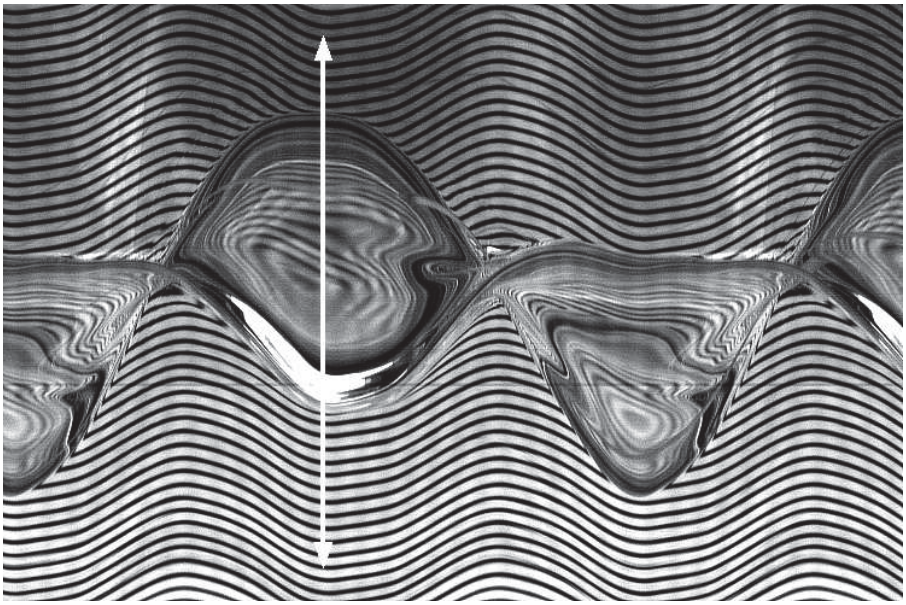

Figure 4-3. Time-space representation of the excitation of a saturated $(0,1)_{sh}$ mode. Vertical length scale of the image is the same as Figure 4-2, and the horizontal length of the image depicts a total time of 0.374 seconds. The white arrow depicts the data taken from Figure 4-2.

motion. The interfacial deflection amplitude of the (0,1) mode, subject to slight optical distortions, can also be extracted from Figure 4-3. This method however becomes more difficult for modes other than the $(0,1)_{sh}$ mode due to azimuthal non-uniformities. Due to the non-uniform bending of light through the cell and then to the camera objective, the back grid was actually not used draw the cell motion time space, but rather a notched slip of paper affixed to the front of the cell, as seen in the far right of the image in Figure 4-2.

Collecting time space data in this manner, careful control of the image by lighting and camera positioning allowed for quick and efficient transfer of the cell motion from the experiment, to the camera software, to ImageJ and finally to MATLAB®. Large amplitude tests required the camera to be positioned further away from the experiment to capture the entire cell motion. Frame rates of 1000 fps were deemed suitable, and captured image size was often set to a 128 pixel width sliver in order to minimize the amount of space consumed on hard drives and time spent for transfers. Typically a slip

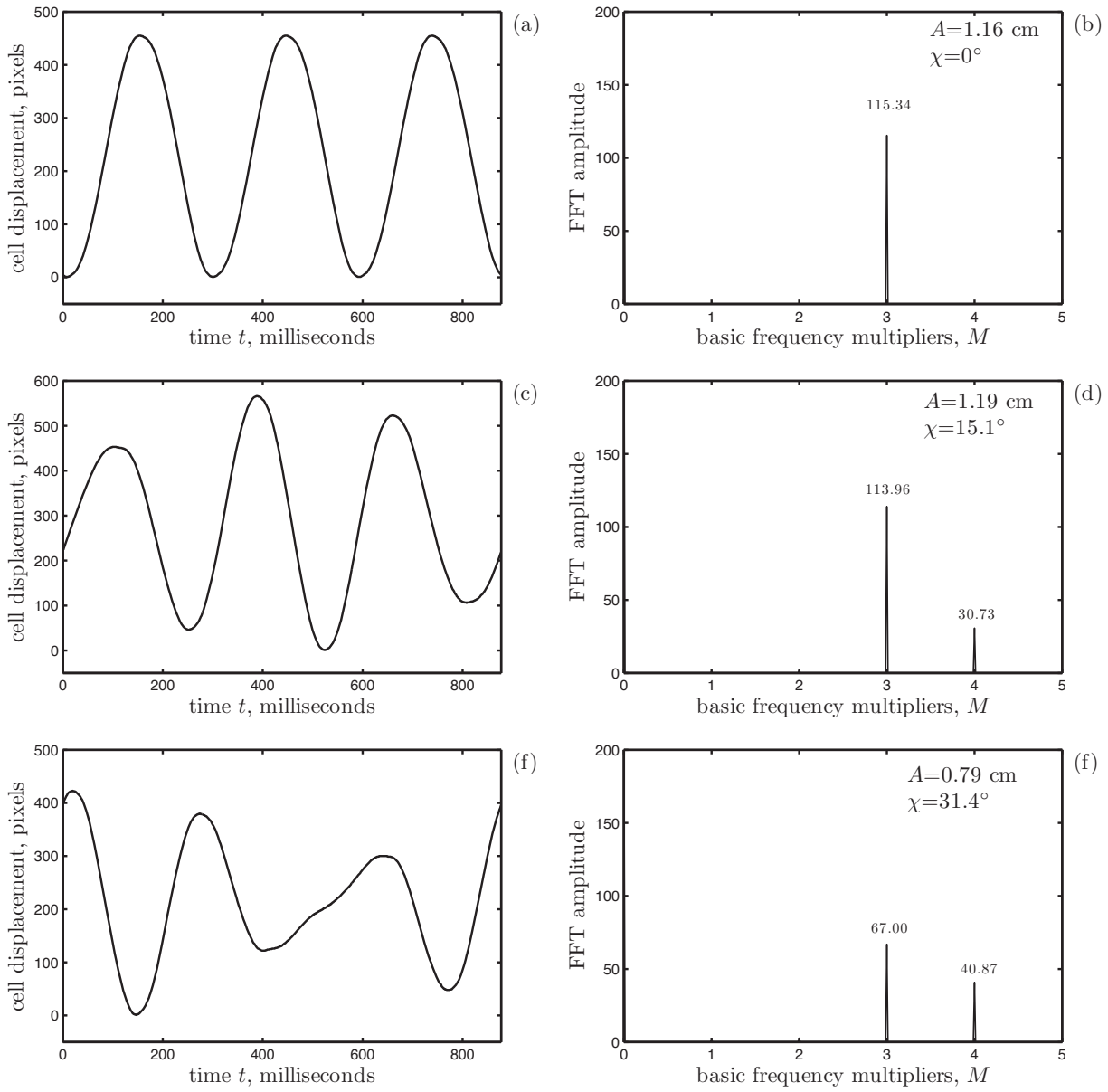

Figure 4-4. Experimental cell motion signals and FFT analysis. The signals (a), (c) and (e) and corresponding FFT spectra (b), (d) and (e) were obtained for programmed conditions of f =1.14 Hz with (a)χ=0°, A=1.20 cm, (c)χ=15°, A=1.23 cm, and (f)χ=31°, A=0.83 cm.

of paper like on the far right of Figure 4-2 with only one notch was used to create a set of images that produced a time space which could quickly be converted to a single-pixel width line of binary data via ImageJ's "Threshold" and "Skeletonize" commands.

Single and Double-Frequency Amplitude Determination

The output amplitude for single-frequency experiments could be obtained simply using the time space data obtained in ImageJ, without any further processing. The single-frequency cell amplitude, in pixels, corresponds to half the peak to trough distance of one cell oscillation, and conversion to a real distance then only requires a distance of known length on the image. The output amplitude for the signal presented in figure 4-4 (a), obtained by this method was 1.16 cm, less than the programmed amplitude of 1.2 cm. A major obstacle that had to be respected was that the percent error between the output and the programmed amplitude was a complicated function of both the programmed amplitude and frequency, and it was therefore necessary to analyze the output cell motion for every data point.

The output signals presented in Figure 4-4 (a), (c), and (e) result from a programmed motion of Equation 2–26 where (M_1,M_2)=(3,4) and $f=\omega/2\pi$=1.14 Hz. While crest-to-trough analysis works for the single-frequency motions, it is apparent this method will not work for the double-frequency signals of Figures 4-4 (c) and (e). Thus MATLAB®'s discrete Fast Fourier Transform function was used to analyze double-frequency signals. Taking the discrete Fourier transform of a digital signal decomposes the real data into the complex amplitudes of the various frequency components present in the signal. To combat digital noise and the low resolution that arises in short signals, FFT was performed on a signal built by stacking the same period of cell motion data onto itself many times. Analysis of the long-time cell motion showed signal deterioration, but at times well past the duration of experiments in this work. In analyzing single periods of cell motion, the two amplitudes for (3,4) forcing appeared exactly at basic frequency multiples of 3 and 4, as seen in Figures 4-4 (b), (d), and (e), further supporting the frequency control of the shaker.

Analysis of several sets of cell motion with χ=0° and comparison to the peak-to-trough method at different frequencies and amplitudes showed the FFT peak amplitudes to

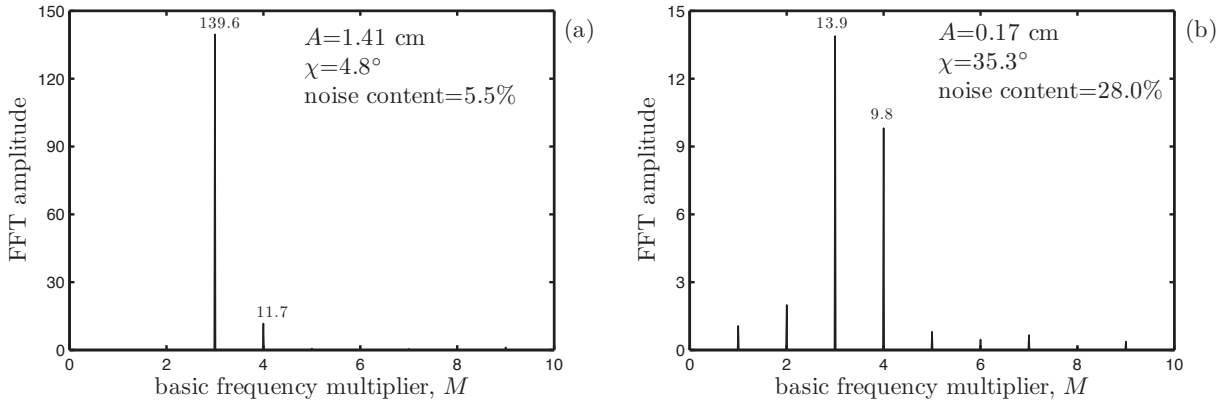

Figure 4-5. Sample Fourier spectra depicting the appearance of undesired frequencies. Programmed parameters were (a) f=1.12 Hz, χ=5°, A=1.45 cm and (b) 1.29 Hz, 35°, 0.25 cm.

scale linearly with output cell motion amplitude and also to be independent of frequency. Thus the peak-to-trough method was used to calibrate the FFT peak amplitudes for a single-frequency experiment, and after doing so it was possible to calculate the output amplitudes A_{M_1} and A_{M_2} for the M_1 and M_2 components in double-frequency experiments.

An important implication of the varying percent error of output to programmed amplitude meant that for double-frequency experiments the output value of χ suffered from the same lack of correspondence to the programmed value. For example, when a programmed value of χ specifies separate component amplitudes of, say, 10 and 5 mm, but the output amplitudes disproportionately are adjusted to 8 and 3 mm, the output value of χ changes. However, given the real output amplitudes of the frequency components by the FFT analysis, the real value of χ was determined by taking $\tan^{-1}(A_{M_2}/A_{M_1})$ via the definition 2–26. Finally, given the real values of χ and A_{M_1} and A_{M_2}, the overall amplitude A could be determined by either $A_{M_1}/\cos\chi$ or $A_{M_2}/\sin\chi$.

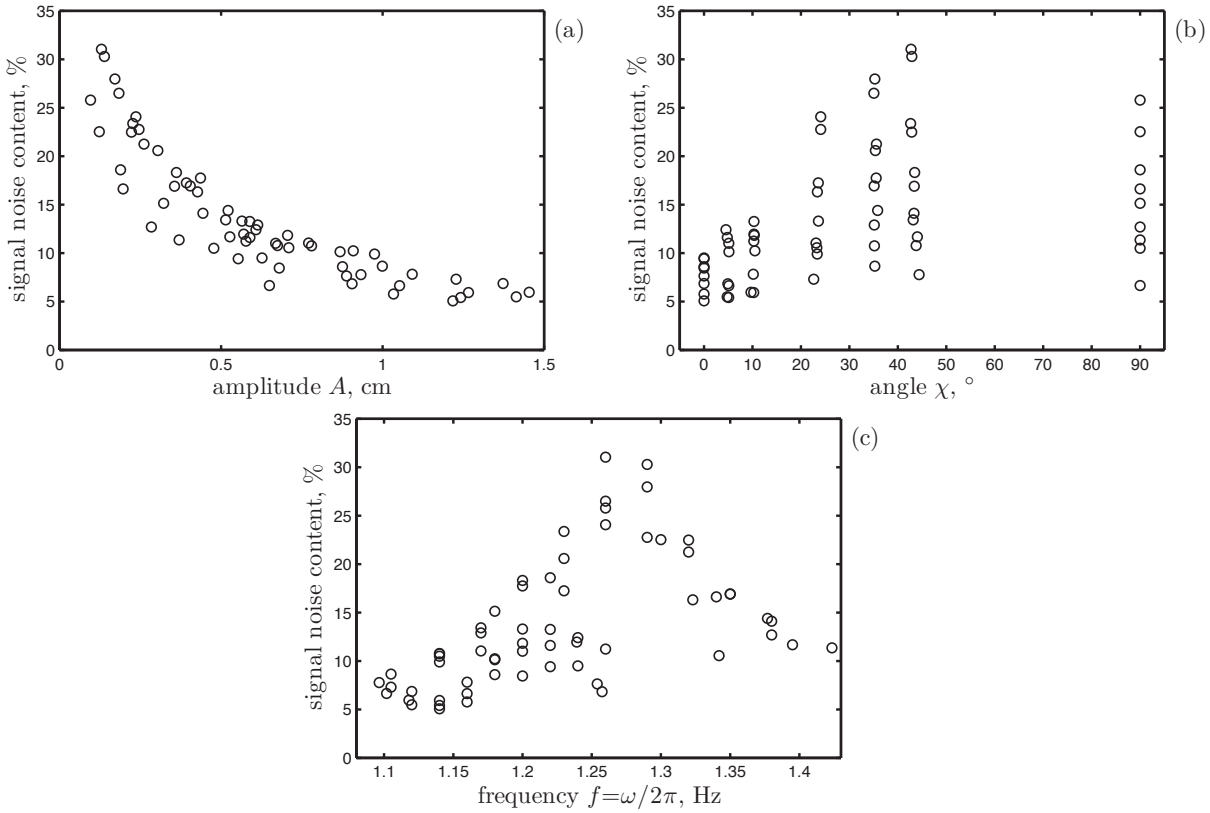

Figure 4-6. Output cell motion signal quality dependence on parametric conditions. Percent quantities plotted are the ratios of the undesired FFT noise to the amplitudes of the programmed frequencies.

Analysis of the Output Cell Motion Quality

Fourier analysis presented a powerful technique to analyze the quality of the imposed shaker waveform. In addition to the programmed frequencies, it was possible detect the presence of other harmonics in the cell motion, owing to either motor and structural vibrations or digital processing noise. The presence and effect of these harmonics are highlighted by the two Fourier spectra in 4-5, corresponding to experiments with different amounts of noise relative to the principle frequency components. Figure 4-5 (a) presents the spectrum for a high-amplitude experiment with only the slight addition of the 4ω component (low-χ). Here the principle 3ω and 4ω peak amplitudes dominate any other noise or system resonances, whose total summed amplitude accounts for 5.5% of the programmed frequency amplitudes.

Figure 4-5 (b) corresponds to motion with far greater ratio of 4ω component (χ=35.3°), at a considerably lower amplitude. Here the amplitudes owing to undesired system resonances and noise summed to nearly 30% of the combined 3ω and 4ω amplitude, raising greater call for concern.

This non-ideality showed trends with respect to the parameters A, χ, and f which could be generalized. Presented in Figure 4-6 is this relative percent of undesired frequencies for all double-frequency data presented in this work. Lower amplitudes, higher frequencies, and departure from the single-frequency values of χ=0 or 90° all tend to introduce a greater proportion of these additional resonances. This trend depends most consistently on the imposed amplitude, because experiments at high frequency or frequency mixing can still produce good signals if the overall amplitude is high. While this behavior calls into question the waveform integrity for low output amplitudes, it is believed the amplitudes of the undesired frequencies such as those in Figure 4-5 (b) are still too small to affect the linear threshold observed by the principle 3ω and 4ω frequencies. Once again this may be an avenue for improvement necessary to perform a non-linear experiment.

Figure 4-6 (b) illustrates another concern, where the data points show slight deviations from the programmed integer values of χ=[5, 10, 22.5, 35, 45]. Again, this arises due to the inability to control the deviation of both output frequency amplitudes simultaneously. It would be possible to make slight adjustments to the programmed χ until the desired output was reached, but in the midst of searching for a linear threshold this would be tedious. Fortunately, the typical deviation observed between output and the programmed value of χ was never considered significant enough to affect linear stability predictions or the conclusions drawn from the experiments.

Experimental Repeatability

The most commonly performed experiment was the search for a linear threshold amplitude, done by successive experiments at constant frequency, while interpolating

between amplitudes which did and did not see the instability. This method requires a tolerance for the instability, where, if the amplitude is lowered by a tolerable amount and the instability is not seen, then the original point is marked as the threshold. The normal tolerance in these experiments was about 0.1 mm. A troubling behavior that was encountered was the increase in the marked threshold from one day until the next morning, where, for example, if at the end of one day the instability at a certain frequency was first found to grow at an amplitude of 10 mm, it was common to not observe the instability until, say, 12 mm amplitude the next morning.

The reason for the increase in amplitude stems from from the wetting behavior of the FC70-silicone oil film and the stick-slip behavior of the contact line. It was found that the excitation of the instability developed a silicone oil film below the resting interface position, and the general sense is that the presence of this film greatly reduced the stresses relating to motion of the apparent contact line. The film is visible to the naked eye and gradually recedes after the cell vibration is stopped and the instability dies out. “Sidewall wetting” on the other hand was believed to be a molecular level phenomenon, inferred because excitation of a long-stagnant interface and re-forming of the sidewall film did not instantly re-adjust the threshold to the value of the previous day. Instead, many experiments forming the film had to be carried out, throughout which the instability could be excited at lower and lower amplitudes for a specific frequency.

This process of “wetting” the sidewall to its saturated state could take nearly two hours, and therefore a data set of thresholds was best determined by ensuring the instability was continually being excited and the wall wetting conditions were kept constant. Maintenance of the wetting was, however, complicated by the existence of mode induction times: apparent dead periods before which the instability appeared and grew. These times increased with proximity to the threshold, approaching five minutes, meaning the maintenance of constant wetting conditions became more difficult as one neared the actual threshold. One approach taken to getting data near the threshold

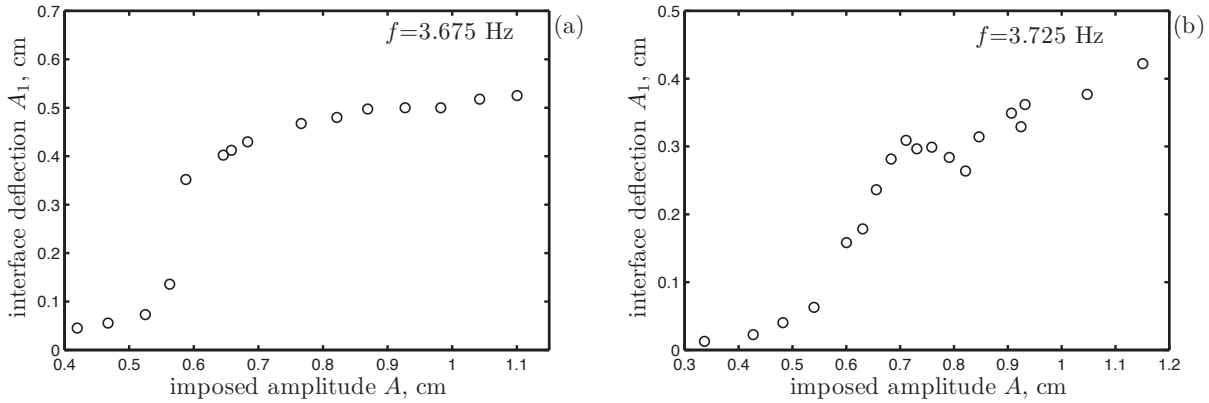

Figure 4-7. Experimental repeatability issues. Saturated wave amplitudes of $(0,1)_h$ modes for a series of experiments (a) without a coffee break and (b) with a coffee break.

was to use intermittent experiments well above the threshold where the mode could be quickly excited and the wall conditions restored.

While the discussed method for maintaining constant wetting is satisfactory for reproducing the reported thresholds of this work, this method would likely need to become more specific to ensure repeatability of nonlinear phenomena. This is illustrated somewhat comically in Figures 4-7 (a) and (b), two sets of experiments measuring the saturated wave amplitude as a function of the forcing amplitude, a traditional bifurcation curve. In order to preserve the sidewall wetting from experiment to experiment, measurements were made quickly and effort was made to be constantly exciting a mode. The great sensitivity of the nonlinear system to the sidewall wetting is seen in Figure 4-7 (b), where instead of running the set of experiments without pause, the cell sat still for a fifteen minute coffee break. Upon return, the change of the sidewall wetting was significant enough to produce data inconsistent with that from before the break, around A=0.8 cm. In addition to the saturated wave amplitudes, there exists an abundance of more complex nonlinear behavior which would also show great sensitivity to the initial condition.

CHAPTER 5
SINGLE-FREQUENCY EXPERIMENTS AND DISCUSSION

Sidewall Meniscus and Film Behavior

The key results are connected to the behavior of the interface close to the sidewalls, the source of the non-ideality. Filling of the cell with FC70 and silicone oil produced a convex down meniscus in the glass cylinders, a result of the preferential wetting of the glass by the silicone oil. Upon vibration of the cell either below or above the Faraday threshold, the harmonic modulation of the gravity field causes adjustment to the desired meniscus profile, resulting in harmonic emission of an axisymmetric wave from the sidewall. For a system that commences oscillation, there exists a transient period during which the emission of the meniscus wave and the reflection of the wave through the cylinder's z-axis equilibrates to a steady state wave that appears as concentric ripples. The quiescent state, initial emission of a wave, and a steady state meniscus profile are depicted in Figure 5-1. The magnitudes and characteristic wavelengths of these ripples are very much a function of the parametric amplitude and frequency. Finally, although the temporal behavior of the interior profile is complex due to the persistent emission and reflection of meniscus waves, the alteration of the meniscus remains axisymmetric and harmonically periodic with the cell motion. This periodicity is suspected to interact with the harmonic modes of instability, which will be presented and discussed further on.

Pictured in Figure 5-2 is the excitation of a $(0,1)_{sh}$ mode after it has saturated to a steady amplitude. While the nonlinear growth is not the main focus of this work, the transition to this state is essential to be able to reproduce the linear thresholds. The emission of meniscus waves does not alter the contact position of the interface at the sidewalls, but excitation of a Faraday wave results in a motion that begins to separate the apparent contact position from the actual position. As the Faraday wave begins to grow, the first downward motion of the interface at the sidewall causes both the apparent

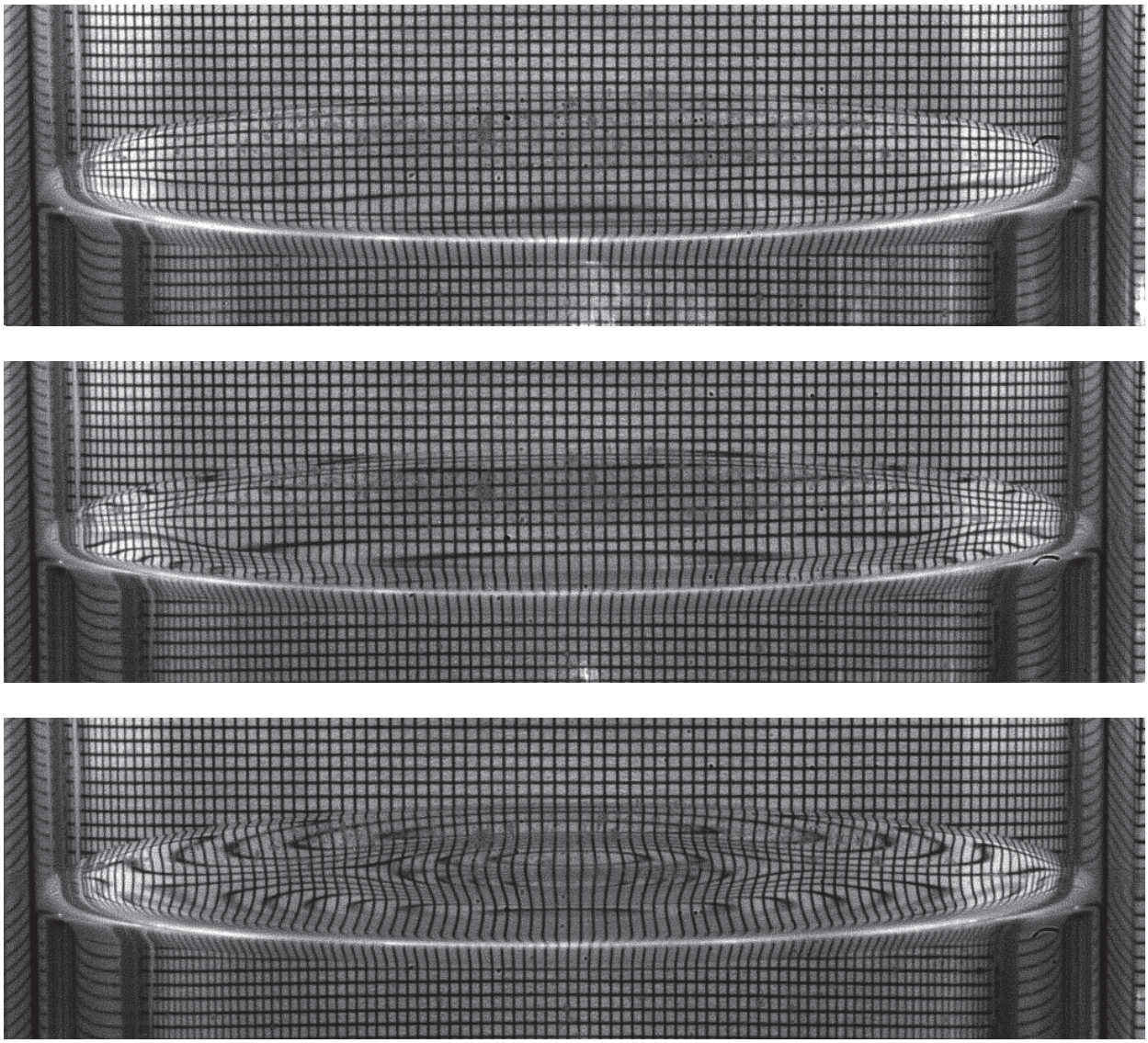

Figure 5-1. Experimental visualization of the meniscus dynamics. Images depict the static FC70 and 1.5 cSt silicone oil interface and meniscus (top), initial meniscus wave emission (middle) and steady state meniscus waves (bottom). The wave profile generated by the meniscus dynamics remains axisymmetric throughout the period of induction prior to growth of the instability.

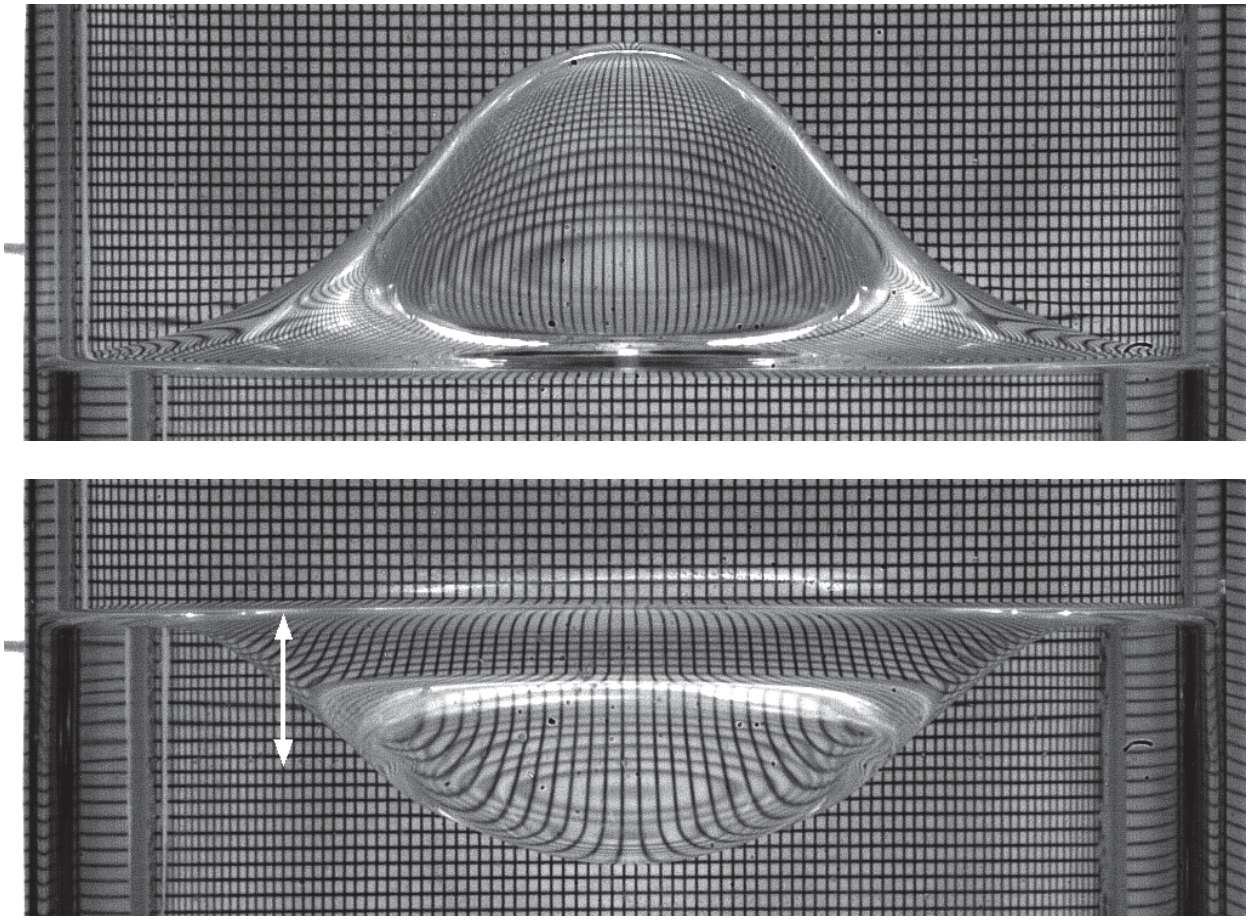

Figure 5-2. Experimental visualization of the excitation of a $(0,1)_{sh}$ mode. Excitation at f=7.5 Hz is shown for the maximum (above) and minimum cycle (below) in a FC70 and 1.5 cSt silicone oil system. The double-headed white arrow denotes the z-direction difference between the apparent and actual contact lines of the interface. Cell radius R=2.55 cm.

and the actual contact line to be pushed downward. For the reverse upward motion of the interface, the apparent contact line moves upward, while the actual contact line remains fixed to the lowest position the interface had reached, visualized in Figure 5-2. While the actual and apparent contact lines coincide for the upward cycle, the actual contact line lies 0.56 cm below the apparent contact line in the downward cycle, evidenced by the slight optical deformations of the back grid in the far left and right sides of the image. After saturation of the Faraday wave to a finite amplitude, the interface remains tethered to this low position, stretching and contracting vertically as the bulk

FC70 glides up and down over a tiny film of silicone oil. This is clearly visualized in Figures 5-3 and 5-4, with sets of images showing the film dynamics during a period of a saturated $(0,1)_{sh}$ mode, like Figure 5-2. A system with silicone oil viscosity 50 cSt is shown in Figure 5-3, and the film formation is evidenced by the deformation of the grid as the apparent contact line advances above the pinned position. Temporal asymmetry is seen when the apparent contact line begins to recede, and the profile of the interface more closely represents a 90° angle with the wall. Both the grid deformation (film thickness) and asymmetry are more subtle in Figure 5-4, where a set of images has been shown for a $(0,1)_{sh}$ mode when the upper viscosity is 1.5 cSt. The formation of this film is believed to be critical to the realization of the stress-free boundary condition. Obviously there are stresses introduced through this mechanism, but we shall argue that it is less significant than the viscous stresses arising from bulk fluid motion. The dependence on the upper phase viscosity will be established by first presenting the experimental thresholds for a $(2,1)_{sh}$ mode when 10 cSt oil is used as the upper phase, followed by the results using 1.5 cSt oil.

Experimental Threshold Dependence Upon the Upper Phase Viscosity

Figure 5-5 presents the experimental onsets of the $(2,1)_{sh}$ mode and the corresponding theoretical predictions for two FC70 and silicone oil systems of identical layer heights in which the upper phase viscosity is (a) 10 cSt and (b) 1.5 cSt. The data points correspond to sets of conditions at which the instability was observed. A separate experiment performed at an amplitude slightly lower than that of the data points resulted in a system at which the instability does not appear and only the meniscus waves were present. Hysteresis effects have been well reported (Benjamin & Ursell [11], Henderson & Miles [36], Tipton & Mullin [77], Das & Hopfinger [23]) on the detuned branch of the curve, where the “offset” of wave motion occurs at a frequency or amplitude lower than the onset, but this phenomenon was not studied in this work. The end points of the data set correspond to co-dimension 2 points, in this case for both sets of results the left

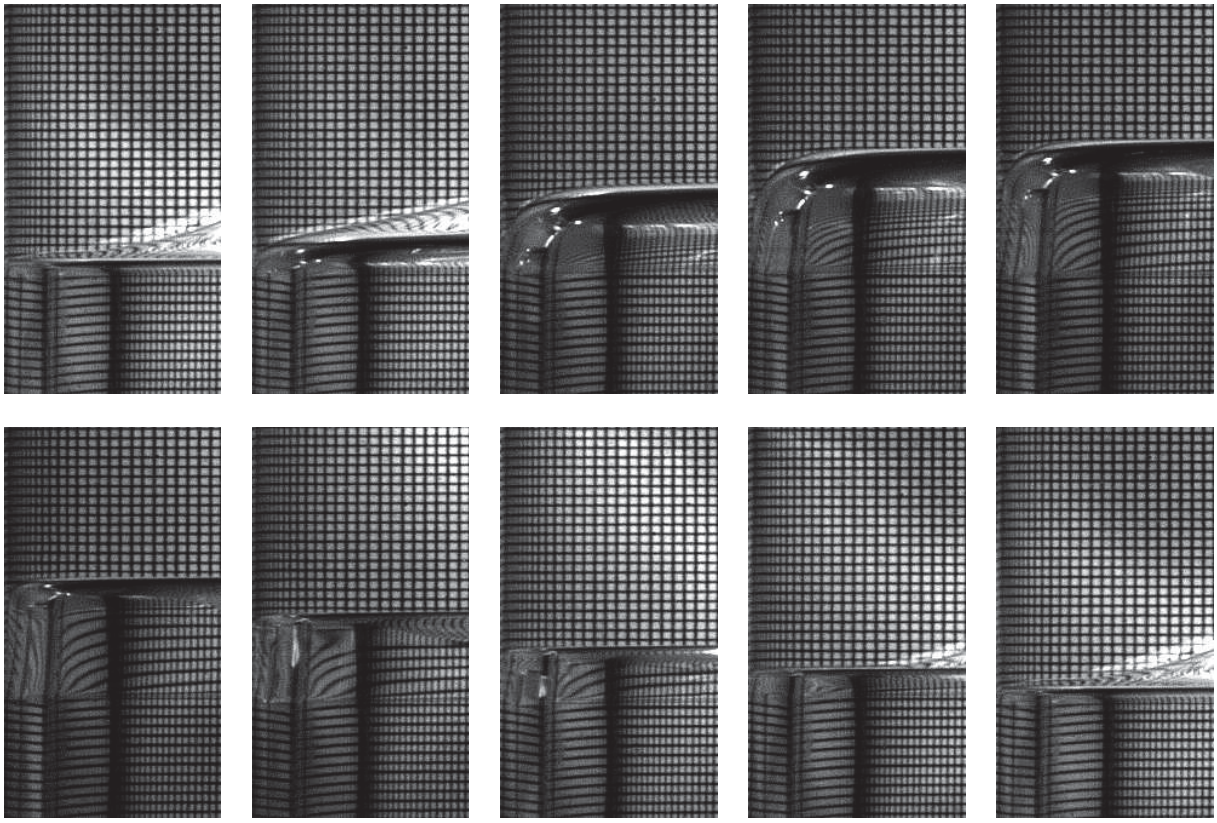

Figure 5-3. Film dynamics in a FC70 and 50 cSt silicone oil system. Images are taken of the sidewall during one period of the saturated excitation at f=6.7 Hz of a $(0,1)_{sh}$ mode. Moving from left to right and then top to bottom, the temporal spacing between each image is 0.299 seconds. Images are presented such that the interface contact line remains constant in each image.

co-dimension 2 point is a superposition of the $(2,1)_{sh}$ with a $(1,1)_{sh}$ mode, and a $(2,1)_{sh}$ with a $(0,1)_{sh}$ for the right point. The latter co-dimension 2 point in the 10 cSt system is visualized in Figure 5-6, exhibiting the same contact line behavior as in Figure 5-2. In the case of this instability it should be noted that the film is not azimuthally uniform due to the presence of the $(2,1)_{sh}$ mode.

Of great interest is the deviation between the thresholds and the predictions in both data sets; the observed 1.5 cSt thresholds clearly provide better agreement with the predictions compared to that of the 10 cSt oil. In fact the sidewall film was much smaller and difficult to notice in the 1.5 cSt oil systems, and therefore, in addition to lower stresses arising from sidewall boundary layers, we concluded that the total sidewall

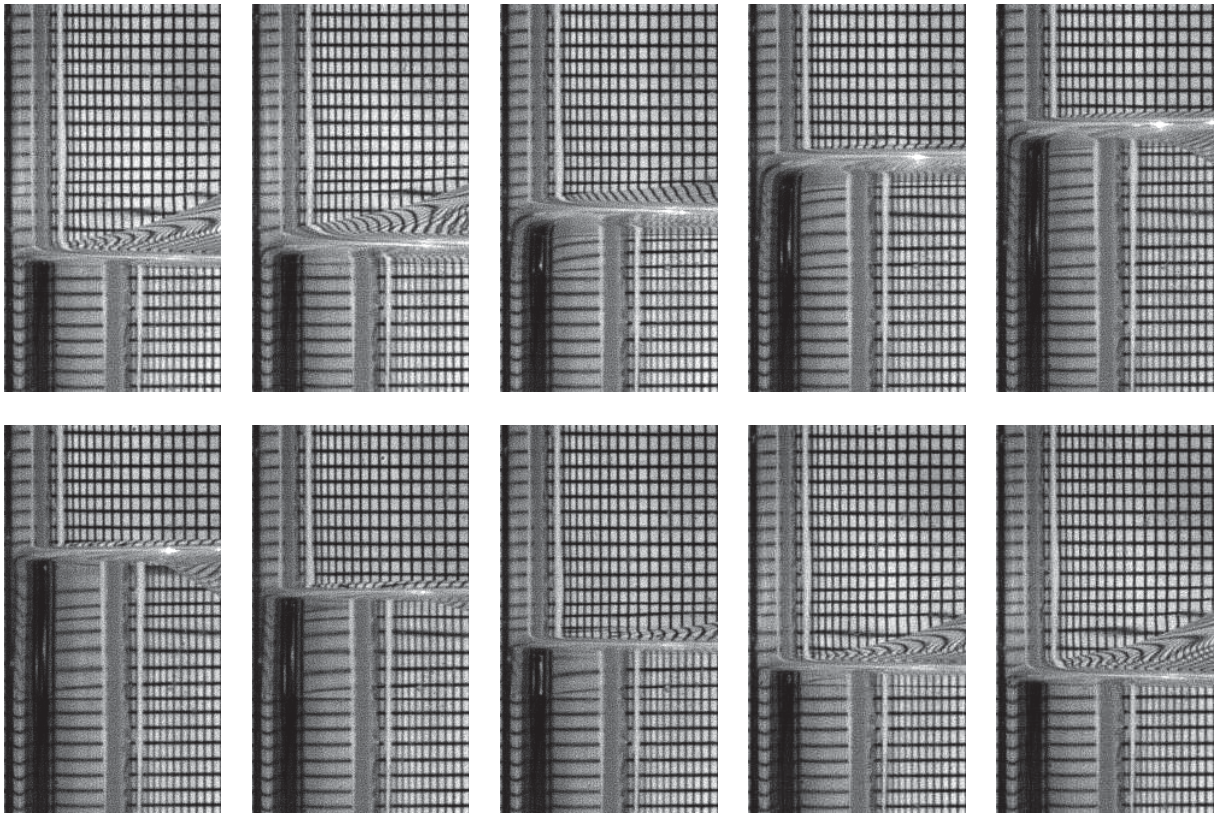

Figure 5-4. Film dynamics in a FC70 and 1.5 cSt silicone oil system. Images are taken of the sidewall during one period of the saturated excitation at f=7.5 Hz of a $(0,1)_{sh}$ mode. Moving from left to right and then top to bottom, the temporal spacing between each image is 0.267 seconds, and the image length scale is the same as 5-3. Images are presented such that the interface contact line remains constant in each image.

contribution to the overall system dissipation was much smaller when using 1.5 cSt oil. At the end of the section, this will be quantitatively verified by comparison of the predicted interior viscous contribution with the experimental damping rates. Thus in the interest of ideality the remainder of experiments to be presented use 1.5 cSt oil, which allows us to more carefully pinpoint the interaction between the non-ideality and the instability. Before presenting more threshold data, the nonlinear behavior of the wave growth will be discussed using Figures 5-5 (a) and (b) as it is characteristic of all the observed modal behavior and has a tendency to obscure the linear threshold.

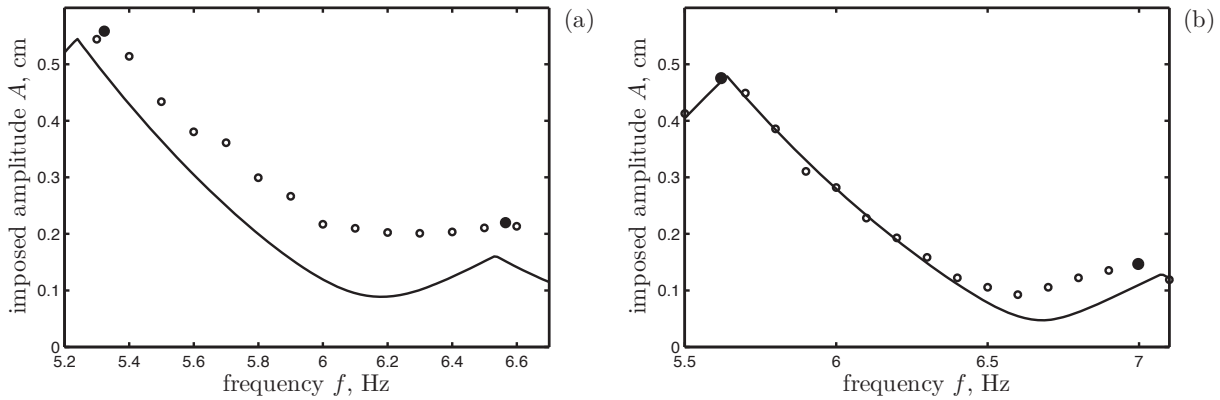

Figure 5-5. Dependence of the upper phase viscosity on theoretical agreement. Experimental thresholds and predictions are for excitation of the $(2,1)_{sh}$ mode in FC70 (1916 kg m^{-3}) and silicone oil bilayers (h_1=2.1 cm, h_2=2.0 cm) in a R=2.55 cm cylinder for (a) 10 cSt oil (944 kg m^{-3}) and (b) 1.5 cSt oil (846 kg m^{-3}). Open circles represent single-mode thresholds, black dots represent co-dimension 2 points. Neighboring modes are the $(1,1)_{sh}$ mode at lower frequencies and the $(0,1)_{sh}$ at higher.

Nonlinear Growth and Saturation

The nonlinear behavior changes considerably as one moves from the detuned branch of the $(2,1)_{sh}$ mode to the tuned branch in Figure 5-5. It has also been reported that the bifurcation is subcritical for frequencies below the natural frequency, i.e., detuned modes, and supercritical for frequencies above the natural frequency, i.e., tuned modes [25, 59]. In this work, the experimental observations are consistent with this, given that there exists a “jump” in the saturated amplitude of the excited mode for the data points at frequencies less than the natural frequency, while at frequencies above the natural frequency the mode saturation is nearly zero at the critical threshold. In fact, for many of the points below the natural frequency, the excited mode grows until the interface ruptures for imposed amplitudes slightly above the threshold. Because such a marked change can be observed by such slight changes in the imposed amplitude, detection of the instability is quite easy for the subcritical branch. The instability is more difficult to detect on the supercritical branch, because a slight increase in the imposed amplitudes past the threshold results in only a slight increase in the saturated wave

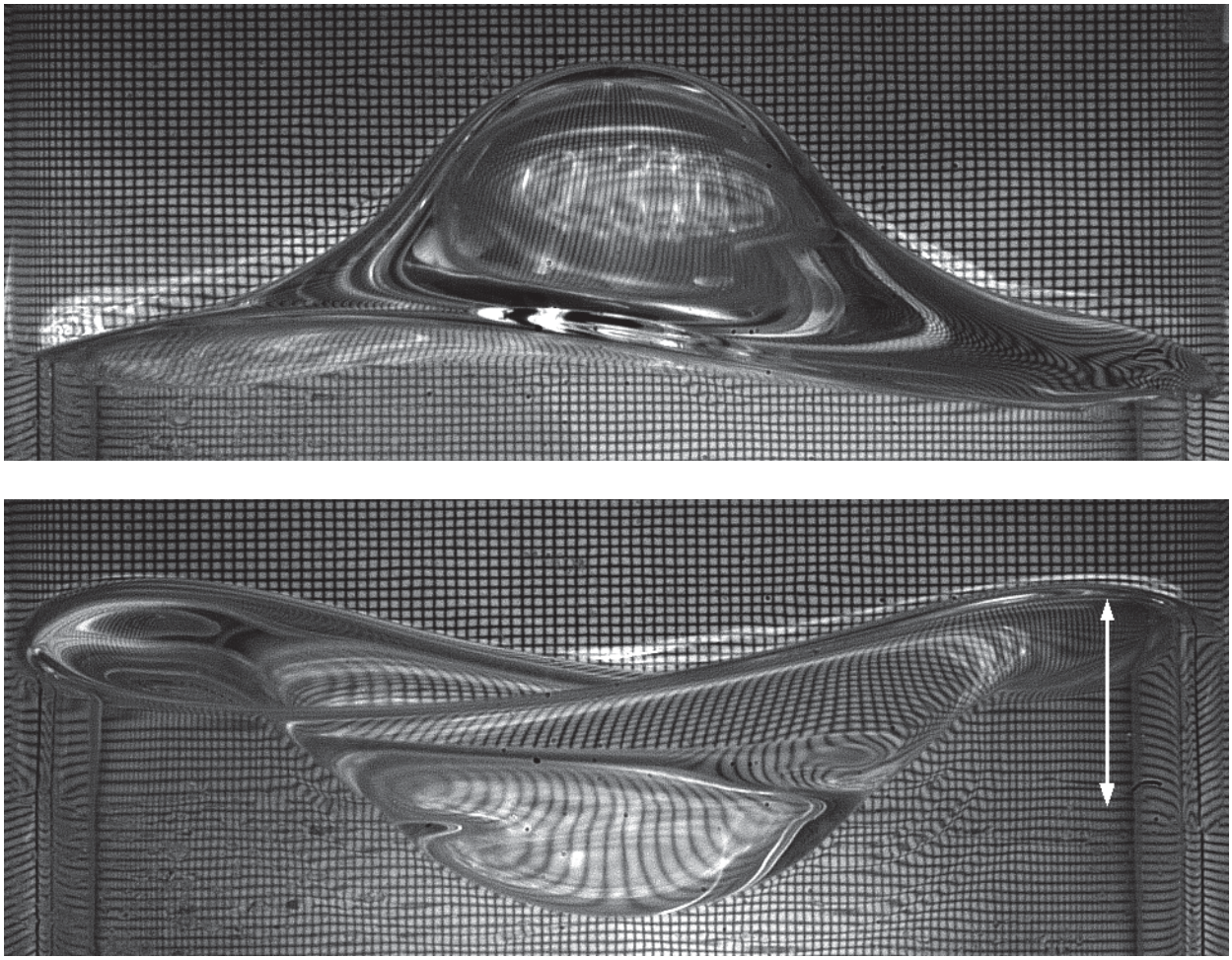

Figure 5-6. Experimental visualization of a co-dimension 2 point. Presented is the (a) maximum cycle and (b) minimum cycle during the growth of a co-dimension 2 point consisting of a $(2,1)_{sh}$ mode with a $(0,1)_{sh}$ mode from the data set in Figure 5-5 (a).

amplitude. This difficulty is compounded for tuned harmonic modes, as it becomes more difficult to differentiate the instability from the meniscus waves, whose emission is also harmonic.

Finally, the temporal dynamics of the growth of detuned modes is very interesting. In the excitation of detuned modes, there were periods of time during which the interface showed no unstable motion long after initialization of the cell motion. Only the meniscus waves persisted during these induction periods, and suddenly the interface would begin to deflect and grow in a rapid manner. These induction times increase with proximity to

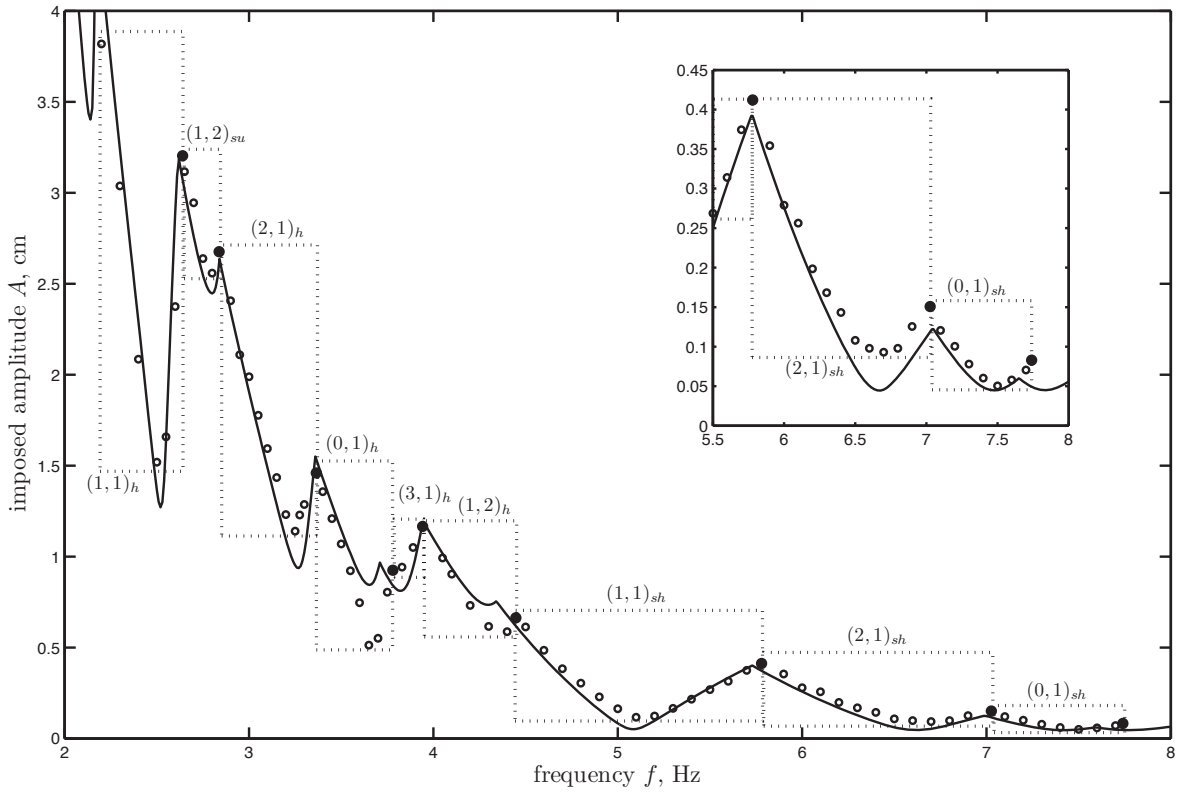

Figure 5-7. Theoretical comparison for the large height experimental system. Experimental thresholds and the corresponding theoretical curve is shown for a bilayer of FC70 (h_1=3.1 cm, ρ_1=1888 kg m^{-3}) and 1.5 cSt silicone oil (h_2=3.3 cm, ρ_2=846 kg m^{-3}) in the R=2.55 cm cell. Data points enclosed by a box indicate the excited mode. Black dots represent co-dimension 2 points.

the critical threshold, sometimes approaching four or five minutes, as noted by Das & Hopfinger [23].

FC70 and 1.5 cSt Silicone Oil Instability Thresholds

Presented in Figures 5-7 and 5-8 are the sets of threshold data for cells filled with large and small heights of FC70 and 1.5 cSt silicone oil. Frequency bands and threshold amplitudes were found for modes ranging from 2 to about 8 Hz. Above 8 Hz the wavefield was excited at considerably smaller amplitudes, and the system behaved more like a laterally infinite system as the effects of mode discretization began to vanish. In both systems, superharmonic and harmonic modes were observed in addition to the traditional subharmonic response. Co-dimension 2 points, predicted theoretically by the

model as the cusps in the stability curve, were found throughout the frequency range by careful actuation of both frequency and amplitude. The experimental thresholds for both layer heights are predicted quite well by the model, especially from the perspective of mode selection. For only a handful of points is the observed mode different from the theoretical prediction. However there are certainly some noticeable trends of the data not matching the predictions, and for this reason the results of each cylinder will be discussed separately.

The experimental data are grouped together according to mode. The system presented in Figure 5-7 is the large height system with a FC70 layer of 3.1 cm and a 1.5 cSt silicone oil layer of 3.3 cm. The modes observed in this system, in increasing frequency, are $(1,1)_h$, $(1,2)_{su}$, $(2,1)_h$, $(0,1)_h$, $(3,1)_h$, $(1,2)_h$, $(1,1)_{sh}$, $(2,1)_{sh}$, and $(0,1)_{sh}$. The observed modes, noted by the enclosing boxes in the figure, match the predicted mode except when noted. The threshold amplitudes show good agreement, save for the points near the tongue minima for the subharmonic and superharmonic modes, due to residual wall dissipation. On the other hand, for the $(0,1)_h$ and $(1,2)_h$ tongues, it can be clearly seen that the thresholds of the experiment lie below the predicted thresholds. This is a noteworthy result, and the best explanation seems to be the interaction of the harmonic, axisymmetric meniscus waves with the instability, lending itself to thresholds below the prediction.

A similar set of modes were observed for experiments with reduced layer heights, where a FC70 layer of h_1=2.1 cm and a 1.5 cSt layer of h_2=2.0 cm, were used (cf. Figure 5-8). The effect of layer heights from the inviscid theory for two liquids was shown by Kumar & Tuckerman [52] where height dependence in the dispersion relation arises via the expression

$$\frac{\rho_1 + \rho_2}{\rho_1 \coth kh_1 + \rho_2 \coth kh_2}$$

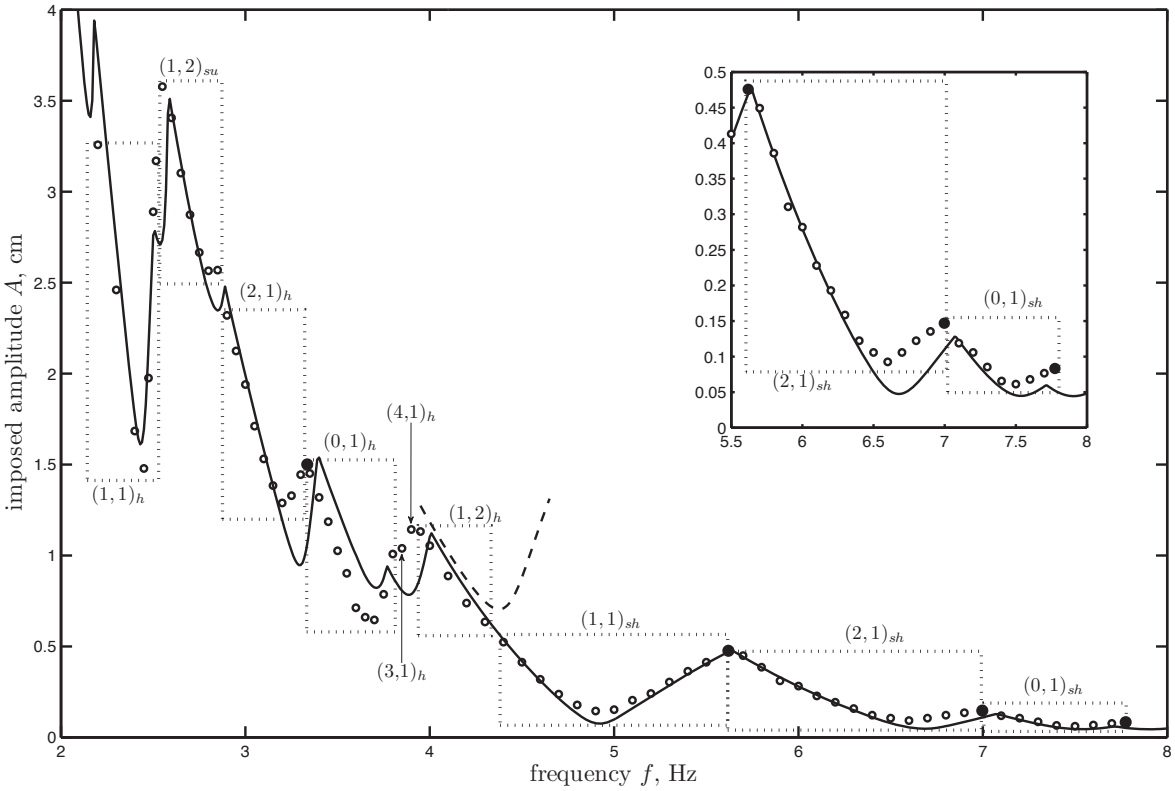

Figure 5-8. Theoretical comparison for the small height experimental system. Experimental thresholds and the corresponding theoretical curve is shown for a bilayer of FC70 (h_1=2.1 cm, rho_1=1916 kg m^{-3}) and 1.5 cSt silicone oil (h_2=2.0 cm, ρ_2=846 kg m^{-3}) in the R=2.55 cm cell. The dashed line represents the predicted $(1, 2)_{sh}$ threshold.

which shows saturation toward unity when kh_1 and kh_2 are greater than about 3. In this system, the expression leads to values of 0.89 for the (1,1) modes, 0.98 for the (2,1) modes, and 0.99 for the (0,1) modes indicating only moderate effect of height. Still, the resulting shift of the harmonic and subharmonic (1,1) modes are observed as predicted by the viscous theory. However it should be noted that the $(1,2)_h$ mode observed between 4 and 4.4 Hz just above threshold is not the predicted mode. The predicted threshold for the $(1,2)_h$ mode is shown in Figure 5-8 and is predicted to be higher than the $(1,1)_{sh}$ mode. The early presence of the $(1,2)_h$ mode observed in the small and large height systems give further reason to believe the existence of an interaction with the meniscus waves. The ordering of the modes in Figure 5-8 is largely the same as seen

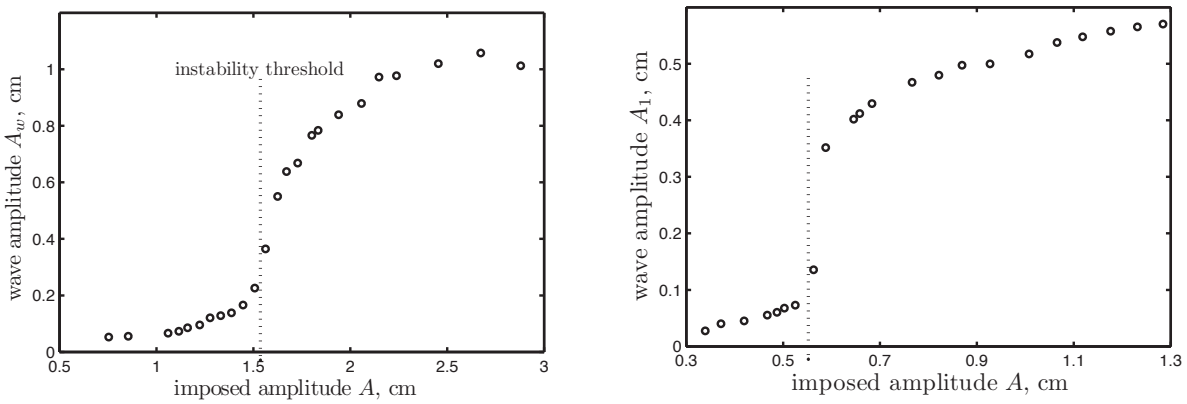

Figure 5-9. Saturated interface deflection owing to meniscus and parametric excitation. Wave amplitudes are from the large height system (see Figure 5-7) for imposed frequencies of (a) 2.52 Hz and (b) 3.68 Hz.

for the large height system, save for the region from 3.8 to 4 Hz, where instead of only $(3,1)_h$ modes, a $(4,1)_h$ mode was also observed. The predicted $(3,1)_h$ mode was damped considerably. Also absent from the experimental system are the $(4,1)_h$ modes predicted around 2.6 Hz. The trend here appears to be that wall damping increases substantially with the number of azimuthal nodes. Most clearly noticeable in the low height system is that the $(0,1)_h$ resonance is again much lower than predicted, for the same reason as given earlier for the large height system.

Saturated Interface Amplitudes

Figures 5-9 (a) and (b) present the saturated wave amplitude with respect to the imposed vibrational amplitude in the large height system (cf. Figure 5-7) for two different frequencies, roughly corresponding to the natural frequencies of the $(1,1)_h$ and $(0,1)_h$ modes. Here the wave amplitude has been taken as half the difference between the maximum and minimum interfacial heights. The general shapes of the response of Figures 5-9 (a) and (b) resemble those of Henderson & Miles [36] and Das & Hopfinger [23], but what is intended to be shown is smoothing of the response near the critical threshold as opposed to a sharp bifurcation. This smoothing of the response near the threshold was described as a “tailing” by Virnig *et al.* [79], who reported similar behavior

for the wave response of $(1,1)_{sh}$ modes in a rectangular cell using water. Addition of surfactant minimized the tailing in their experiments. In contrast to their observation of this behavior for a subharmonic mode, the tailing in the current work seems be characteristic of the interaction with the meniscus waves, as it was additionally noticed for the $(2,1)_h$ mode, but was nearly absent for the $(1,1)_{sh}$, $(2,1)_{sh}$, and $(0,1)_{sh}$ modes.

Higher Order Nonlinear Phenomena and the Path to Turbulence

In addition to practical reasons, the nonlinear behavior also serves to define the single-mode Faraday excitation as a fluid mechanical system, separating it from the more general description as a resonant nonlinear oscillator. A major benefit of the experiment is therefore the opportunity to observe real nonlinear phenomena, which more broadly are accounted for as nonlinear damping in dynamical systems analysis. These phenomena represent the initial departures from the “regular” behavior predicted by an evolution equation obtained from a weakly nonlinear analysis, where a linear mode grows and saturates to a finite amplitude. Knowing the amplifications at which these departures appear, one can reasonably set expectations for the possible agreement between the experiment and a weakly nonlinear theory. These phenomena are reported and discussed qualitatively, as the repeatability of nonlinear experiments was not rigorously investigated.

Saturation to a regular standing wave was common for excitation near the threshold for frequencies above or slightly below the natural frequency, standing in contrast to the breaking behavior observed for excitation well below the natural frequency. The images in Figure 5-10 depict the initial growth of a $(0,1)_{sh}$ mode above the natural frequency, at an amplitude sufficiently high to produce complex nonlinear behavior. It is seen that as the mode grows and approaches a maximum deflection amplitude there appear concentric ripples on the surface which modulate the spatial form of the mode, decrease mode amplitude, and then dissipate. Originating in all likelihood from shear effects resulting from higher velocities associated with higher amplification, this behavior adds

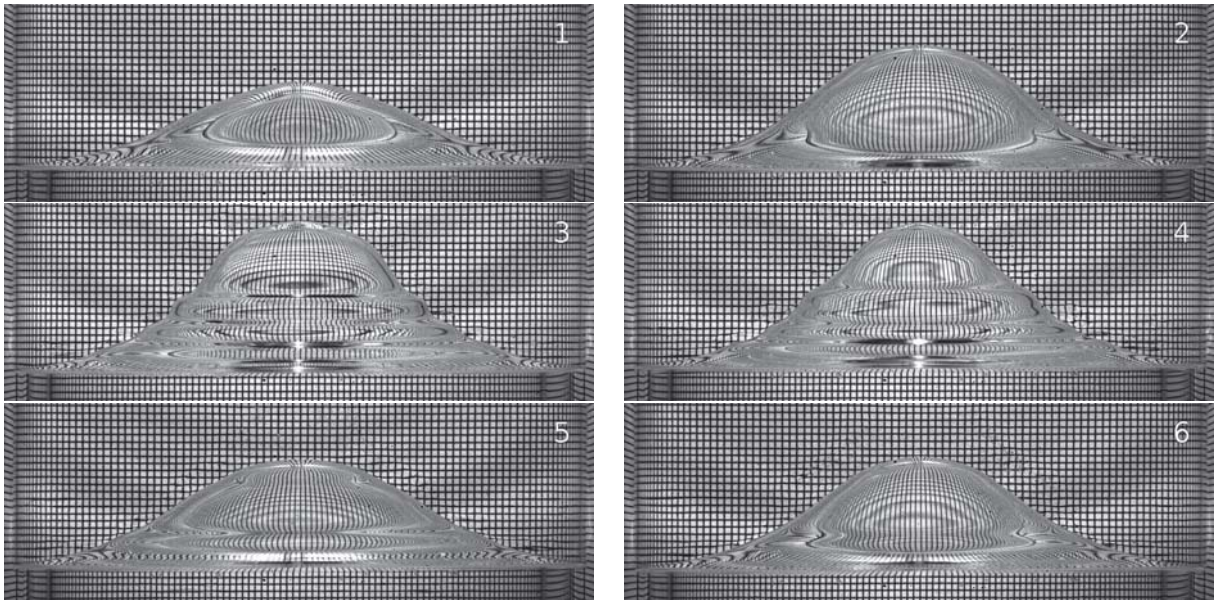

Figure 5-10. Shear instabilities on a $(0,1)_{sh}$ mode.Transient surface ripples appear during the growth of a $(0,1)_{sh}$ mode, excited at 7.65 Hz in the system of Figure 5-7. The sequence depicted spans eleven wave oscillations, and the presented images correspond to the maximum wave deflections of the 1st, 3rd, 5th, 7th, 9th, and 11th oscillations.

additional temporal periodicities to the mode dynamics. Further increase of the forcing amplitude at fixed frequency can cause the mechanism to either continue to reappear, or at even higher amplitudes, sustain itself. This behavior may be similar to the periodic modulation observed by Das & Hopfinger [23], but comparison to their images for the $(0,1)_{sh}$ mode reveals highly nonlinear waveforms, suggesting greater effects of surface tension.

Another mechanism by which new frequencies entered into the system is presented in 5-11, which shows the saturated excitation of a $(0,1)_{sh}$ mode, except at a lower frequency than 5-10. Here it is seen by careful inspection of the images that the polar position of the maximum deflection amplitude is different each subsequent cycle. In this case the mode actually orbits the central z-axis of the cell, in a clockwise motion when observed from above. The appearance of this motion, referred to as a "precessional state," is described by Tipton & Mullin [77], and with even greater detail, including

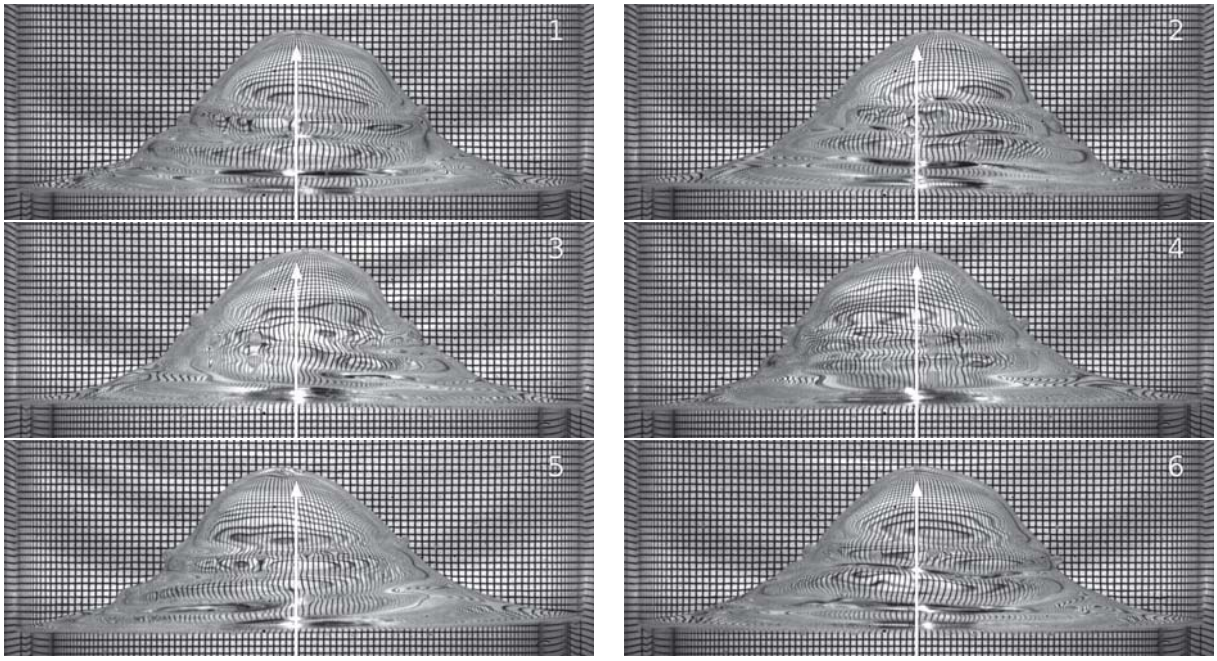

Figure 5-11. Precession of a $(0,1)_{sh}$ mode. Images depicting the orbiting of the $(0,1)_{sh}$ mode about the central z-axis, excited at 7.2 Hz in the system of Figure 5-7. Each image depicts the cell at every other trough of the imposed cell motion, i.e. at times t=0, 0.28, 0.56, 0.83, 1.11, 1.39 seconds.

measurements of the frequency of the precession, in the Ph.D. dissertation of Tipton [76]. The apparent contact line is clearly not horizontal in the 2nd and 5th images, suggesting the possibility of the superposition of another linear mode, albeit unpredicted by the theory. Quite interesting work on the interaction of two Faraday modes and the resulting phase space attractors has been done by Ciliberto & Gollub [20] and Henderson & Miles [36].

Secondary shear instabilities were commonly observed on (1,1) and (2,1) modes, as seen in Figures 5-12 and 5-13. These ripples appeared during the saturation of the mode and persisted throughout excitation, in contrast to the ripples of Figure 5-10 which would appear and disappear. These ripples appeared once the saturated mode amplification surpassed a threshold value, below which the mode retained its linear form. Further increase in the mode amplification caused bubbles to tear from the ripples, seen slightly in 5-12 and moreso in 5-13, and larger amplification naturally resulted in

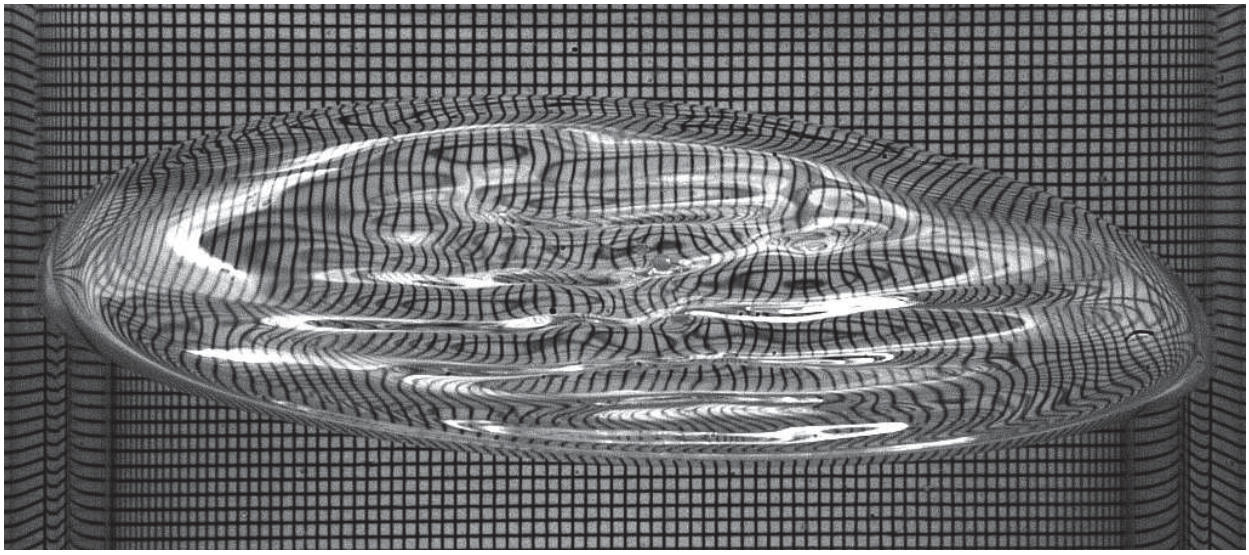

Figure 5-12. Shear instabilities on a $(1,1)_{sh}$ mode. Visualization of a standing $(1,1)_{sh}$ mode with surface ripples, excited at 5.6 Hz in the system of Figure 5-7.

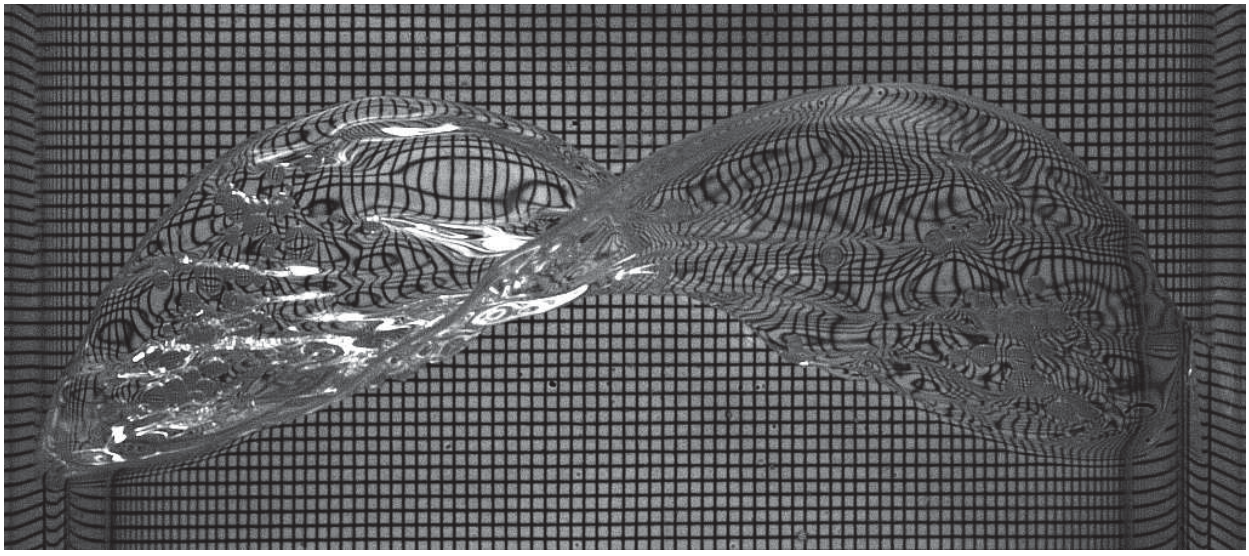

Figure 5-13. Shear instabilities on a $(2,1)_{sh}$ mode. Visualization of a standing $(2,1)_{sh}$ mode with surface ripples, excited at 6.8 Hz in the system of Figure 5-7.

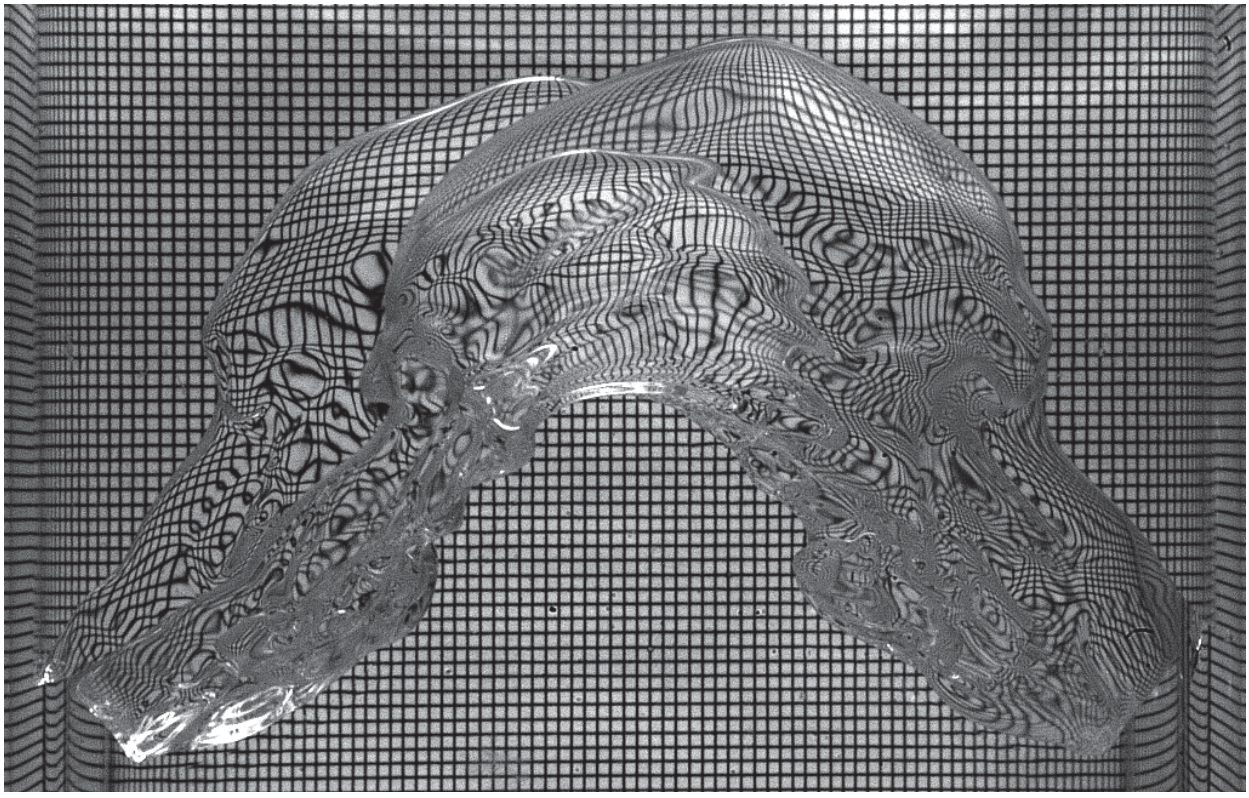

Figure 5-14. Breakup of a $(2,1)_{sh}$ mode. Visualization of the unbounded growth of a $(2,1)_{sh}$ mode, excited at 5.75 Hz in the system of Figure 5-7.

the unrestricted growth and breakup of the interface, see Figure 5-14. These ripples appear to have been suppressed by experiments with larger viscosity oils, ranging from 10 to 50 cSt.

The image sequence of Figure 5-15 shows highly nonlinear behavior typical of the breaking modes on the subcritical branches of the $(0,1)_{sh}$. Here the breakup pattern is guided by the continued growth of the secondary instabilities present in Figure 5-10, which turn over, collapse, and compress as the wave proceeds through its reverse cycle and breaks up. These patterns remain azimuthally uniform throughout most of this process, although non-uniform patterns were also observed. Although such patterns are well known in the realms of the Rayleigh-Taylor and Kelvin-Helmholtz instabilities, none have been reported in the reviewed experiments of single-mode excitation. It is believed the characteristic length scales of the breakup patterns are very dependent upon the

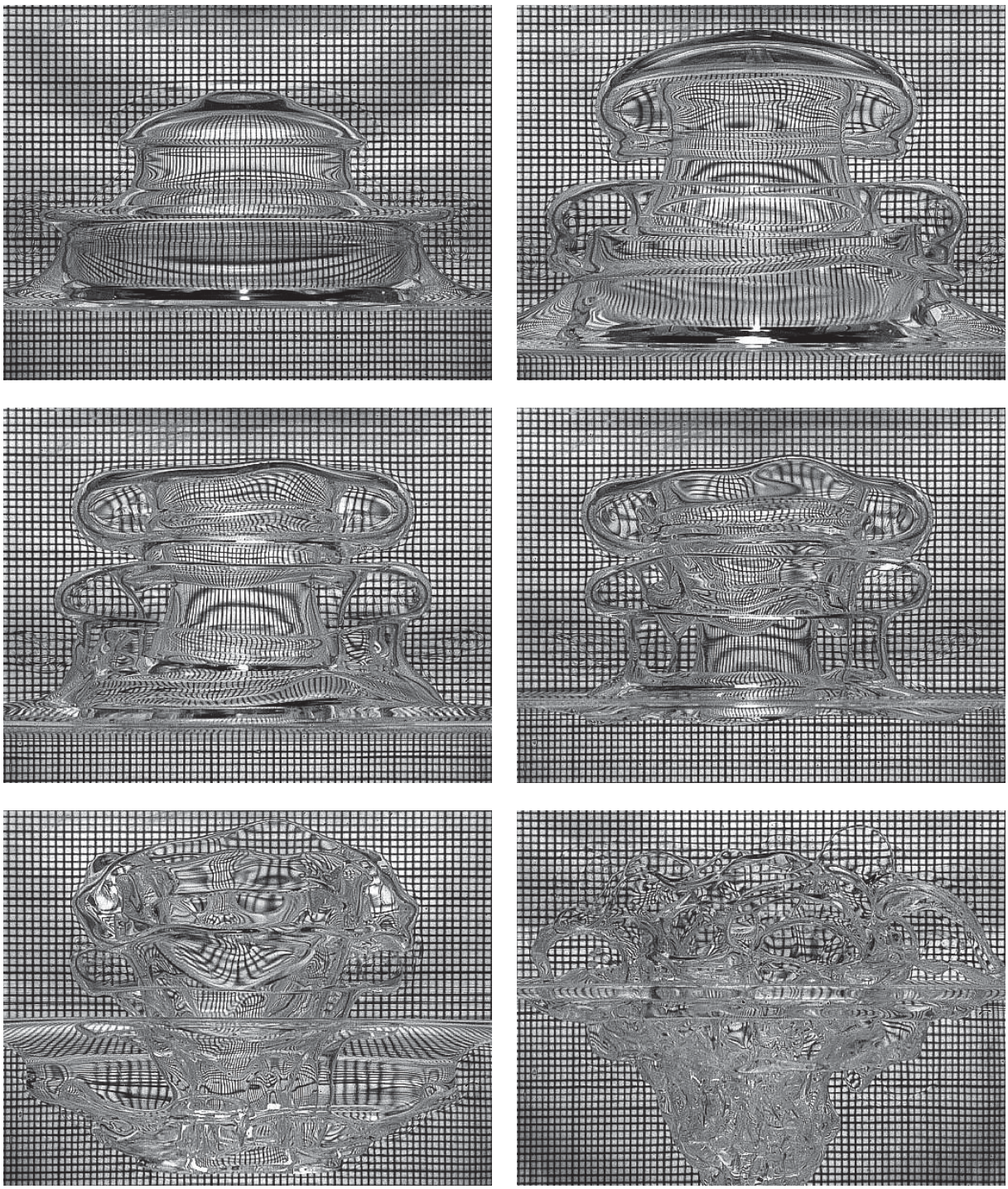

Figure 5-15. Ordered breakup of a $(0,1)_{sh}$ mode. The image series depicts a sequence of instabilities in the catastrophic breakup of a $(0,1)_{sh}$, excited at 7.4 Hz in the system of Figure 5-8.

dynamic viscosities of the two phases, as this seems to control the growth rates of the secondary instabilities which produce the behavior.

System Damping Study

A valuable and common measurement in the single-mode experiments is the rate at which an excited mode decays once the forcing has been stopped. These damping rates can be used to fit a linearly damped Mathieu equation to the observed thresholds, as in Henderson & Miles [36] and Tipton & Mullin [77], but in the case of the experiments in this study the rates will primarily be used to gauge the amount of dissipation in the system due to bulk viscous effects not included in Equation 3–1. The exponential rate of decay is determined by the slope of the logarithm of the ratio of the wave amplitude scaled by the initial value plotted against time. This was done for both harmonic and subharmonic (0,1) modes, for which the maximum wave height occurs at the z-axis. Imaging of the mode and selection of the time space of this central position produces a decay. The wave amplitude was then measured as half of the difference between the maximum wave amplitude and the apparent contact line. Extensive details on this method can be found in Keulegan [48], Henderson & Miles [36] and Das & Hopfinger [23].

To quantify the damping in the system, the (0,1) mode was both harmonically and subharmonically excited in the FC70-10 cSt silicone oil system and also in the large and small height FC70-1.5 cSt silicone oil systems. A total of eight measurements of the decay of an excited $(0,1)_h$ mode for the 10 cSt system were taken at excitation frequencies of 3.3 and 3.4 Hz with imposed amplitudes of 15 and 16 mm. Analysis of the time series of the wave amplitudes at the center of the cell yielded an average damping rate of 1.15 s^{-1}. Measurements for the $(0,1)_{sh}$ mode were taken at frequencies of 7 and 7.1 Hz with imposed amplitudes of 2.2 and 2.3 mm, yielding an average rate of 1.12 s^{-1}. Calculation of the linear viscous contribution from the interior with Equation (3–1) predicts a rate of 0.51 s^{-1} for both the harmonic and subharmonic

modes, suggesting that the remainder might be attributed to wall effects. Damping measurements for similar forcing parameters in the 1.5 cSt silicone oil systems yielded harmonic and subharmonic damping rates of 0.65 s^{-1} and 0.67 s^{-1} in the large height system and 0.58 s^{-1} and 0.57 s^{-1} in the small height systems. Here the interior contributions from Equation 3–1 are 0.397 s^{-1} and 0.395 s^{-1} for the small and large height systems, respectively. Comparison of the interior viscous damping to the overall measured damping reveals the sidewall effects of roughly 0.6 s^{-1} in the 10 cSt system and 0.18 to 0.25 s^{-1} in the 1.5 cSt systems. A conjecture that can therefore be made is that an upper fluid viscosity has a great effect on the dissipation owing to the film formation, as the thickness of this film was noticeably smaller for the experiments with 1.5 cSt silicone oil versus the 10 cSt oil. Henderson & Miles and Das & Hopfinger report measured $(0,1)_h$ decay rates of about 0.38 s^{-1} and 0.45 s^{-1} whereas the interior contributions are 0.022 s^{-1} and 0.0049 s^{-1}.

CHAPTER 6
DOUBLE-FREQUENCY EXPERIMENTS

This chapter presents the results of a limited study on excitation of the instability with vibrations composed of two frequencies, the linear theory for which has been presented and discussed in Chapter 2. These experiments reveal regimes in which the threshold behavior mimics that of the single frequency case and also where it shows new, unexpected behavior. Presented in Figure 6-1 (a)-(g) are data sets and the corresponding linear predictions for (M_1, M_2)=(3, 4) excitation of the FC70 and 1.5 cSt silicone oil system for various values of the frequency ratio χ. For low values of χ, Figures (a)-(c), the onset thresholds for the $(0,1)_h$ mode owing resonance with the $M_1\omega$ component are observed in accordance with the linear predictions, followed by the emergence of a $(1,1)_{sh}$ mode at higher χ in Figures 6-1 (d)-(g), owing to resonance with the $M_2\omega$ component. Figure 6-1 (h) best displays the transition from $M_1\omega$ to $M_2\omega$ resonance, where the threshold is measured for increasing values of χ when the basic frequency $f = \omega/2\pi$ is held fixed.

Linear Behavior

Excitation of the instability using two frequency components was qualitatively the same as with a single frequency, where meniscus waves persisted for amplitudes below threshold, and induction periods followed by growth and saturation or breakup prevailed at amplitudes above the threshold. The linear theory was also shown to again very accurately predict the threshold behavior, especially for the $(1,1)_{sh}$ mode at ratios of 22.5°, 35°, and 45° (Figures 6-1 (d)-(f)). The frequency band for each of these data sets was a little larger than predicted, due to the tongue damping observed in the neighboring $(3, 1)_h$ and $(2, 2)_h$ modes, in accordance with the deviation seen in the single frequency experiments for modes with higher numbers of azimuthal nodes.

The remarkable finding from the double-frequency experiments stemmed from the modifications seen to the $(0, 1)_h$ threshold due presumably to the interaction with

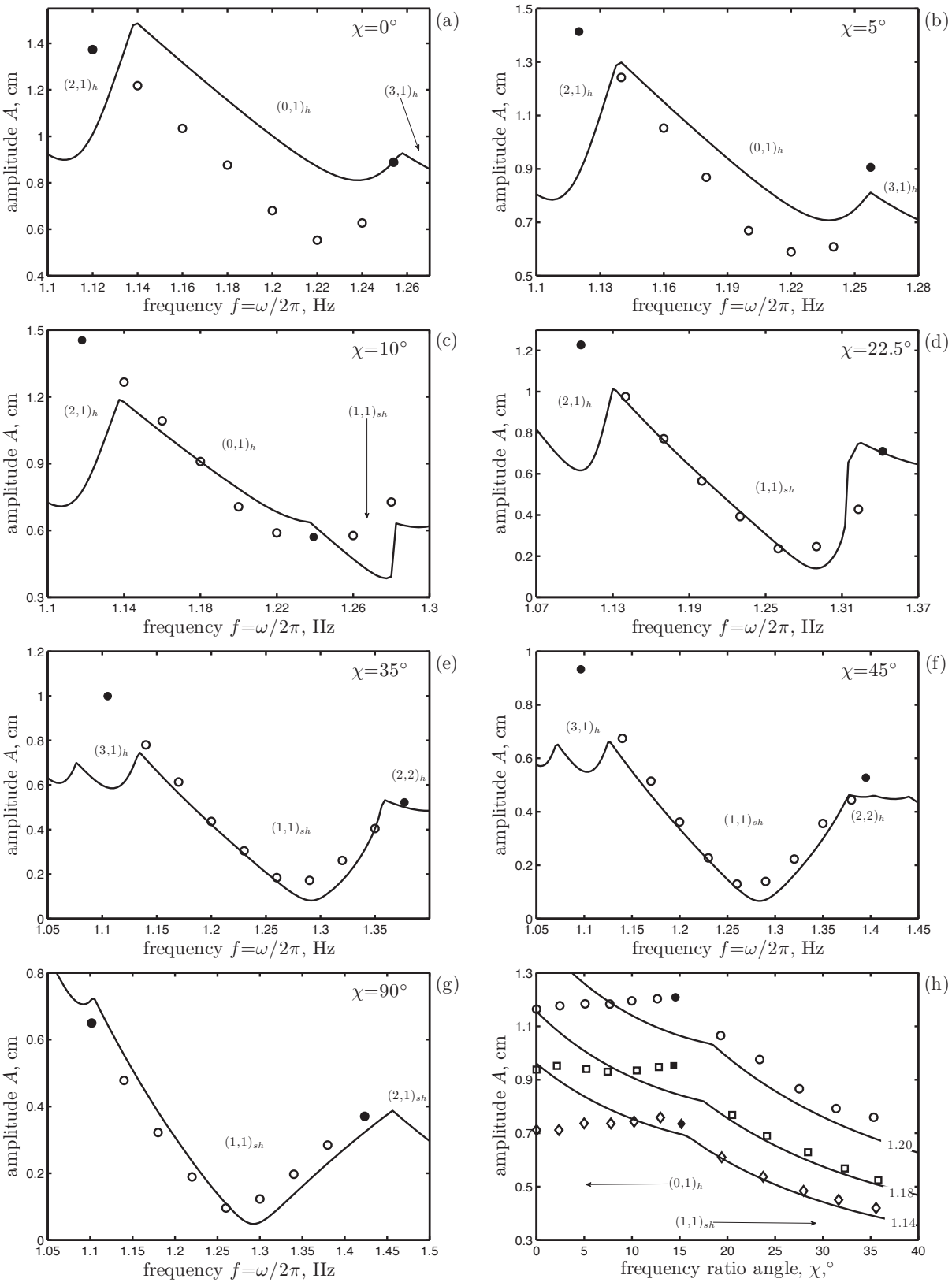

Figure 6-1. Threshold data and predictions with (M_1, M_2)=(3,4) excitation. System is FC70 (1905 kg m^{-3}, 3.1 cm) and 1.5 cSt silicone oil (846 kg m^{-3}, 3.3 cm) in the R=2.55 cm cylinder.

the meniscus waves. Relative to the single-frequency thresholds in Figure 6-1 (a), the data set obtained at χ=5° (Figure (b)), indicating slight addition of the 4ω component, shows a decrease in the deviation between the observed and predicted thresholds as one moves from the natural frequency (about 1.22 Hz) to the co-dimension 2 point. Excitation at χ=10° with greater $M_2\omega$ component in Figure (c) shows this deviation to continue to decrease, where the experimental thresholds actually cross the predictions, with higher-than predicted thresholds near the $(2, 1)_h$-$(0, 1)_h$ co-dimension 2 point. This behavior of the observed crossing the predicted threshold is highlighted in Figure 6-1 (h), by fixed frequency data sets, where it is seen that the observed thresholds remain nearly constant as χ is increased, in contrast to the predicted decrease.

Nonlinear Behavior and Interaction

Double-frequency excitation will be further described using the time space data for sets of harmonically and subharmonically excited (0,1) modes. These waves have saturated to a steady-state standing wave and are helpful for inferring both linear and characteristic nonlinear behavior. The parametric conditions were also set to in order to produce high wave amplification, but not so great that the linear form of the mode was altered by secondary instabilities or higher order damping mechanisms (see Chapter 5). Relative to threshold experiments where only the minimum threshold was required, these experiments were performed in an especially controlled manner, where the temperature fluctuations due to lamp use were minimized and the wall conditions were maintained at maximum wetting (see experimental repeatability, Chapter 4). Each excited wave owes its resonance to the $M_1\omega$=3ω component, meaning the wave executes three periods in the single cell period presented in the figures.

For reference, the $(0,1)_h$ wave was excited at the basic frequency f=1.2 Hz without addition of the 4ω component (χ=0°) at an amplitude of A=0.84 cm, and the resulting standing wave time space and cell displacement is shown in Figure 6-2. Evident from the wave motion is that the maximum wave amplitudes remain constant, denoted

by A_1, A_3 and A_5 in Table 6-1. The consistency of the reflections on the waves also indicates the absence of additional frequencies in the response and lends credence to the experimental control. The minimum wave amplitudes also remain constant, but are notably less than the maximum wave amplitude, indicating a non-symmetrical motion of the wave about the midplane and therefore also the nonlinear restoring force. This results from not only the density and viscosity contrast of the two phases, but also from the biased direction of gravity, the concavity of the meniscus and the film dynamics. The apparent contact line lags behind the wave crests, possibly due to the high meniscus wave amplitudes, which are greatly reduced in subharmonic excitation where the phase shift is nearly absent.

The $(0,1)_h$ waves resulting from excitation with 4ω component added are shown in Figures 6-3 (a) and (b). The main similarities between these waves and the single-frequency case of Figure 6-2 are that the minimum wave amplitudes are again less than the maximum amplitudes, and that the contact line lags the wave deflection. Examination of Table 6-1 reveals that not only have the average wave maxima (A_1, A_3, A_5) and minima (A_2, A_4, A_6) decreased with the increased ratio of the 4ω component, but there also enters internal variance from one of these maxima or minima to the next. The images visually confirm this by the slight distortion of the reflection from one wave to the next, which was not present in the single-frequency case. This may be expected theoretically, as the Floquet expansion is written for the basic frequency ω, and this periodicity in the experiment has remained intact.

A characteristic difference between single and double-frequency experiments, important to both linear and nonlinear behavior, results from the meniscus waves adopting the periodicity of the parametric vibrations. Thus when a second frequency is added to the forcing, the matching of the meniscus wave periodicity with that of the instability is lost, because the meniscus wave periodicity now also contains two frequencies, while the response of the instability, to first approximation, contains only

one frequency. The resulting mismatch of the meniscus wave periodicity with that of that of the instability is the central explanation offered for the observed thresholds crossing the predictions seen in Figure 6-1 (h).

Given the limited quantity of data, the intention of this analysis is to provide initial insight into the the characteristics and differences in the nonlinear behavior of modes excited by one and two frequencies. However, one quantitative comparison that will be made using this data is with regards to the differences between the average maximum and minimum wave heights. Saturated wave data similar to the $(0,1)_h$ excitation of Figures 6-2 and 6-3 is presented for the subharmonic analogue in Figure 6-4 for f=2.5 Hz, and A=0.098 cm excitation with frequency ratios of χ=0°, 13.9°, and 26.9°. Much like the harmonic experiments, deviation from the constant peak amplitudes and periodicity is seen as the second frequency is added. Notably different is the reduction of the phase lag of the contact line. Comparing the average peak amplitudes to the trough amplitudes, shown in Table 6-1, this ratio is consistently smaller for the subharmonic excitation (about 1.33) to that of the harmonic experiments (about 1.47), indicating a biased increase of the peak maxima relative to the minima in the harmonic experiments. This bias is accredited to the interaction with the meniscus waves, whose amplitudes were noted to be considerably greater in harmonic experiments than the subharmonic analogue where they were nearly absent (see Chapter 5).

Experimental Conclusion

This concludes the presentation and analysis of the observed excitation of single-mode Faraday waves with one and two frequency components. The study reveals the linear theory to be sufficient for predicting the critical thresholds for some regimes, while less so for those in which the sidewall non-ideality is able to interact with the instability. Most notable is the interaction between the harmonic fundamental axisymmetric mode and the meniscus waves of the same periodicity, and similar spatial form. The nature of this interaction is observed to change when the instability is excited

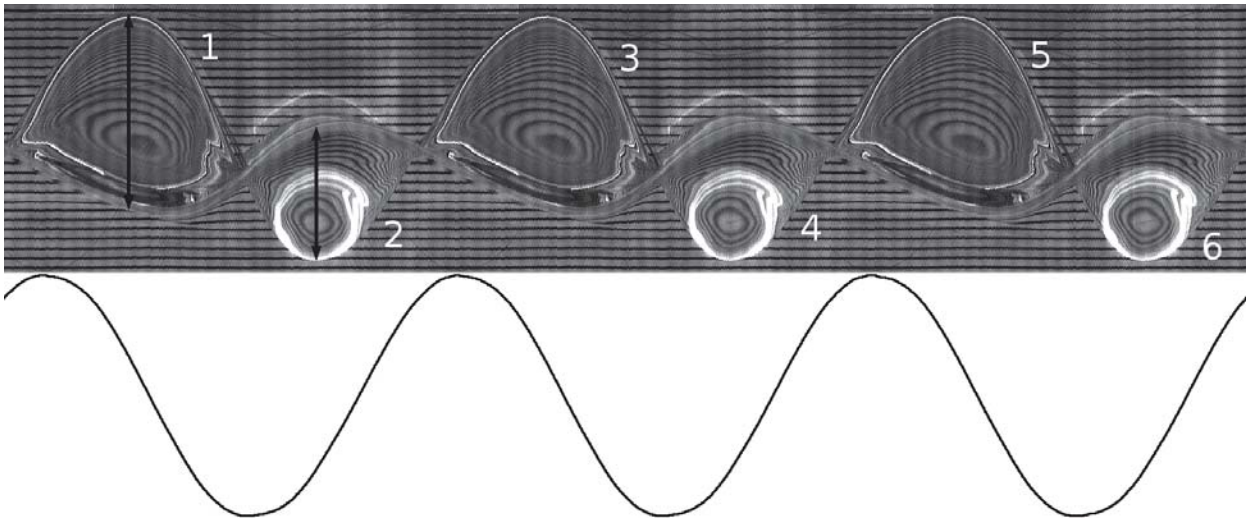

Figure 6-2. Saturated nonlinear data for a harmonic mode excited with a single frequency. Shown is the time space, in the oscillating reference frame, of the single frequency (3ω) excitation of a saturated $(0, 1)_h$ mode at $f=\omega/2\pi$=1.2 Hz and A=0.84 cm using the system of Figure 6-1. Time space data was collected for the maximum wave amplitude, as in Figure 4-2. Vertical length of the image represents an experimental length of 3.902 cm and the total time, represented by the horizontal length of the image, is 1.666 seconds. Below the image for comparison is the output cell displacement. All images in this chapter are of the same resolution. Wave amplitude measurements are reported in Table 6-1.

with two frequencies, due to the resulting mismatch between the wave periodicities. Analysis of the nonlinear saturation of experiments displays differences between the single and double-frequency cases, and also reveals more consequences of the interaction between the instability and the meniscus waves. A consequence of the addition of a second frequency component is the introduction of three more degrees of freedom, thereby greatly increasing the required scope to fully capture its effect on the phenomena. The double-frequency experiments of this study were restricted to the cases of (M_1, M_2)=(3,4) and the phase lag ϕ=0°. While the phase lag is known to have little effect on the linear predictions, intuition suggests an ability of it to adjust the interaction between the meniscus waves and the instability and ought to be the subject of future investigation.

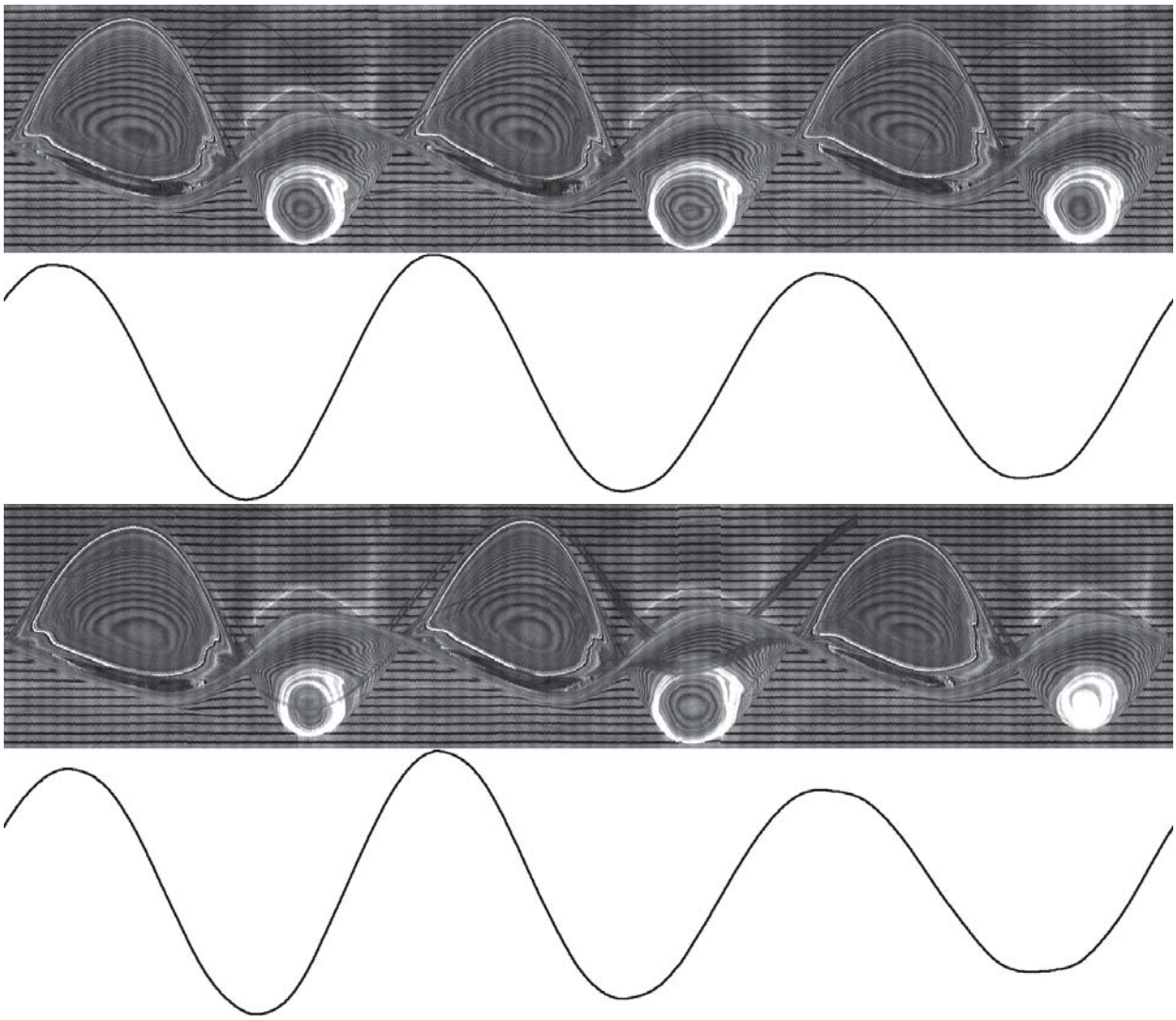

Figure 6-3. Saturated nonlinear data for harmonic modes excited with two frequencies. Shown is the time space data from system 6-1 for saturated $(0,1)_h$ modes excited at a frequency $f=\omega/2\pi$=1.2 Hz with (M_1,M_2)=(3,4) where χ=5.2° and A=0.84 cm (above) and χ=10.6° and A=0.84 cm (below). Wave amplitude measurements reported in Table 6-1.

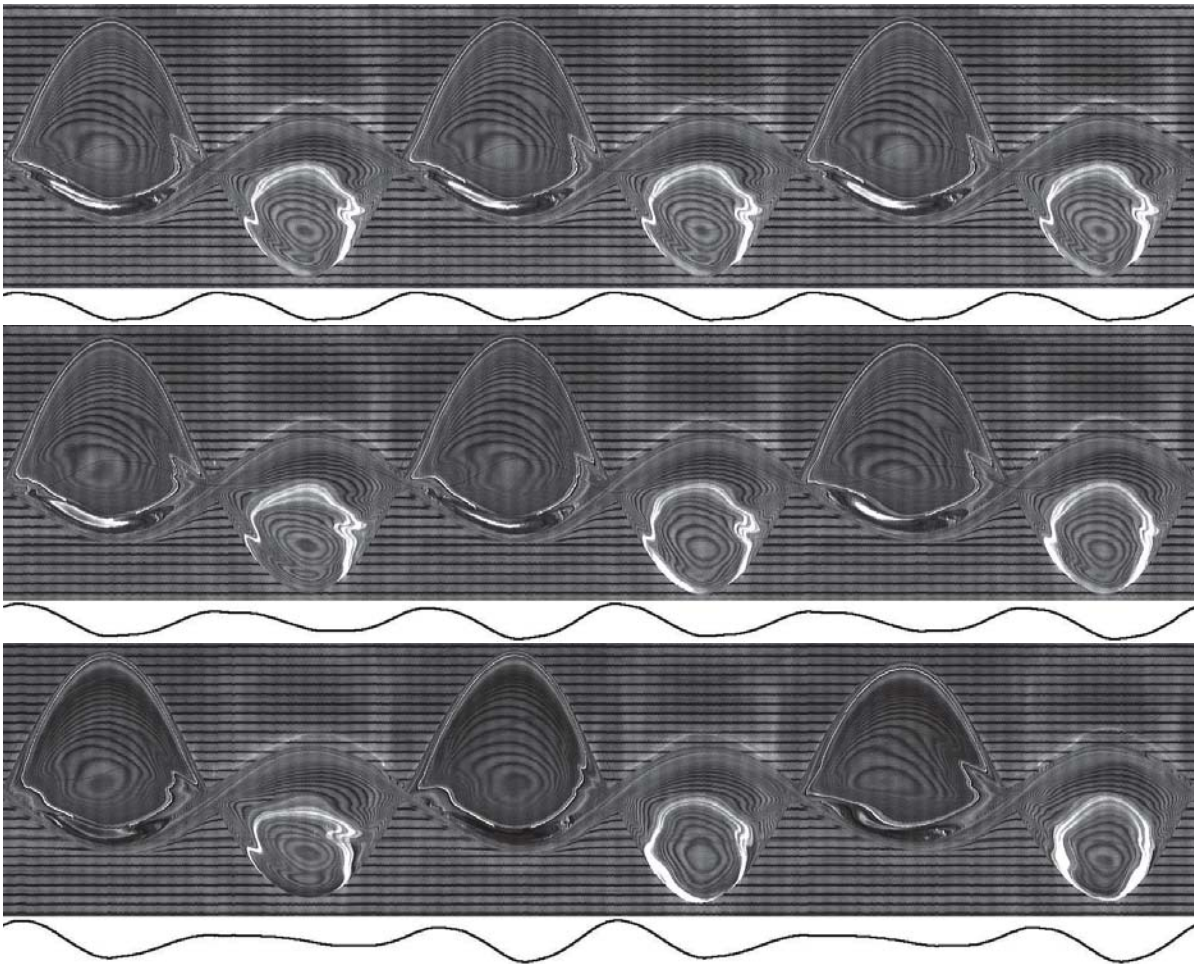

Figure 6-4. Saturated nonlinear data for subharmonic modes excited with two frequencies. Shown is the time space data from system 6-1 for saturated $(0,1)_{sh}$ modes excited at a frequency $f=\omega/2\pi$=2.5 Hz with (M_1,M_2)=(3,4) where χ=0° and A=0.097 cm (top), χ=13.9° and A=0.098 cm (middle), and χ=26.9° and A=0.098 cm (bottom). Wave amplitude measurements reported in Table 6-1.

Table 6-1. Parametric conditions and wave height measurements.

f, Hz	χ, °	A	A_c	A_1	A_2	A_3	A_4	A_5	A_6	$\frac{A_{odd}}{A_{even}}$
1.20	0	0.84	1.00	1.43	0.98	1.43	0.98	1.43	0.98	1.47
1.20	5.2	0.84	0.87	1.43	0.95	1.44	1.00	1.38	0.92	1.47
1.20	10.6	0.84	0.78	1.35	0.88	1.39	0.98	1.24	0.84	1.48
2.50	0	0.097	0.044	1.52	1.14	1.52	1.14	1.52	1.14	1.33
2.50	13.9	0.098	0.033	1.51	1.13	1.52	1.14	1.49	1.15	1.32
2.50	26.9	0.098	0.030	1.47	1.08	1.47	1.10	1.36	1.10	1.32

Data tabulated from Figures 6-2, 6-3, and 6-4. The amplitude A_c represents the fixed-frequency threshold amplitude predicted by the linear theory. An A subscripted with a number denotes half the wave heights measured according to the black arrows in Figure 6-2. Imposed and wave amplitudes measured in cm.

CHAPTER 7
FINAL DISCUSSION AND CONCLUDING REMARKS

Despite occurring in a fluid mechanical system, single mode Faraday wave excitation is unique in its ability to be generalized under the umbrella of parametric excitation of a nonlinear system with a single degree of freedom. An important realization made over the course of this work therefore was that all previous experiments measuring the critical thresholds had more or less adopted this generalization in regards to the theoretical explanation of their results. The first experiments of Benjamin & Ursell and Dodge *et al*. simply noted the deviation between their thresholds and the inviscid model, as they did not include any form of system damping. The later experiments of Henderson & Miles, Tipton & Mullin, and Das & Hopfinger each showed the assumption of linear damping to be valid as they each saw sufficient agreement with the linearly damped oscillator, and moved on to study higher order phenomena. What has set this work apart from the previous experiments was the motivation to design a system which respected the assumptions necessary to make connection with the equations of fluid mechanics, and most significantly, the stress-free boundary condition. This meant considerable effort was spent searching for a liquid system that could approximate the ideal behavior dictated by the theory. While not in it of itself a nobler way of investigating the phenomenon, the result was an increased efficiency of interpreting the nuanced phenomena which lead to theoretical mismatch, opening robust avenues for future investigation. These phenomena, along with the key aspects of the system design and method are the principle results of this scientific investigation and will be discussed.

Experimental Method

Realization of the Stress-Free Boundary Condition

Primarily, an extensive study of the Faraday threshold was conducted with single and double-frequency parametric excitation in the regime of mode discretization, and for the first time comparison has been made to the viscous linear stability theory of Kumar

& Tuckerman [52]. This theory, which is written for horizontally infinite systems, was adapted to finite size cylinders by application of a sidewall stress-free condition, allowing separation of variables and the study of individual modes of instability. While from one perspective this is an inviscid theory condition, because all real systems experience sidewall stresses owing to viscous boundary layers and capillary effects, in a viscous system close approximation has been shown possible when these sidewall stresses pale in comparison to the bulk stresses. This method of approximation requires careful selection of the participating fluids, which could only be determined by trial and error, as the behavior of an interface at the sidewall is extremely difficult to predict. The chosen liquids in this experiment, the fluorinert FC70 and silicone oil, produced an interface which happened to move very effortlessly over glass, over a film of the silicone oil (see Figures 5-3 and 5-4). While this film is not accounted for by the model, its associated stresses along with those of viscous boundary layers were found to be much less in comparison to the bulk domain linear viscous contribution (see Chapter 5). Furthermore the sidewall stresses were minimized by optimizing the upper phase viscosity, which both decreases the boundary layer stresses and the film thickness.

Experimental Repeatability

The path of investigation was strongly affected and driven towards study of the linear threshold by both the experimental repeatability and the data analysis techniques. Repeatability was first investigated in the context of being able to reproduce the observed linear threshold from one experiment to another. Troubling behavior was observed when excitation of the instability could require a considerably higher amplitude from the afternoon of one day to the morning of the next. Additionally it was seen the nonlinear behavior could change significantly during a series of experiments when the system was left sedentary for a fairly short period of time, as seen in the inconsistency of saturated wave amplitudes in Figures 4-7 (a) and (b). Along with the presence of the sidewall film, this behavior is believed to be dependent upon molecular-scale behavior

of silicone oil adsorption onto the glass, which sets a high standard for setting an experimental initial condition.

Experimental Initial Condition

For the reason of performing continued experiments over the course of the day, and also the fact that sidewall wetting was observed to produce lower thresholds, the initial condition of a completely de-wetted sidewall corresponding to the stagnant system was deemed impractical. The other option, a completely "wetted" sidewall initial condition was chosen, and was employed by continued excitation of the instability, with breaks taken while a standing mode was left in excitation. In regards to searching for a linear threshold, this method was sufficient as the threshold therefore decreased over the course of a run of experiments, and the actual thresholds, reported such as in Figures 5-7 and 5-8, are the lowest observed thresholds, believed to represent the case when the maximum wetting condition was met. While the time-spaces of Figures 6-2, 6-3 and 6-4 represent nonlinear experiments where the greatest care was taken to ensure the maximum wetting initial condition, future nonlinear experiments with this liquid system would require a more well-defined method of preparing the initial condition and several experiments be run to verify repeatability. The dependence of the observed phenomena on the sidewalls hearkens to the original results of Keulegan [48] where wave damping depended strongly on the container material. A promising modern-day solution which could offer tighter control of the wetting and thus the initial condition is nanoscale surface modification such as silanization, summarized by Blossey *et al.* [14].

Data Analysis Techniques

The electromechanical shaker was found to produce a mismatch between the programmed and the output vibrational amplitudes, which required the output amplitude to be measured individually for each experiment via image analysis. This method was tedious, but at the same time allowed for a smooth transition to the FFT analysis used for the double-frequency experiments. Image analysis for wave amplitude

measurements, on the other hand, was most inefficient, as it was first required to remove the vibrational reference frame from time space data, followed by manual tracing of the interface (example, Figure 6-2). This was an overly tedious method which seriously impeded nonlinear analysis, and therefore relegated focus to the linear threshold. The potential scope of experiments would increase dramatically from the ability to accurately measure a time series of the interfacial deflection, as long time dynamics and phase portrait behavior could be investigated. Henderson & Miles [36] employed a 1.15 mm diameter in situ capacitance type probe to measure deflections. Tipton [76] employed a non-intrusive method which may be better suited for immiscible systems, where the measurement of the deflection of a laser shown vertically through the system was used to infer both the surface gradient and deflection. Without the ability to efficiently measure wave deflections, much focus remained on the linear threshold, where only visual confirmation of the instability was required to mark a data point.

Experimental Results

The measured thresholds of Figures 5-7 and 5-8 form the central results of this work, and the comparison to the linear theory adapted to stress-free case enables very clear separation of the different non-idealities present in the system. First and foremost, however, the agreement between the observations and the predictions is quite good, from several perspectives. First, the observed thresholds across the entire frequency range follow the predictions very closely given the threshold amplitudes range from nearly 4 centimeters at low frequency to less than a millimeter at high frequency. Looking at individual modes, the experimental mode selection is also excellent, where the co-dimension 2 points forming the bounds of the frequency bands are positioned very near both the predicted frequencies and amplitudes. Careful examination of the observed thresholds reveals the possibility of frequency band shifts to both lower and higher frequencies, where it appears the $(1,1)_{sh}$ mode experiences a positive shift in Figure 5-7 and a negative shift in Figure 5-8. However, making these

claims with certainty is difficult because the shifts are very small and likely within the experimental control, given the accuracy to which the physical properties were known, and changes due to ambient temperature fluctuations. However, both positive and negative shifts were in fact observed in the previous experimentsnegative shifts were observed by Benjamin & Ursell, Miles & Henderson, and Das & Hopfinger while Dodge *et al*. and Ciliberto & Gollub observed positive frequency shifts. Notably the experiments of Dodge *et al*. and Ciliberto & Gollub were performed in large diameter cells, resulting in remarkably small frequency bands, suggesting a possible dependence of the frequency shift on the cell size. Prediction of damping rates and frequency shifts of waves depending on factors such as contact conditions and capillary effects have been performed by the likes of Miles [58], Mei & Liu [56] and Hocking [40].

Beyond the ambiguity of mode frequency shifts, definite trends can be gleaned from the the discrepancies seen between the experiments and the predictions based on the modal structure and the response periodicity. Deviation is observed for nearly all the modes near the natural frequencies, where the observed thresholds lie above the theoretical predictions, much like all of the previous experiments. This deviation can be seen to grow for modes with greater numbers of azimuthal nodes, as seen when comparing the $(0,1)_{sh}$ thresholds to the $(2,1)_{sh}$ thresholds in both Figures 5-7 and 5-8. This kind of trend is also seen in the $(0,1)_{sh}$ and $(3,1)_{sh}$ thresholds observed by Das & Hopfinger, Figure 3-1 (f).

The FC70 and silicone oil system used in these experiments offers a very promising starting point of connecting the instability to the sidewall behavior, because it is possible to establish a well-defined initial condition, if excitation is started for a system where the film has already been created and the wall “wetted” (see above, and Chapter 4). In preparing a consistent initial condition, considerations would have to be made regarding the rates at which the film drained and the actual contact line re-advanced in the sedentary system before excitation re-commenced. Thereafter, the interface

would ideally remain tethered to the same contact position for the duration of the experiment, and the apparent contact line motion would be connected to the stretching and contraction of the interface along the film. Ito *et al.* [44] presented a detailed comparative study between a model they proposed and the dynamics of the film formed in their experiments with water and kerosene, which could possibly be adapted to the initial condition proposed by this work. This film is also qualitatively similar to the behavior observed in the classical film-forming behavior of Landau & Levich [53]. Another important result that deserves explanation was the improvement of the theoretical agreement when the oil viscosity was reduced from 10 cSt to 1.5 cSt, as in Figure 5-5. If both sets of data were obtained for the same initial condition, with a film present and maximum sidewall wetting, the only difference noticeable to the linear theory ought be the increased damping due to the upper phase boundary layers.

In these experiments the stability thresholds are also reported for several harmonic and superharmonic modes, which have not received much attention from previous reports. There exists an abundance of work studying the forced excitation of vibrations in a system via excitation at or near the system natural frequency (see classical works by Rayleigh [68] and Nayfeh & Mook [63]), but this remains separate from the harmonic excitation of the Faraday instability in discretized systems, as it results from time-periodic, homogeneous terms in contrast to the inhomogeneous terms that give rise to forced oscillations. Harmonic excitation of the single-mode instability, near the natural frequency of the mode instead of twice as in subharmonic excitation, naturally occurs at higher amplitudes. This a result of the greater damping experienced by the harmonic mode, as it executes twice as many wave oscillations relative to the cell motion as the subharmonic case.

Meniscus Wave Inhomogeneity

The most interesting finding uncovered by these experiments is the interaction between the meniscus waves and the harmonic Faraday modes. The meniscus

effectively represents the loose, inhomogeneous connection required for the aforementioned forced oscillations, and the lower-than-predicted thresholds for the $(0,1)_h$ modes near 3.6 Hz in Figures 5-7 and 5-8 provide evidence of interaction between the forced and the parametric oscillations. Inclusion of a periodic inhomogeneity in the Mathieu equation means that for parametric amplitudes below the threshold there no longer exists a quiescent base state, but rather a finite, but non-growing amplitude that oscillates with the inhomogeneity. One possible avenue for theoretical comparison is modification of the current linear theory with the inhomogeneous Floquet theory of Slane & Tragesser [73], who show addition of an inhomogeneity can transition an asymptotically stable system to unbounded growth. Tipton [76] noted the possibility of interaction between meniscus waves and the subharmonic excitation of the (0,1) mode, but the effect would in all likelihood be considerably less detectable than the harmonic case where the meniscus wave amplitudes are far greater and the frequency is equal to that of the instability. The harmonic excitation of the (0,1) mode therefore serves as an excellent experiment for studying the mixed parametric and forced resonances. The work of HaQuang *et al.* [35] provides an excellent foundation for the nonlinear behavior of such a system, where they treat the generalized case of a parametrically and forced oscillator subject to both quadratic and cubic nonlinearities. The other harmonic modes in this Faraday system appear to also experience interaction with the meniscus waves, but due to the azimuthal mismatch of these modes with the meniscus waves the interaction is diminished.

Double-Frequency Phenomena

The experiments presented for the double-frequency excitation of single-mode Faraday waves in Chapter 6 are believed to be the first of their kind. Double-frequency excitation opens the door to a large increase in the number of parametric studies which can be conducted, including the dependence on the frequency spacing defined by M_1-M_2, the ratio of the components present in the parametric signal χ, and the

phase lag between the two components ϕ. In these experiments it was shown there exist regions of the stability space for different values of χ that exhibit agreement with the linear theory that is qualitatively the same as the single-frequency case, for the studied case of (M_1,M_2)=(3,4) and ϕ=0°. An interesting co-dimension 2 point appears in the double-frequency system, where increase in χ causes the transition from $M_1\omega$ to $M_2\omega$ resonance. The co-dimension 2 point contained in this transition thereby breaks the harmonic or subharmonic time symmetry of the response, a method used in high-frequency experiments to access new states of pattern formation (see Edwards & Fauve [28], Kudrolli *et al.* [50], and Arbell & Fineberg [3]). In single-mode experiments this is interesting for being able to choose which cell modes participate in the co-dimension 2 point, by adjustment of the parameters M_1 and M_2, offering a versatile extension to the spatiotemporal chaos Ciliberto & Gollub [20] observed between the $(4,3)_{sh}$ and $(7,2)_{sh}$ modes. The $(0,1)_h$ mode continues to show interesting threshold behavior, where the addition of the second frequency component does not change the threshold amplitude according to the predictions. Again this results from the interaction between the meniscus waves and the instability, which becomes further complicated by addition of the second frequency component as the matching of the periodicity is between the two waves is lost.

Nonlinear Behavior

The time space data of Figures 6-2, 6-3 and 6-4 displays behavior of saturated (0,1) modes excited both harmonically and subharmonically, and is meant to qualitatively outline behavior which could be matched by a weakly nonlinear theory. Henderson & Miles [36] notably compared their $(0,1)_{sh}$ mode amplitudes to the predictions of the nonlinear theory of Miles [59], again requiring the measured experimental damping ates. While a weakly nonlinear single-mode Faraday theory including the rigorous calculation of viscosity has not been written, the theory of Skeldon & Guidoboni [72] is a complete theory which acts as the nonlinear extension to the Floquet analysis of

Kumar & Tuckerman, exhaustively analyzing the Lyupanov functions for all possible waveforms in order to determine pattern selection. Extension of a weakly nonlinear Floquet analysis to a cylindrical, discretized system for prediction of mode amplitudes would be much simpler as the number of participating modes is considerably smaller. A complication in making comparison to the amplitudes of a careful nonlinear experiment that would have to be negotiated is the mismatch between the observed and theoretical thresholds. Beyond this the nonlinear theory would be valid for excitation that resulted in the growth and saturation of the linear waveform, below the thresholds at which highly nonlinear behavior begins to appear, as detailed in Chapter 6. A key observation of the time space images is that both the wave peak amplitude ratios and contact line phase lags are much more pronounced in the harmonic experiments than the subharmonic experiments, indicative of strong interaction with the meniscus waves, meaning a nonlinear theory would require incorporation of the inhomogeneous term suggested above. The induction times represent a phenomenon on the boundary of understanding, as it may either be related to stick-slip behavior of the wall or finite time phenomena. The phenomenon is reported by Das & Hopfinger but notably not so by Mullin & Tipton.

APPENDIX A
INVISCID RESULT AND COMMENTS

While Rayleigh[68] presented mathematical justification for the existence of a parametric threshold for subharmonic excitation, the seminal work of Benjamin & Ursell[11] offered the first connection between the instability and the equations of motion. The inviscid theory for Faraday waves is helpful for understanding the fundamental physical behavior, including mode dispersion. Their result equates the instability to the parametrically excited linear pendulum, and will be presented here as a special case of the viscous model presented in Chapter 2. Taking the upper layer to be passive and re-setting the interface to z=h and the lower surface to z=0, Benjamin & Ursell's inviscid result can be adapted by setting μ=0 in the perturbed normal stress balance, Equation 2–16,

$$-\rho\partial_t\partial_z w + \rho\left(g + A\omega^2\cos\omega t\right)\nabla_H^2\zeta = \gamma\nabla_H^4\zeta \text{ at } z = h. \tag{A–1}$$

The time derivative of the velocity profile $\partial_t w$ is calculated directly by setting $\mu = 0$ in Equation 2–18

$$\nabla^2\partial_t\mathbf{v} = 0 \tag{A–2}$$

whose characteristic solution is

$$\partial_t w = A\sinh kz + B\cosh kz \tag{A–3}$$

when $\nabla_H^2 = -k^2$. Noting the no-slip condition does not apply to inviscid theory, the pertinent boundary conditions are the time derivatives of the no-flow condition at the bottom surface and the kinematic condition at the interface

$$\partial_t w = 0 \text{ at } z = 0 \tag{A–4}$$

$$\text{and } \partial_t w = \partial_{tt}\zeta \text{ at } z = h. \tag{A–5}$$

Applying these conditions, the profile evaluates to

$$\partial_t w = \partial_{tt}\zeta \frac{\sinh kz}{\sinh kh} \tag{A–6}$$

and substitution into Equation A–1 yields

$$\partial_{tt}\zeta + \tanh kh \left[gk + \frac{\gamma k^3}{\rho} + A\omega^2 k \cos \omega t \right] \zeta. \tag{A–7}$$

The final result of Benjamin & Ursell is obtained by re-casting with the time transformation $T = \frac{1}{2}\omega t$ and the parameters

$$p = \frac{4 \tanh kh \left[gk + \frac{\gamma k^3}{\rho} \right]}{\omega^2} \text{ and } q = \frac{2kA\omega^2 \tanh kh}{\omega^2}, \tag{A–8}$$

revealing the classical form (see McLachlan[55]) of the Mathieu equation

$$\partial_{tt}\zeta + [p + 2q \cos T]\, \zeta = 0. \tag{A–9}$$

Especially useful are both the definition of a mode's natural frequency via $(p\omega^2)^{\frac{1}{2}}$ and the appearance of the $\tanh kh$ term, which can be used to gauge the whether or not the effect of layer height is saturated. In the context of linear stability, the interpretation of the stability chart of Benjamin & Ursell (Figure A-1) is identical to that of the viscous theory predictions, i.e. Figure 2-1, where the region inside and outside the fins correspond to growing and bounded solutions, respectively. Present in Figure A-1 are the points of perfect resonance occurring for infinitesimal forcing amplitudes, which vanish upon addition of a damping source. The Mathieu equation lends itself to numerical solution by time integration and specification of an initial condition, and representative stable and unstable solutions are presented in Figure A-2. Kumar & Tuckerman[52] present the inviscid theory for systems with two active layers, to which they add linear damping for the purpose of comparison to the predictions of their viscous theory.

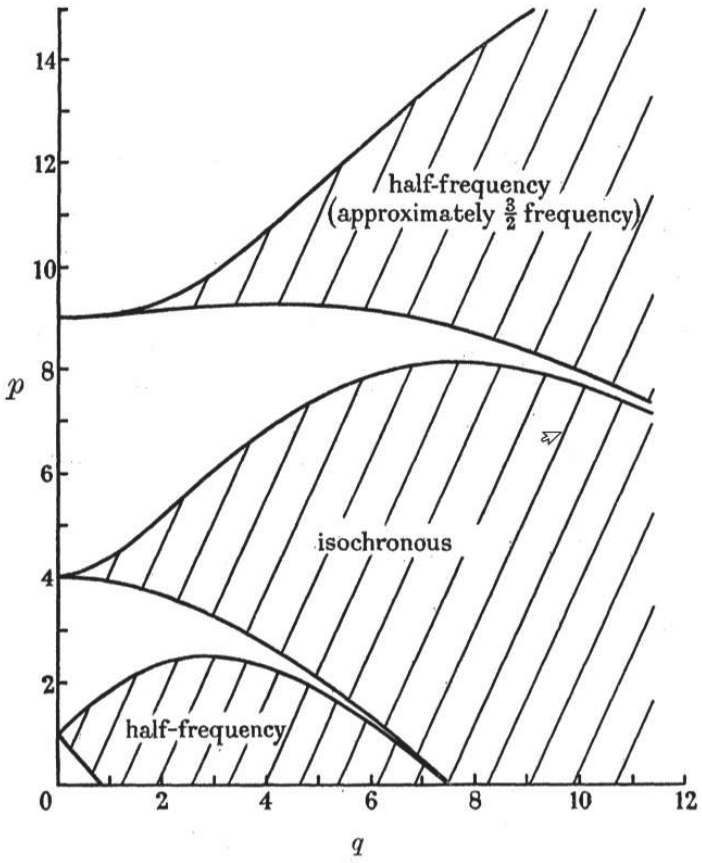

FIGURE 2. Stability chart for the solutions of Mathieu's equation

$$\frac{d^2a}{dT^2} + (p - 2q\cos 2T)\,a = 0.$$

Figure A-1. The stability diagram of Benjamin & Ursell.

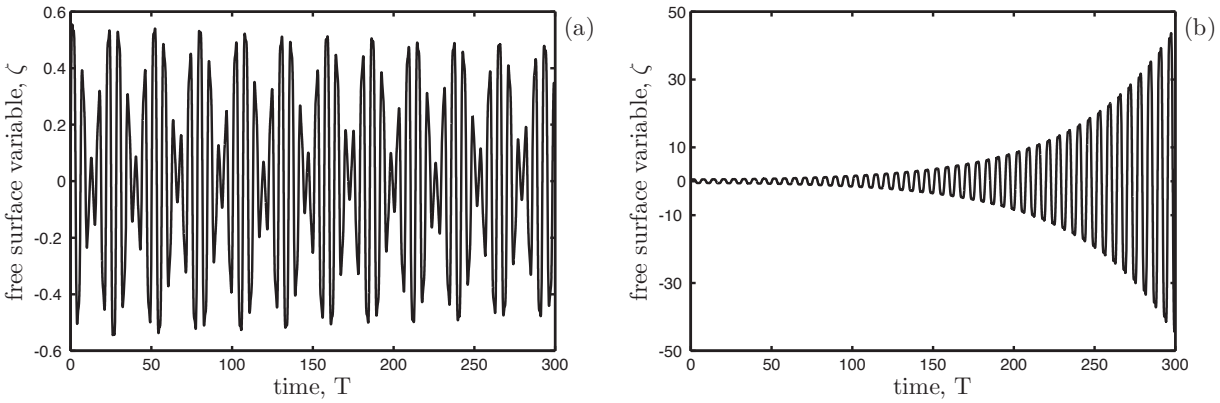

Figure A-2. Sample Mathieu equation solutions. Time development of the free surface variable ζ for (a) a stable solution (p, q)=(2, 1.15) and (b) an unstable solution (p, q)=(2, 1.213).

APPENDIX B
LINEAR STABILITY MATLAB® CALCULATION

The following MATLAB® code is a simple example of the types of calculations used to make the predictions throughout this work. The physical properties of the system input into the calculation are the layer heights, layer densities and viscosities, interfacial tension and gravitational acceleration. Specification of the imposed frequency and the wavenumber of interest along with the Fourier series cutoff completes the input, and execution of the code performs the linear stability calculation outlined in Chapter 2. The parameter input as-is outputs harmonic and subharmonic thresholds for the wavenumber k=259.5 m^{-1} in Figure 2-1, of which the subharmonic minimum is A=0.091 cm. This code serves as the foundation for all the calculations performed in this work.

```
clear all
%%%%%%%%%%% Required Parameter INPUT %%%%%%%%%%%
rho=[1880, 846]; %densities, kg/m^3
nu=[12, 1.5]; %kinematic viscosities, centiStokes
gamma=.007; %interfacial tension, kg/s^2
h=[.005,.005]; %layer heights, m
g=9.81; %gravitational acceleration, m/s^s
f=9; %imposed frequency, Hz
k=259.5; %wavenumber, m^-1
sigma=0; %mode growth rate, s^-1, zero for neutral stability
N=10; %Fourier series cutoff

%%%%%%%% Calculation proceeds from HERE %%%%%%%%%
thresholds=zeros(4,2); %calculation output variable, and contains
    the harmonic and subharmonic neutral stability amplitudes
nu=nu/1e6; %kinematic viscosity conversion, cSt to m^2/s
```

```
16 mu=rho.*nu; %dynamic viscosity calculation, kg*/m*s
17 omega=2*pi*f; %frequency conversion, Hz to radians/s
18 INDEX1=0;
19 for alpha=[0,1/2*omega]; %harmonic and then subharmonic solutions
20     INDEX1=INDEX1+1;
21         D=zeros(2*(N+1)); %eigenvalue problem D-matrix initialize
22         for n=0:N; %loop to calculate the D-matrix coefficients
               for each Fourier mode n
23             fexp=(mu+1i*(alpha+n*omega)); %Fourier-Floquet
                   exponent
24             q1=sqrt(k^2+1/nu(1)*fexp); %characteristic solution
                   exponent1
25             q2=sqrt(k^2+1/nu(2)*fexp); %characteristic solution
                   exponent2
26             b=zeros(8,1); %initialization of inhomogeneity in
                   boundary condition system of equations
27             b(8)=fexp; %insertion of Floquet exponent arising
                   from kinematic condition
28             %Here the matrix defined by the system of equations
                   arising from the boundary conditions is
                   constructed. The characteristic velocity
                   solutions include z*exp(k*z) and z*exp(-kz)
                   instead of exp(q1*z) and exp(q2*z) when q1=q2=0
                   and the coefficients for these solutions are
                   calculated first.
29             if fexp==0
```

```
30  fhs=[exp(-k*h(1)), exp(k*h(1)), h(1)*exp(-k*h(1))
        , h(1)*exp(k*h(1)), 0, 0, 0, 0; %no flow
        condition, bottom surface
31       0, 0, 0, 0, exp(k*h(2)), exp(-k*h(2)), h(2)*
           exp(k*h(2)), h(2)*exp(-k*h(2)); %no flow,
           top surface
32       k*exp(-k*h(1)), -k*exp(k*h(1)), h(1)*k*exp(-k
           *h(1))+exp(-k*h(1)), -h(1)*k*exp(k*h(1))+
           exp(k*h(1)), 0, 0, 0, 0; %no slip
           condition, bottom surface
33       0, 0, 0, 0, k*exp(k*h(2)), -k*exp(-k*h(2)), h
           (2)*k*exp(k*h(2))+exp(k*h(2)), -h(2)*k*exp
           (-k*h(2))+exp(-k*h(2)); %no slip, top
           surface
34       -1, -1, -1, -1, 1, 1, 1, 1,; %continuity of
           velocity at the interface
35       -k, k, -1, -1, k, -k, 1, 1; %continuity of
           velocity z-derivative at the interface
36       -mu(1)*2*k^2, -mu(1)*2*k^2, -mu(1)*(k^2+2*k),
            -mu(1)*(k^2-2*k), mu(2)*2*k^2, mu(2)*2*k
           ^2, mu(2)*(k^2+2*k), mu(2)*(k^2-2*k); %
           continuity of tangential stresses at the
           interface
37       1, 1, 1, 1, 0, 0, 0, 0]; %kinematic condition
           . equally can be written as 0, 0, 0, 0,
           1, 1, 1, 1]
```

```
38          coeff=fhs\b; %calculation of the velocity profile
                coefficients
39          dz1=coeff(1)*k-coeff(2)*k+coeff(3)-coeff(4); %
                evaluation of first z-derivative of the lower
                layer velocity profile at z=0
40          dzzz1=coeff(1)*k^3-coeff(2)*k^3+coeff(3)*3*k^2+
                coeff(4)*3*k^2; %third z-derivative of the
                lower layer
41          dz2=coeff(5)*k-coeff(6)*k+coeff(7)-coeff(8); %
                first z-derivative of the upper layer
42          dzzz2=coeff(5)*k^3-coeff(6)*k^3+coeff(7)*3*k^2+
                coeff(8)*3*k^2; %third z-derivative of the
                upper layer
43          Dn=(rho(2)*fexp+3*mu(2)*k^2)*dz2-mu(2)*dzzz2-((
                rho(1)*fexp+3*mu(1)*k^2)*dz1-mu(1)*dzzz1)+((
                rho(2)-rho(1))*g-gamma*k^2)*k^2; %evaluation
                of the D-matrix coefficients for each Fourier
                mode n
44      else %calculation for when q1=q2 are not zero. Same
            format as above.
45          fhs=[exp(-k*h(1)), exp(k*h(1)), exp(-q1*h(1)),
                exp(q1*h(1)), 0, 0, 0, 0;
46              0, 0, 0, 0, exp(k*h(2)), exp(-k*h(2)), exp(q2
                    *h(2)), exp(-q2*h(2));
47              k*exp(-k*h(1)), -k*exp(k*h(1)), q1*exp(-q1*h
                    (1)), -q1*exp(q1*h(1)), 0, 0, 0, 0;
```

```
48                  0, 0, 0, 0, k*exp(k*h(2)), -k*exp(-k*h(2)),
                        q2*exp(q2*h(2)), -q2*exp(-q2*h(2));
49                  -1, -1, -1, -1, 1, 1, 1, 1,;
50                  k, -k, q1, -q1, -k, k, -q2, q2;
51                  mu(1)*2*k^2, mu(1)*2*k^2, mu(1)*(k^2+q1^2),
                        mu(1)*(k^2+q1^2), -mu(2)*2*k^2, -mu(2)*2*k
                        ^2, -mu(2)*(k^2+q2^2), -mu(2)*(k^2+q2^2);
52                  1, 1, 1, 1, 0, 0, 0, 0];
53              coeff=fhs\b;
54              dz1=coeff(1)*k-coeff(2)*k+coeff(3)*q1-coeff(4)*q1
                    ;
55              dzzz1=coeff(1)*k^3-coeff(2)*k^3+coeff(3)*q1^3-
                    coeff(4)*q1^3;
56              dz2=coeff(5)*k-coeff(6)*k+coeff(7)*q2-coeff(8)*q2
                    ;
57              dzzz2=coeff(5)*k^3-coeff(6)*k^3+coeff(7)*q2^3-
                    coeff(8)*q2^3;
58              Dn=(rho(2)*fexp+3*mu(2)*k^2)*dz2-mu(2)*dzzz2-((
                    rho(1)*fexp+3*mu(1)*k^2)*dz1-mu(1)*dzzz1)+((
                    rho(2)-rho(1))*g-gamma*k^2)*k^2;
59          end
60          D(2*n+1,2*n+1)=real(Dn); %placement of the real and
                imaginary components Dn in the D-matrix
61          D(2*n+1,2*n+2)=-imag(Dn);
62          D(2*n+2,2*n+1)=imag(Dn);
63          D(2*n+2,2*n+2)=real(Dn);
64      end
```

```
65
66          B=zeros(2*(N+1)); %construction of the B matrix
67          if alpha==0; %harmonic
68              B(1,3)=2;
69              B(3:2*(N+1),1:2*N)=eye(2*N);
70              for i=1:2*(N-1)
71                  B(2+i,4+i)=1;
72              end
73          else %subharmonic
74              B(1,1)=1;
75              B(2,2)=-1;
76              B(3:2*(N+1),1:2*N)=eye(2*N);
77              for i=1:2*N
78                  B(i,2+i)=1;
79              end
80          end
81
82          [eigenvecs, eigenvals]=eig(D,1/2*(rho(2)-rho(1))*k^2*B);
              %solution of the eigenvalue problem
83          eigenvals=diag(eigenvals);
84
85          index1=0; %routine used to sort through the obtained
              eigenvalues
86          for index2=1:length(eigenvals) %
87              if isnan(eigenvals(index2)) %NaN eigenvalues ignored
88              elseif isinf(eigenvals(index2)) %infinite eigenvalues
                    ignored
```

```
89              elseif abs(imag(eigenvals(index2)))>1e-6 %super tiny
                    eigenvalues ignored
90              elseif eigenvals(index2)<0  %negative eigenvalues
                    ignored
91              else
92                  index1=index1+1; %index set for positive
                        eigenvalues
93                  evals(index1)=eigenvals(index2); %eigenvalue
                        stored in evals vector
94                  if abs(imag(evals(index1)))<1e-6 %disposal of
                        super tiny complex parts
95                      evals(index1)=real(evals(index1));
96                  end
97              end
98          end
99          evals=sort(evals); %sorting of the obtained eigenvalues
100         evals=100/omega^2*evals; %conversion from acceleration
                Aomega^2 to amplitude A, centimeters
101         thresholds(:,INDEX1)=evals(1:4)'; %output variable
102 end
```

APPENDIX C
$\mathcal{B}_{M1}$ AND $\mathcal{B}_{M2}$

For $(M_1, M_2) = (2, 3)$ and N=9, we have

$$\mathcal{B}_{M_1} = \begin{bmatrix} 0 & 0 & 0 & 0 & 2 & 0 & 0 & 0 & 0 & 0 \\ 0 & 0 & 0 & 0 & 0 & 0 & 0 & 0 & 0 & 0 \\ 1 & 0 & 0 & 0 & 0 & 0 & 1 & 0 & 0 & 0 \\ 0 & -1 & 0 & 0 & 0 & 0 & 0 & 1 & 0 & 0 \\ 1 & 0 & 0 & 0 & 0 & 0 & 0 & 0 & 1 & 0 \\ 0 & 1 & 0 & 0 & 0 & 0 & 0 & 0 & 0 & 1 \\ 0 & 0 & 1 & 0 & 0 & 0 & 0 & 0 & 0 & 0 \\ 0 & 0 & 0 & 1 & 0 & 0 & 0 & 0 & 0 & 0 \\ 0 & 0 & 0 & 0 & 1 & 0 & 0 & 0 & 0 & 0 \\ 0 & 0 & 0 & 0 & 0 & 1 & 0 & 0 & 0 & 0 \end{bmatrix}$$

$$\mathcal{B}_{M_2} = \begin{bmatrix} 0 & 0 & 0 & 0 & 0 & 0 & 2e^{i\phi} & 0 & 0 & 0 \\ 0 & 0 & 0 & 0 & 0 & 0 & 0 & 0 & 0 & 0 \\ 0 & 0 & e^{-i\phi} & 0 & 0 & 0 & 0 & 0 & e^{i\phi} & 0 \\ 0 & 0 & 0 & -e^{-i\phi} & 0 & 0 & 0 & 0 & 0 & e^{i\phi} \\ e^{-i\phi} & 0 & 0 & 0 & 0 & 0 & 0 & 0 & 0 & 0 \\ 0 & -e^{-i\phi} & 0 & 0 & 0 & 0 & 0 & 0 & 0 & 0 \\ e^{-i\phi} & 0 & 0 & 0 & 0 & 0 & 0 & 0 & 0 & 0 \\ 0 & e^{-i\phi} & 0 & 0 & 0 & 0 & 0 & 0 & 0 & 0 \\ 0 & 0 & e^{-i\phi} & 0 & 0 & 0 & 0 & 0 & 0 & 0 \\ 0 & 0 & 0 & e^{-i\phi} & 0 & 0 & 0 & 0 & 0 & 0 \end{bmatrix}.$$

for harmonic (α=0) responses, and

$$\mathcal{B}_{M_1} = \begin{bmatrix} 0 & 0 & 1 & 0 & 1 & 0 & 0 & 0 & 0 & 0 \\ 0 & 0 & 0 & -1 & 0 & 1 & 0 & 0 & 0 & 0 \\ 1 & 0 & 0 & 0 & 0 & 0 & 1 & 0 & 0 & 0 \\ 0 & -1 & 0 & 0 & 0 & 0 & 0 & 1 & 0 & 0 \\ 1 & 0 & 0 & 0 & 0 & 0 & 0 & 0 & 1 & 0 \\ 0 & 1 & 0 & 0 & 0 & 0 & 0 & 0 & 0 & 1 \\ 0 & 0 & 1 & 0 & 0 & 0 & 0 & 0 & 0 & 0 \\ 0 & 0 & 0 & 1 & 0 & 0 & 0 & 0 & 0 & 0 \\ 0 & 0 & 0 & 0 & 1 & 0 & 0 & 0 & 0 & 0 \\ 0 & 0 & 0 & 0 & 0 & 1 & 0 & 0 & 0 & 0 \end{bmatrix}$$

$$\mathcal{B}_{M_2} = \begin{bmatrix} 0 & 0 & 0 & 0 & e^{-i\phi} & 0 & e^{i\phi} & 0 & 0 & 0 \\ 0 & 0 & 0 & 0 & 0 & -e^{-i\phi} & 0 & e^{i\phi} & 0 & 0 \\ 0 & 0 & e^{-i\phi} & 0 & 0 & 0 & 0 & 0 & e^{i\phi} & 0 \\ 0 & 0 & 0 & -e^{-i\phi} & 0 & 0 & 0 & 0 & 0 & e^{i\phi} \\ e^{-i\phi} & 0 & 0 & 0 & 0 & 0 & 0 & 0 & 0 & 0 \\ 0 & -e^{-i\phi} & 0 & 0 & 0 & 0 & 0 & 0 & 0 & 0 \\ e^{-i\phi} & 0 & 0 & 0 & 0 & 0 & 0 & 0 & 0 & 0 \\ 0 & e^{-i\phi} & 0 & 0 & 0 & 0 & 0 & 0 & 0 & 0 \\ 0 & 0 & e^{-i\phi} & 0 & 0 & 0 & 0 & 0 & 0 & 0 \\ 0 & 0 & 0 & e^{-i\phi} & 0 & 0 & 0 & 0 & 0 & 0 \end{bmatrix}$$

for subharmonic (α=$\frac{\omega}{2}$) responses.

APPENDIX D
OUTREACH SUMMARY OF WORK

The work of this dissertation is the result of a detailed theoretical and experimental study of a phenomenon originally discovered by Faraday in 1831. Faraday saw that when he held a vibrating violin bow to the bottom of a plate holding a liquid, tiny waves would form and vibrate on the surface. His experiments showed that the patterns formed by the waves, which he called “beautiful crispations,” changed depending on the liquids he used and the note he struck with his violin bow. Over 150 years later, we have a detailed understanding of the mathematics that explain these patterns, and have also performed many experiments which show new behavior not seen by Faraday. What will be described in this appendix is that this phenomenon of Faraday’s waves, can be deeply understood from the perspective of some simple experiments, analogies, and physical principles of everyday life such as resonance and friction.

What Faraday’s violin bow effectively did to the plate of liquid was to cause it to move up and down in a regular motionat a certain frequency. Before discussing the meaning of this up and down motion, it will be noted that Faraday made a very important observation, which was that the tiny ripples on the surface would move up and down each time the plate moved up and down. Described here is a resonancethat the frequency of the up and down ripple motion was equal to the up and down motion of the plate. He also observed that the note struck on the bow had to be loud enough for anything to happen on the surface. The combination of these two observations are the signature of parametric resonance, a phenomenon observed in many other systems, and most notably the pendulum. To further explain the nature of this work and Faraday’s experiment, an analogy between a liquid interface and a pendulum will be made.

A pendulum, like that of a grandfather clock, consists of a mass attached to a rod or string which is held at a fixed position. At rest, the pendulum bob points in the direction of gravity, and when pulled away and released, it swings back and forth about the rest

position at a regular frequency. This was taken advantage of by Christian Huygens [41] who invented the first pendulum clock. The frequency of oscillation about the rest position depends upon the length and the mass of the pendulum bob. It can be seen that short clock pendulums oscillate quite rapidly relative to the 67 meter long Foucault pendulum which hanged at the Pantheon in Paris, France, and required over 16 seconds to complete one period of oscillation.

Another important idea in being able to complete the analogy between a pendulum and the surface ripples observed by Faraday is that of energy dissipation. When the the pendulum is pulled away from the rest position, energy is put into the system, which, when the bob is released, tends to keep the system in motion. However, in any real system, maintenance of this energy in the system is difficult and is gradually lost, or dissipated. In the case of the pendulum, energy is lost due to frictional effects such as the string connection to the fixed point or even air resistance due to the bob motion. Eventually the loss of energy results in the decay of the bob motion until it stops at the rest position. This energy loss is compensated in pendulum clocks by winding of the clock, that is, a storage of energy in a spring.

In the context of explaining Faraday's phenomenon of waves appearing on a vertically vibrated liquid surface, these waves exhibit the same behavior as just described for pendulums where there exists a natural frequency and there exist sources of energy loss. Imagining kids playing in a pool, the surface gets disturbed and becomes very wavy in time. After the kids leave the pool, the waves on the surface continue to oscillate back and forth at a somewhat regular frequency, just like the pendulum bob moving back and forth about its rest position. While the pendulum frequency is determined by the string length and the pendulum mass, the water wave frequency is primarily determined by the distance between two wave crests. Large distances between wave crests, or wavelengths, oscillate very slowly, whereas small ripples, like those of Faraday's experiment, oscillate quickly. Returning to the pool, eventually the

waves die out just like the pendulum bob returned to rest. One of the explanations for this which is more well known is the fluid viscosity, which acts as a source of energy dissipation in fluids.

Before explaining how the waves of Faraday's experiment manifest themselves, a real experiment demonstrating parametric resonance will be demonstrated. Walking home from the grocery store with shopping bags, one might notice that after picking up a certain pace the swaying of one's arms begins to naturally fall into rhythm with the steps they are taking. This is very much parametric resonance! Letting one's arm hang loose, the shopping bag acts as a pendulum bob, and when walking is commenced, the up and down motion of one's shoulder acts in the exact same way as Faraday's vibration of his plate. As an experiment, you ought try using shopping bags of different lengths and the amount of "apples" in the bag to sense the different resonances which can be achieved between the motion of the bag and your stride. Notably one will see that normally the bag executes one period for ever two steps. This is actually what Faraday also observedthe frequency of the ripples on the liquid surface was exactly half that of the violin bow frequency. Try sitting on a swing and seeing if you observe any similarities!

Just like the experiment here, parametric resonance is observed in a pendulum when the point to which it is connected is moved up and down. Similar to the initial incline or decline in an elevator, moving of the pendulum connection causes the magnitude of gravity to increase and decrease with the up and down motion. In the case the bob is moved slightly away from rest, if its motion back towards the rest position coincides with the downward motion of the pendulum connection, energy can be transferred to the bob, because its motion is in phase with the connection motion. Likewise, coincidence of the motion of the bob past the rest position with the upward motion of the connection also transfers energy to the bob. This is the method by which parametric resonance is achieved in the pendulum, and is identical to that of Faraday's

experiment in the sense that the effective gravity is being changed by the up and down motion of the system, and that the back and forth motion of the pendulum bob is substituted by the up and down motion of the standing waves.

This explanation forms the foundation for the understanding of the phenomenon explored in this dissertation. However, as mentioned before, Faraday had to strike his bow with a note loud enough to excite the waves. Equally, in the shopping bag experiment, one must walk at a pace brisk enough for any noticeable behavior to occur. This condition represents a threshold energy input which must be surpassed in order for the phenomenon to be observed, and is directly related to the dissipation present in an experiment. Measurement of these thresholds and comparison to a mathematical prediction is a central focus of this work.

Previous Faraday wave experiments have been performed in two different regimes, which lend themselves to two different means of predicting this threshold. At high frequencies, like the original experiments of Faraday, the excited wavelength is very small, and the sources of energy dissipation due to the sidewalls are less important than the dissipation due to viscosity. In this case the critical threshold can be predicted directly by analysis of the well known equations describing fluid motion, the Navier-Stokes equations. Replication of the sidewall behavior required by this analysis is difficult in experiment, and therefore in the low-frequency regime, where the sidewall dissipation is by contrast more significant, experiments have been designed to use low viscosity fluids and circumvent the necessity for such analysis. The thresholds are then matched, not predicted, by a model which includes the dissipation measured from the experiment.

While there are certain benefits to this type of approach in the low frequency regime, in this dissertation an experimental system which excites the parametric resonance at low frequencies has been designed which minimizes the dissipation due to sidewall effects, producing a good agreement with the predictions of the Navier-Stokes

equations. In doing so a novel Faraday wave system has been studied and many interesting phenomena have been revealed that were not observed in the previous experiments. One of these behaviors is the use of a liquid film to allow ideal sidewall behavior, much like one might apply a lubricant to a pendulum connection in order to minimize the associated dissipation. The other novel aspect is an observance of an interaction between the forced and the parametric resonances. Forced resonance represents the motion one could induce in a pendulum if they were to oscillate the connection from side to side rather than up and down. In the Faraday experiment this occurs because of a ripple that appears in the system due to the liquid sidewall meniscus. In the course of presenting these results, the mathematical model used to predict the thresholds is described in detail, as well as the experimental method.

REFERENCES

[1] Abramowitz, M., & Stegun, I. (1964). *Handbook of Mathematical Functions*. New York: Dover, Tenth ed.

[2] Arbell, H., & Fineberg, J. (1998). Spatial and temporal dynamics of two interacting modes in parametrically driven surface waves. *Physical review letters*, *81*(20), 4384–4387.

[3] Arbell, H., & Fineberg, J. (2002). Pattern formation in two-frequency forced parametric waves. *Physical Review E*, *65*(3), 036224.

[4] Bacri, J. C., Perzynski, R., Shliomis, M. I., & Burde, G. I. (1995). negative-viscosity effect in a magnetic fluid. *Physical review letters*, *75*(11), 2128–2131.

[5] Bajaj, R. (2003). Two-frequency parametric excitation of the surface of viscous magnetic fluid. *Journal of magnetism and magnetic materials*, *261*(1), 29–47.

[6] Bajaj, R., & Malik, S. (2002). Parametric instability of the interface between two viscous magnetic fluids. *Journal of magnetism and magnetic materials*, *253*(1), 35–44.

[7] Bashtovoi, V. G., & Rosensweig, R. E. (1993). Excitation and study of subcritical waves on a magnetic fluid surface. *Journal of magnetism and magnetic materials*, *122*(1), 234–240.

[8] Bechhoefer, J., Ego, V., Manneville, S., & Johnson, B. (1995). An experimental study of the onset of parametrically pumped surface waves in viscous fluids. *J. Fluid Mech.*, *288*, 325–350.

[9] Becker, J., & Miles, J. (1986). Parametric excitation of an internally resonant double pendulum, ii. *Zeitschrift für Angewandte Mathematik und Physik (ZAMP)*, *37*(5), 641–650.

[10] Benjamin, T. B., & Scott, J. C. (1979). Gravity-capillary waves with edge constraints. *J. Fluid Mech*, *92*(2), 241–267.

[11] Benjamin, T. B., & Ursell, F. (1954). The stability of a plane free surface of a liquid in vertical periodic motion. *Proc. R. Soc. Lond. A*, *225*, 505–515.

[12] Besson, T., Edwards, W. S., & Tuckerman, L. S. (1996). Two-frequency parametric excitation of surface waves. *Phys. Rev. E*, *54*, 507–514.

[13] Blamey, J., Yeo, L. Y., & Friend, J. R. (2013). Microscale capillary wave turbulence excited by high frequency vibration. *Langmuir*.

[14] Blossey, R., *et al.* (2003). Self-cleaning surfaces-virtual realities. *Nature materials*, *2*(5), 301–306.

[15] Case, K. M., & Parkinson, W. C. (1957). Damping of surface waves in an incompressible fluid. *J. Fluid Mech.*, *2*, 172–184.

[16] Chandrasekhar, S. (1981). *Hydrodynamic and hydromagnetic stability*. Dover publications.

[17] Chen, P., & Viñals, J. (1999). Amplitude equation and pattern selection in faraday waves. *Physical Review E*, *60*(1), 559.

[18] Christiansen, B., Alstrøm, P., & Levinsen, M. T. (1992). Ordered capillary-wave states: quasicrystals, hexagons, and radial waves. *Physical review letters*, *68*(14), 2157–2160.

[19] Ciliberto, S., Douady, S., & Fauve, S. (1991). Investigating space-time chaos in faraday instability by means of the fluctuations of the driving acceleration. *EPL (Europhysics Letters)*, *15*, 23–28.

[20] Ciliberto, S., & Gollub, J. P. (1985). Chaotic mode competition in parametrically forced surface waves. *J. Fluid Mech.*, *158*(1), 381–398.

[21] Cowley, M. D., & Rosensweig, R. E. (1967). The interfacial stability of a ferromagnetic fluid. *J. Fluid Mech*, *30*(4), 671–688.

[22] Cross, M. C., & Hohenberg, P. C. (1993). Pattern formation outside of equilibrium. *Reviews of Modern Physics*, *65*(3), 851.

[23] Das, S. P., & Hopfinger, E. J. (2008). Parametrically forced gravity waves in a circular cylinder and finite-time singularity. *J. Fluid Mech.*, *599*, 205–228.

[24] Dodge, F. T., Kana, D. D., & Abramson, H. N. (1965). Liquid surface oscillations in longitudinally excited rigid cylindrical containers. *AIAA J.*, *3*, 685–695.

[25] Douady, S. (1990). Experimental study of the Faraday instability. *J. Fluid Mech.*, *221*, 383–409.

[26] Douady, S., & Fauve, S. (1988). Pattern selection in faraday instability. *Europhysics letters*, *6*(3), 221–226.

[27] Drazin, P. G., & Reid, W. H. (1981). *Hydrodynamic stability*. Cambridge Monographs on Mechanics and Applied Mathematics.

[28] Edwards, W. S., & Fauve, S. (1994). Patterns and quasi-patterns in the Faraday experiment. *J. Fluid Mech.*, *278*, 123–148.

[29] Ezerskii, A. B., Korotin, P. I., & Rabinovich, M. I. (1985). Random self-modulation of two-dimensional structures on a liquid surface during parametric excitation. *Soviet Journal of Experimental and Theoretical Physics Letters*, *41*, 157.

[30] Faraday, M. (1831). On the forms and states of fluids on vibrating elastic urfaces. *Phil. Trans. R. Soc. Lond.*, *52*, 319–340.

[31] Fauve, S., Kumar, K., Laroche, C., Beysens, D., & Garrabos, Y. (1992). Parametric instability of a liquid-vapor interface close to the critical point. *Phys. Rev. Lett.*, *68*(21), 3160–3163.

[32] Friend, J., & Yeo, L. Y. (2011). Microscale acoustofluidics: Microfluidics driven via acoustics and ultrasonics. *Rev. Mod. Phys.*, *83*, 647–704.

[33] Gollub, J. P., & Meyer, C. W. (1983). Symmetry-breaking instabilities on a fluid surface. *Physica D: Nonlinear Phenomena*, *6*(3), 337–346.

[34] Gu, X. M., Sethna, P. R., & Narain, A. (1988). On three-dimensional nonlinear subharmonic resonant surface waves in a fluid. i: Theory. *Journal of applied mechanics*, *55*(1), 213–219.

[35] HaQuang, N., Mook, D. T., & Plaut, R. H. (1987). A non-linear analysis of the interactions between parametric and external excitations. *Journal of Sound and Vibration*, *118*(3), 425–439.

[36] Henderson, D., & Miles, J. (1990). Single-mode Faraday waves in small cylinders. *J. Fluid Mech.*, *213*, 95–109.

[37] Henderson, D. M., & Miles, J. W. (1989). Faraday waves in 2:1 internal resonance. *J. Fluid Mech.*, *222*, 449–470.

[38] Hill, D. F. (2002). The faraday resonance of interfacial waves in weakly viscous fluids. *Physics of Fluids*, *14*, 158.

[39] Hill, G. W. (1886). On the part of the motion of the lunar perigee which is a function of the mean motions of the sun and moon. *Acta Mathematica*, *8*(1), 1–36.

[40] Hocking, L. M. (1987). The damping of capillary-gravity waves at a rigid boundary. *J. Fluid Mech*, *179*, 253–266.

[41] Huygens, C. (1673). *Horologium oscillatorium: sive, De motu pendulorum ad horologia aptato demostrationes geometricae*. F. Muguet.

[42] Ibrahim, R. A. (2005). *Liquid sloshing dynamics: theory and applications*. Cambridge Univ Press.

[43] Ito, T., & Kukita, Y. (2008). Interface behavior between two fluids vertically oscillated in a circular cylinder under nonlinear contact line condition. *J. Fluid Sci. Tech.*, *3*, 690–711.

[44] Ito, T., Tsuji, Y., & Kukita, Y. (1999). Interface waves excited by vertical vibration of stratified fluids in a circular cylinder. *J. Nuc. Sci. and Tech*, *36*, 508–521.

[45] James, A. J., Vukasinovic, B., Smith, M. K., & Glezer, A. (2003). Vibration-induced drop atomization and bursting. *J. Fluid Mech.*, *476*, 1–28.

[46] Johns, L., & Narayanan, R. (2002). *Interfacial Instability*. Springer.

[47] Keolian, R., Turkevich, L. A., Putterman, S. J., Rudnick, I., & Rudnick, J. A. (1981). Subharmonic sequences in the faraday experiment: departures from period doubling. *Physical Review Letters*, *47*(16), 1133–1136.

[48] Keulegan, G. H. (1958). Energy dissipation in standing waves in rectangular basins. *J. Fluid Mech.*, *6*, 33–50.

[49] Kudrolli, A., & Gollub, J. P. (1996). Patterns and spatiotemporal chaos in parametrically forced surface waves: a systematic survey at large aspect ratio. *Physica D: Nonlinear Phenomena*, *97*(1), 133–154.

[50] Kudrolli, A., Pier, B., & Gollub, J. P. (1998). Superlattice patterns in surface waves. *Physica D: nonlinear phenomena*, *123*(1), 99–111.

[51] Kumar, K. (1996). Linear theory of Faraday instability in viscous fluids. *Proc. R. Soc. Lond. A*, *452*, 1113–1126.

[52] Kumar, K., & Tuckerman, L. (1994). Parametric instability of the interface between two fluids. *J. Fluid Mech.*, *279*, 49–67.

[53] Landau, L., & Levich, B. (1942). Dragging of a liquid by a moving plate. *Acta Physicochim. URSS*, *17*(42).

[54] Landau, L. D. (1987). *Fluid Mechanics: Volume 6 (Course Of Theoretical Physics) Author: LD Landau, EM Lifshitz, Publisher: Bu*. Butterworth-Heinemann.

[55] McLachlan, N. (1947). *Theory and application of Mathieu functions*. Clarendon Press.

[56] Mei, C. C., & Liu, L. F. (1973). The damping of surface gravity waves in a bounded liquid. *J. Fluid Mech.*, *59*(02), 239–256.

[57] Melde, F. (1860). Über die erregung stehender wellen eines fadenförmigen körpers. *Annalen der Physik*, *187*(12), 513–537.

[58] Miles, J. W. (1967). Surface-wave damping in closed basins. *Proc. R. Soc. Lond. A*, *297*, 459–475.

[59] Miles, J. W. (1984). Nonlinear Faraday resonance. *J. Fluid Mech.*, *146*, 285–302.

[60] Milner, S. T. (1991). Square patterns and secondary instabilities in driven capillary waves. *J. Fluid Mech.*, *225*, 81–100.

[61] Müller, H. W. (1993). Periodic triangular patterns in the faraday experiment. *Physical review letters*, *71*(20), 3287–3290.

[62] Müller, H. W., Wittmer, H., Wagner, C., Albers, J., & Knorr, K. (1997). Analytic stability theory for Faraday waves and the observation of the harmonic surface response. *Phys. Rev. Lett.*, *78*(12), 2357–2360.

[63] Nayfeh, A. H., & Mook, D. T. (1979). Nonlinear oscillations. *Nonlinear oscillations, by Nayfeh, Ali Hasan; Mook, Dean T. New York: Wiley, c1979.*, *1*.

[64] Perry, M. P., & Jones, T. B. (1975). Interfacial parametric ferrohydrodynamics. *Journal of Applied Physics*, *46*(2), 756–760.

[65] Pétrélis, F., Falcon, E., & Fauve, S. (2000). Parametric stabilization of the rosensweig instability. *The European Physical Journal B-Condensed Matter and Complex Systems*, *15*(1), 3–6.

[66] Qi, A., Friend, J. R., Yeo, L. Y., Morton, D. A. V., McIntosh, M. P., & Spiccia, L. (2009). Miniature inhalation therapy platform using surface acoustic wave microfluidic atomization. *Lab Chip*, *9*(15), 2184–2193.

[67] Raman, C. V. (1912). Experimental investigations on the maintenance of vibrations. *Bulletin of the Indian Association for the Cultivation of Science*, *6*, 1–40.

[68] Rayleigh, J. W. S. (1945). The theory of sound, vols. 1 and 2.

[69] Rinaldi, C., Chaves, A., Elborai, S., He, X. T., & Zahn, M. (2005). Magnetic fluid rheology and flows. *Current opinion in colloid & interface science*, *10*(3), 141–157.

[70] Rosensweig, R. E. (1997). *Ferrohydrodynamics*. Dover Publications.

[71] Simonelli, F., & Gollub, J. P. (1989). Surface wave mode interactions: effects of symmetry and degeneracy. *J. Fluid Mech.*, *199*(1), 471–494.

[72] Skeldon, A. C., & Guidoboni, G. (2007). Pattern selection for Faraday waves in an incompressible fluid. *SIAM J. Appl. Math.*, *67*(4), 1064–1100.

[73] Slane, J., & Tragesser, S. (2011). Analysis of periodic nonautonomous inhomogeneous systems. *Nonlinear Dynamics and Systems Theory*, *11*(2).

[74] Slattery, J. (1999). *Advanced Transport Phenomena*. Cambridge Univ Press.

[75] Someya, S., & Munakata, T. (2005). Measurement of the interface tension of immiscible liquids interface. *J. Cryst. Growth*, *275*, e343–e348.

[76] Tipton, C. (2003). *Interfacial Faraday Waves in a Small Cylindrical Cell*. Ph.D. thesis, University of Manchester.

[77] Tipton, C. R., & Mullin, T. (2004). An experimental study of Faraday waves formed on the interface between two immiscible liquids. *Phys. Fluids*, *16*, 2336–2341.

[78] Tufillaro, N. B., Ramshankar, R., & Gollub, J. P. (1989). Order-disorder transition in capillary ripples. *Physical review letters*, *62*(4), 422–425.

[79] Virnig, J. C., Berman, A. S., & Sethna, P. R. (1988). On three-dimensional nonlinear subharmonic resonant surface waves in a fluid: Part II–experiment. *Trans. ASME E: J. Appl. Mech.*, *55*, 220–224.

[80] Wagner, C., Müller, H.-W., & Knorr, K. (2003). Pattern formation at the bicritical point of the Faraday instability. *Phys. Rev. E*, *68*, 066204.

[81] Xu, J., & Attinger, D. (2007). Control and ultrasonic actuation of a gas–liquid interface in a microfluidic chip. *Journal of Micromechanics and Microengineering*, *17*(3), 609.

[82] Zhang, W., & Viñals, J. (1997). Pattern formation in weakly damped parametric surface waves. *J. Fluid Mech.*, *336*(1), 301–330.

[83] Zoueshtiagh, F., Amiroudine, S., & Narayanan, R. (2009). Experimental and numerical study of miscible Faraday instability. *J. Fluid Mech.*, *628*, 43–55.

BIOGRAPHICAL SKETCH

William Richard Batson III, affectionately known as Trey, was born in 1985 to Susan and Billy Batson in Lexington, South Carolina. He was inspired by science and math at an early age. When he wasn't enjoying learning his multiplication tables he was envying his friends who had already figured out what a "square root" was. In elementary school he read books on DNA and electricity for fun, and once told his grandmother he would grow up to be a brain surgeon. Before middle school he played summer baseball, which he believes to have been "decent" at, yet still most vividly remembers the time he was hit in the head by a warm-up flyball, and then cried about still having to go to bat against the league's ace pitcher. In the end baseball was fun, but the most humbling was golf which he loved even more, yet could never seem to find the right mindset to put it all together. At Irmo High School he built on his mother's love of music by discovering his own, and embraced the intellect of his father as he surrounded himself with an incredibly bright crowd, many of whom have already become doctors, lawyers, and silicone valley entrepreneurs. He followed his father by attending Clemson University in upstate South Carolina, where he chose chemical engineering based on his appreciation of chemistry and knack for calculus. He conducted undergrad research with David Bruce at Clemson for two summers, cementing his decision to pursue grad school because he enjoyed the "slow process" of research. He finished with his B.S. in chemical engineering and a minor in math in 2008, then wound up in Ranga Narayanan's office because the man was wearing New Balance shoes. Subsequently he spent his time learning to love research at the University of Florida. Girlfriends fluttered about here and there but at this point he is content to wait for the special someone, and is grateful for the friends he has made and all of the time he has been afforded to pursue his dreams, which he will continue to do, as he hopes give back some of what he has received one day with a career in academia. He received his Ph.D. from the University of Florida in the spring of 2013.